SPring-8
Research Frontiers

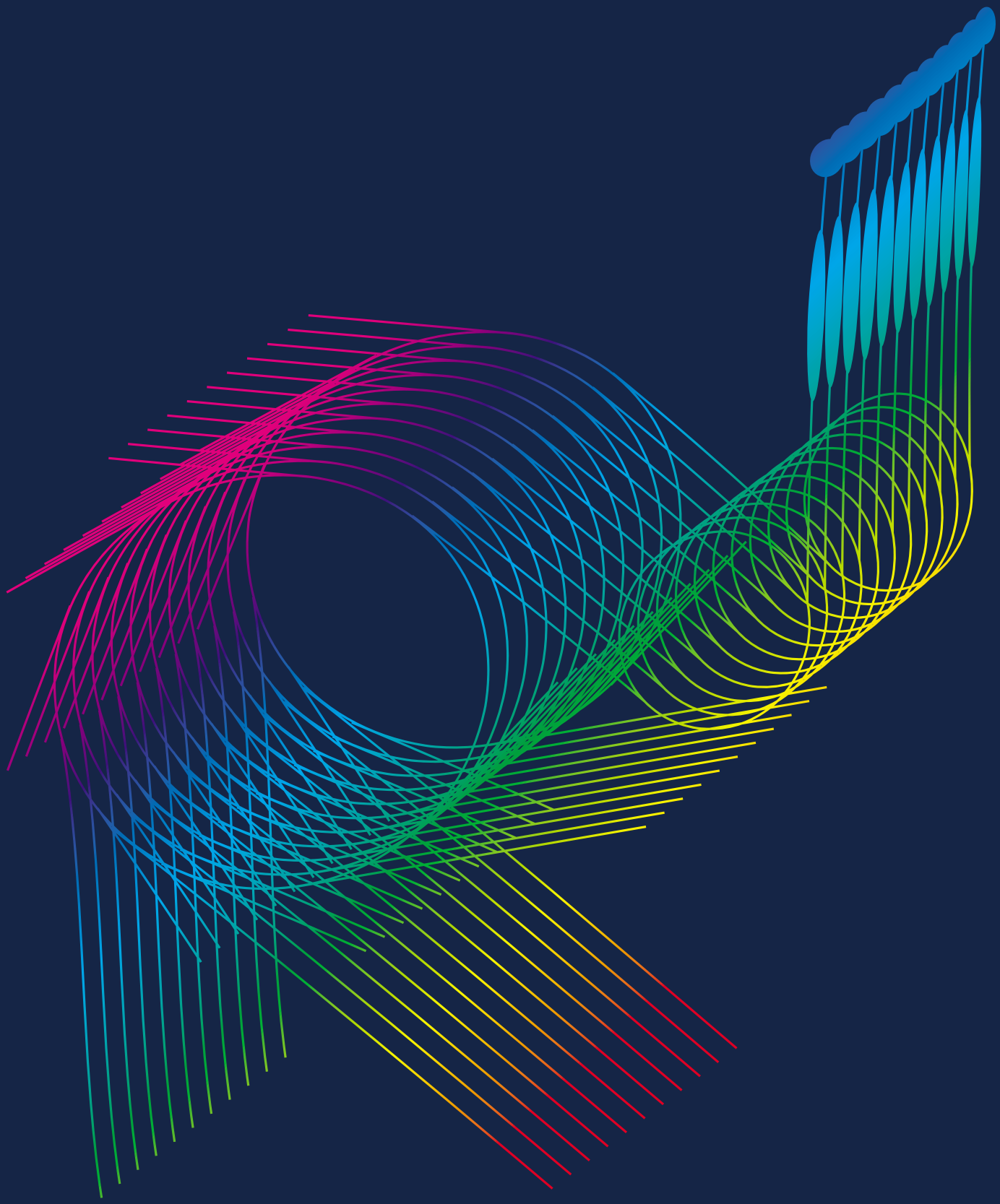

1997/1998

CONTENTS

PREFACE

SPring-8, one of the world's brightest synchrotron radiation sources covering from the soft to hard X-ray ranges (0.5 keV to 300 keV), succeeded in accumulating the electron beam in March 1997 and subsequently, started experimental tests on several beamlines from July of the same year. In October 1997, the facility was opened to outside users for experiments on ten beamlines.

Here, we present a report on the performance of the X-ray source and some of the experimental results obtained at SPring-8 from October 1997 to November 1998. This period corresponded to the first two terms of operation in the user service mode and involved more than 400 experiments conducted by 1800 users.

The X-ray source has already surpassed the expectations under the original design. Routine operation of the storage ring was achieved with a horizontal emittance of $7x10^{-9}$ m·rad and a coupling constant of 0.1%. These low values for the emittance and coupling constant resulted in vertical emittance and vertical beam size values as small as 10^{-11} m·rad and 10 mm, respectively. Direct measurement of the beam size is currently underway using several methods. The stored current has reached 100 mA with a lifetime longer than 60 hours. The source can be operated in the full-filling mode, 21-bunch mode, or single-bunch mode. The stability of the beam is extremely high and daily changes due to earth tides can be clearly observed in the storage ring circumference. This high performance of the source provides users with new opportunities for exploring new areas in various research fields.

This report covers the results of experiments classified into five groups, namely Life Science, Diffraction and Scattering, XAFS, Spectroscopy, and Instrumentation and Techniques. Many interesting results obtained at SPring-8, however, are not included in this volume simply because their data have not yet been fully analyzed, and in some cases the papers are yet to be published.

At this time, sixteen beamlines are in operation - ten public, one R&D, one contract and four JAERI/RIKEN beamlines. The results presented here were obtained from these beamlines.

We are now constructing nine public beamlines (including an infrared beamline), five contract, three JAERI/RIKEN, two R&D and two machine-study beamlines. Two RIKEN beamlines are to be special types. One is being built along a straight section where a 30-m undulator will be installed. The other will be a 1km-long beamline from an in-vacuum undulator.

Hiromichi Kamitsubo
Director
SPring-8 / JASRI

SPring-8 Research Frontiers describes the remarkable scientific achievements made at SPring-8 as well as developments in the accelerator and beamlines. This first volume covers a period of about one year since the opening of synchrotron radiation research facilities to public users. Hereafter, **SPring-8 Research Frontiers** will be published annually.

We tentatively classified synchrotron radiation research into five fields and invited five specialists from the Proposal Review Committee to be Editing Coordinators of their respective research fields as listed below:

Life Science : Professor Isao Tanaka (Hokkaido University)
Diffraction and Scattering : Professor Makoto Sakata (Nagoya University)
XAFS : Professor Yasuo Udagawa (Tohoku University)
Spectroscopy : Professor Atsushi Fujimori (The University of Tokyo)
Instrumentation and Techniques : Dr. Yoshio Suzuki (SPring-8/JASRI)

Since **SPring-8 Research Frontiers** is not a scientific journal, the authors are limited in number and will serve as contact persons.

We express our sincere thanks to these Editing Coordinators for their efforts in preparing the introductory overviews and making comments on each research field. We also express our thanks to the users and facility staff members of SPring-8 for their cooperation during the editing process. We acknowledge Dr. Katsutoshi Yasufuku for his comments and Ms. Marcia M. Obuti-Daté for her help in editing this volume.

Scientific Frontiers

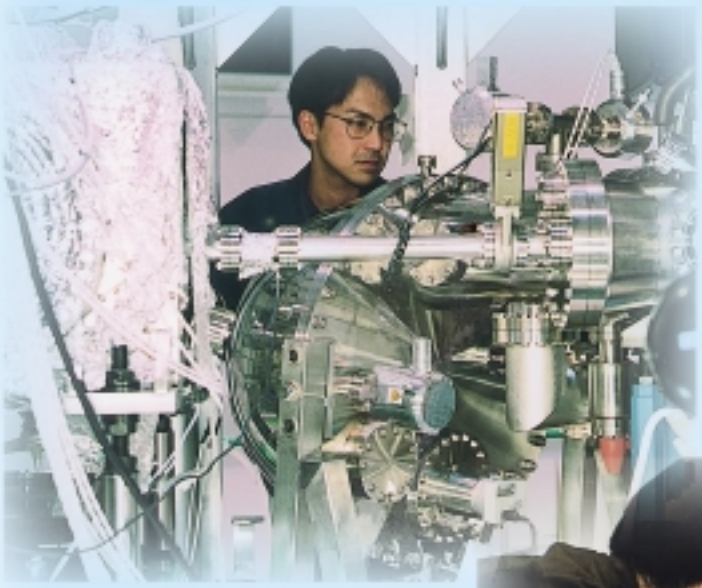

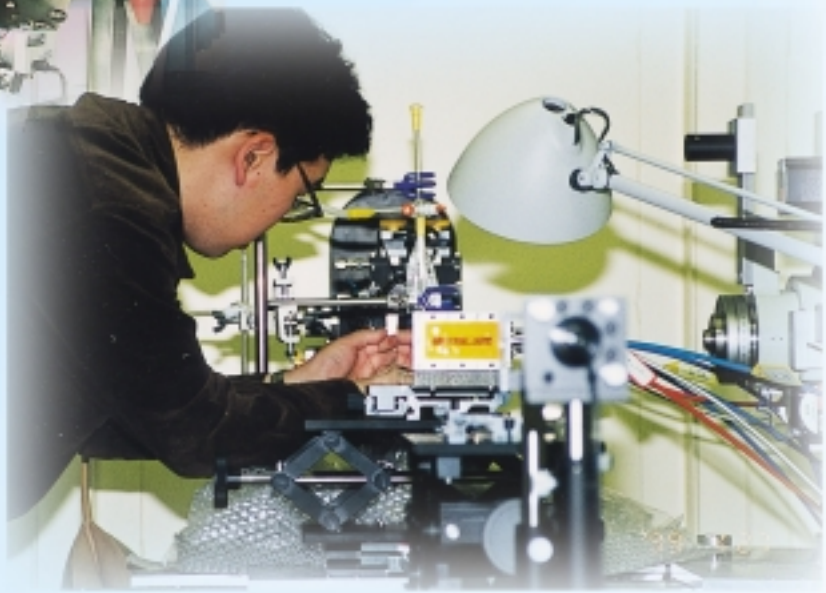

LIFE SCIENCE

During the last decade, synchrotron radiation has brought on enormous changes in the field of structural biology. Several thousand new structures of biological macromolecules have been determined through use of synchrotron radiation. It is therefore no longer expected that researchers in this field will attempt to study functions of macromolecules without referring to their three-dimensional structures.

The advent of the third generation synchrotron radiation source will clearly accelerate the development of research in this field. The third generation source will make it possible to analyze the structures of supramolecular complex crystals and microcrystals, that have very weak diffraction power. Furthermore, the use of anomalous scattering makes it possible to analyze these structures more rapidly.

The demand for beam time is larger than those available at SPring-8, especially in the life science field. This demand is not likely to decrease, particularly at a time when genome projects are expected to elucidate many unknown genes whose structures have yet to be analyzed. This new scientific field is referred to as structural genomics; in this field, the functions of unknown genes are studied by analyzing the three-dimensional structures of the products of particular genes. Such projects are expected to yield great benefits in a variety of fields, including biology, medicine, pharmacology and agriculture. The current report covers only a limited number of results from studies in this rapidly expanding field.

A beamline dedicated to the MAD method is in operation at SPring-8. This beamline was constructed on the basis of the trichromatic concept. In the trichromatic concept, three data sets using three different wavelengths are collected quasi-simultaneously. Several new structures have already been solved using this beamline. Among these, the structural analysis of blasticidin S deaminase, a Zn-binding protein, is provided in this report. The high intensity is also beneficial for atomic resolution structural analyses. The structure of the catalytic domain of chitinase, one of the multidomain proteins from Bacillus circulans, was refined at an atomic resolution (1.13 Å) using anisotropic displacement parameters.

Isao Tanaka

STUDIES ON THE MAD METHOD AT THE RIKEN BEAMLINE I BL45XU

The introduction of synchrotron radiation has accelerated the accumulation of three-dimensional structures, and with the tunability over a wide energy range of the synchrotron radiation, the multi-wavelength anomalous diffraction (MAD) method, which supplies phases from a single anomalous scatterer [1], has been developed [2]. By utilizing the third generation SR with the maximized advantage of the MAD method, **RIKEN beamline I (BL45XU)** is designed to contribute to research on structural biology.

One of the critical problems in macromolecular crystallography is the phase problem. The multiple isomorphous replacement (MIR) method has been the most useful phasing method in macromolecular crystallography. However, the MIR method requires at least two different heavy atom derivatives, of which crystals have to be in a high degree of isomorphism with the native crystals. On the other hand, employing the MAD method, all the data can be collected from the same crystal, if it contains anomalous scatterers. The MAD method has the advantage in terms of both accuracy and convenience in phase evaluation.

However, the development of the MAD method as a routine method in macromolecular crystallography is not straightforward because the contribution by the anomalous scatterer is minimal. To ensure accuracy in MAD experiments, it is essential to minimize systematic errors, such as absorption, detector characteristics and radiation damage, so that actual signals in Bijvoet and dispersive differences are measured as precisely as possible. In MAD experiments, at least three sets of diffraction data have to be collected with different wavelengths. In addition, the wavelengths have to be tuned as quickly as possible with a good reproducibility.

To achieve such an experimental environment for the MAD method, the "trichromatic concept" was introduced by the development of high-quality diamond crystals [3]. The trichromatic concept maintains that three kinds of data sets at three wavelengths are taken quasi-simultaneously for the same protein crystal without changing the setting by the "trichromator". The trichromator consists of three pairs of transparent diamond double-crystal monochromators with a fixed exit; it collinearly introduces X-rays with three monochromatized wavelengths in an identical beam direction (Figure 1).

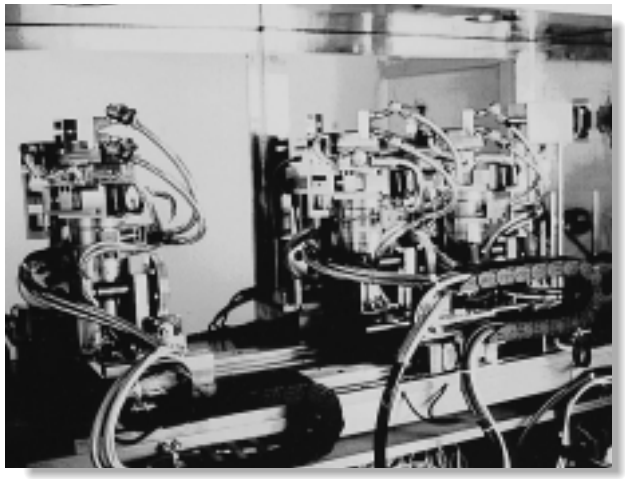

Fig.1: A sideview photograph of the trichromator. The trichromator contains 3-pairs of diamond double-crystal monochromators. Courtesy of IUCr [4].

Dichromatic synchrotron radiation is emitted from tandem vertical undulators. Monochromatized radiations of three wavelengths are cut out from the dichromatic synchrotron radiation with the trichromator, and the three are sequentially supplied through beam choppers. The data collection is sequentially performed at each wavelength to minimize systematic errors as well as background interference produced by other wavelengths (Figure 2).

The construction of the **RIKEN beamline I (BL45XU)** was started in August 1996, and progressed until June 1997. The commissioning of the beamline with synchrotron radiation began in July 1997. In the initial test, the trichromator successfully monochromatized three wavelengths at the same time, and three undulator beams were observed [4]. In the experimental station, a four-circle diffractomator and two different types of two-dimensional detectors were arranged. As a fast read-out two-dimensional detector, a multiple CCD X-ray detector (MCCDX) is being developed in order to record the diffraction patterns of protein crystals [5]. The MCCDX detector will have a 4 x 4 matrix

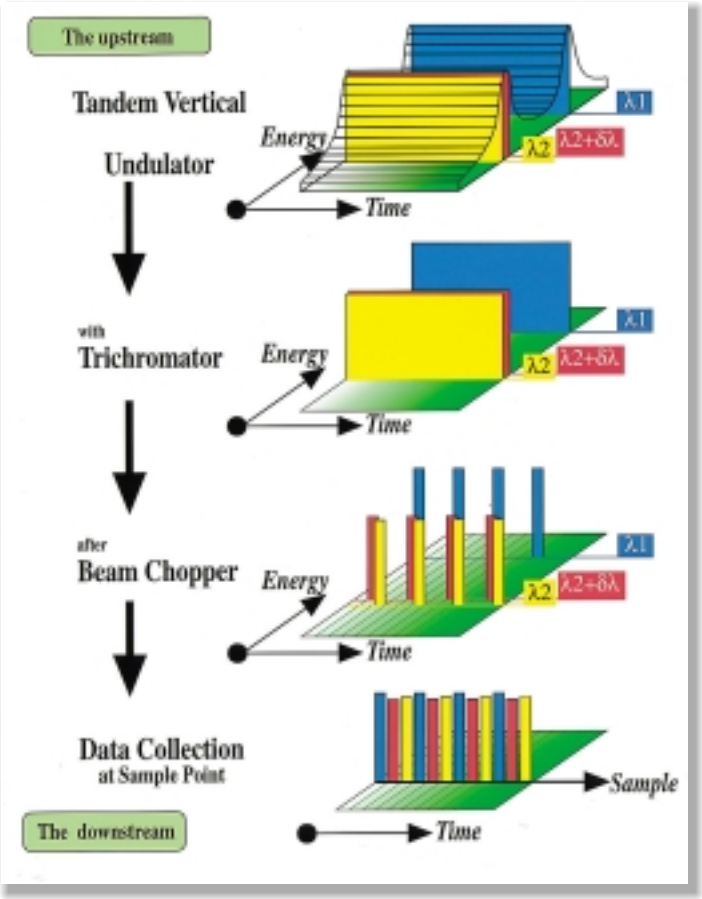

Fig. 2: Outiline of the "trichromatic concept". Courtesy of IUCr [4].

array of CCD X-ray detector modules with an active area size of 200 x 200 mm^2. In the initial stage, an imaging plate detector (RIGAKU R-AXIS IV) was installed and used for MAD data collection.

For MAD data collection, the first pair of the trichromator is set at a remote point of the absorption edge to obtain an anomalous scattering-free data set. As a result of XANES profile measurements, the other two wavelengths are supplied at the peak and edge energy of the anomalous scatterer, to maximize anomalous scattering contributions. The beam chopper sequentially supplies one wavelength out of the three to the experimental station.

The crystal of blasticidin S deaminase (BSD) was analyzed as the first sample. BSD is an enzyme which includes one Zn atom per one molecule (*Mr* ~ 13,000), and a homo-tetramer of BSD is included in an asymmetric unit. Figure 3 shows the XANES spectrum of BSD. The remote, peak and edge wavelengths of the Zn atom were selected at 1.0 Å, 1.2818 Å and 1.2822 Å, respectively. Three wavelength data sets of diffraction images were collected at 2.2 Å resolution. Four Zn positions of the asymmetric unit were clearly shown in anomalous and dispersive difference Patterson maps, and the initial electron density map was easily calculated. Figure 4 shows the MAD phased initial electron density map obtained, which clearly shows the secondary structure and side chains. The model building and the refinement of BSD progressed satisfactorily [6].

On the other hand, a dichromatic diffraction experiment using two wavelengths simultaneously was planned as a more efficient use of the trichromator. Two different wavelength diffractions at the remote and the edge of an anomalous scatterer were recorded on one imaging plate, and the diffraction at the third wavelength was recorded on another

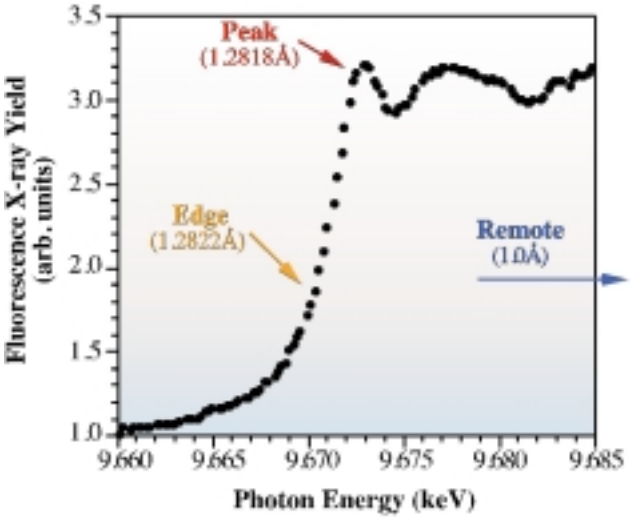

Fig. 3: The XANES spectrum of a BSD crystal, which includes a Zn atom. The MAD data collection was carried out at the wavelengths of 1.0 Å, 1.2818 Å and 1.2822 Å.

imaging plate. Figure 5 shows dichromatic diffraction images of another Zn protein. The dichromatic diffraction images were processed by using ordinary indexing software, the anomalous and dispersive difference Patterson maps clearly showed the Zn positions. The structural analysis progressed sufficiently. To date, we have already determined six structures, including one more Zn protein crystal, two Hg derivative crystals, and one Se-Met crystal.

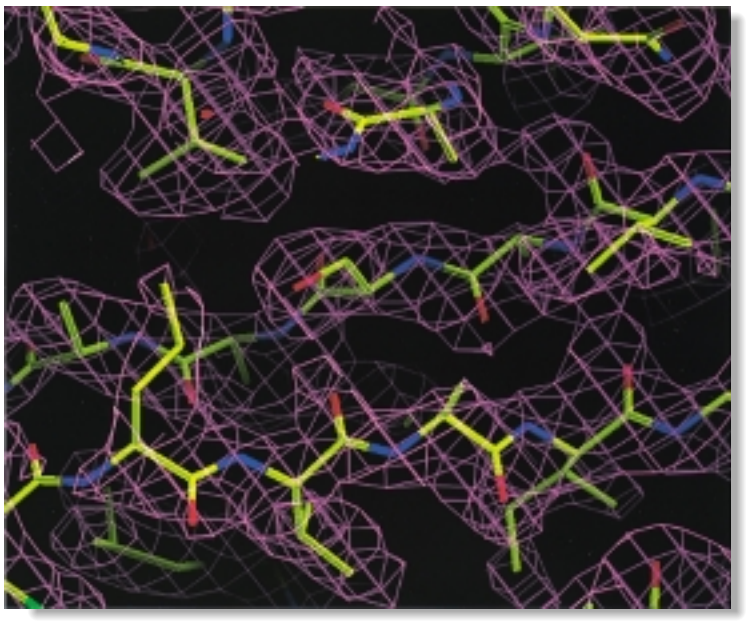

Fig. 4: MAD phased initial electron density map of BSD at 2.3 Å resolution.

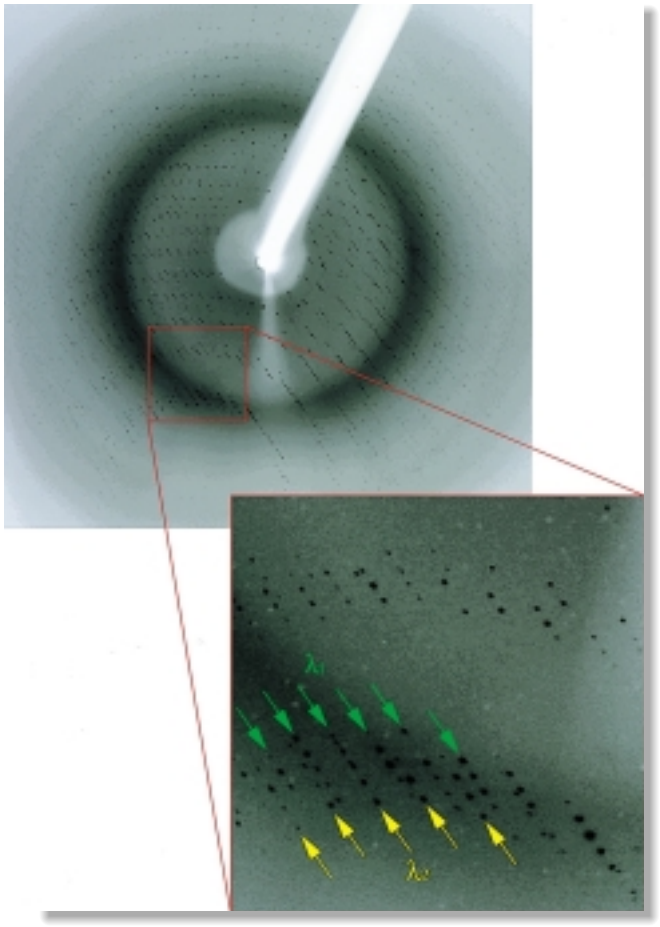

Fig. 5: Dichromatic diffraction images of a Zn protein. Two different diffractions at the remote (λ_1) and the edge (λ_2) wavelengths were exposed on the same imaging plate.

Masaki Yamamoto[a], Takashi Kumasaka[a] and Eiki Yamashita[a,b]
(a) SPring-8 / RIKEN
(b) Osaka University

E-mail : yamamoto@postman.riken.go.jp

Reference

[1] J. Karle, *Int. J. Quant. Chem.* **7** (1980) 357.
[2] W.A. Hendrickson *et al., Proteins* **4** (1988) 77.
[3] M. Yamamoto *et al., Rev. Sci. Instrum.* **66** (1995) 1833.
[4] M. Yamamoto *et al., J. Synchrotron Rad.* **5** (1998) 222.
[5] T. Kumasaka *et al., SPring-8 Annual Report* (1996) 210.
[6] M. Yamamoto *et al.,* to be published.

CRYSTAL STRUCTURE ANALYSIS OF THE CATALYTIC DOMAIN OF CHITINASE A1 FROM BACILLUS CIRCULANS AT ATOMIC RESOLUTION

Chitinases are enzymes that hydrolyzes chitin, a homopolymer of N-acetylglucosamine. These enzymes exist in a wide range of organisms, including bacteria, fungi, higher plants, insects, crustaceans and some vertebrates, and play various roles both inside and outside the cell. *Bacillus circulans* WL-12 secretes at least six kinds of chitinases into the culture mediums [1].

Chitinase A1, the main chitinase of this bacterium, has the strongest chitin degradation ability and is produced most voluminously compared to the other five chitinases. Chitinase A1 is a typical multi-domain protein which consists of three different kinds of domains (a catalytic domain, two type III homology units of fibronectin and a C-terminal short segment). Classified by homology among the amino acid sequences of the catalytic domain, chitinase A1 belongs to family 18 of the glycosyl hydrolases.

The mutant, named CA6, which consists only of the catalytic domain of chitinase A1, is composed of 419 amino acid residues (*Mr* 45,489) and maintains 49% of the chitin degradation activity of intact chitinase A1. CA6 was crystallized at 20° C by the vapor diffusion method in 10(w/v)% aqueous solution of polyethylene glycol (average molecular weight is *ca*. 4,000) as a precipitant and 25 mM potassium dihydrogenphosphate as an additive. Crystals of about 0.20 X 0.20 X 1.75 mm^3 were obtained in two weeks' time. The space group was P1, and the lattice constants were *a*= 43.96 Å, *b*= 48.62 Å, *c*= 54.59 Å, α= 108.90°, β= 95.06° and γ = 115.77°. One unit cell contained one molecule of CA6.

Initially, a structural analysis was attempted by the molecular replacement method using the X-ray diffraction data (completeness: 87.8%) up to 2.5 Å resolution collected in house by a Rigaku R-AXIS IIc oscillation diffractometer. A molecular model of CA6 based on the three-dimensional structure of chitinase A from *Serratia marcescens* with 33% amino acid sequence homology to CA6 was constructed by the homology modeling technique using the SWISS-MODEL. It was possible to determine the orientation of the CA6 molecule from a series of rotation searches with the program AMORE. However, there were many areas where an interpretation of the electron density map for the main chain was difficult, and accordingly the refinement of the crystal structure failed. Afterwards, it became possible to interpret the density map since the phases were expanded and improved with the program ARP using the X-ray diffraction data (completeness: 74.7%) up to 1.5 Å resolution collected at the beamline 18B of the Photon Factory. We are currently refining the three-dimensional structure, adding anisotropic displacement parameters to the calculation (Figure 1), with the

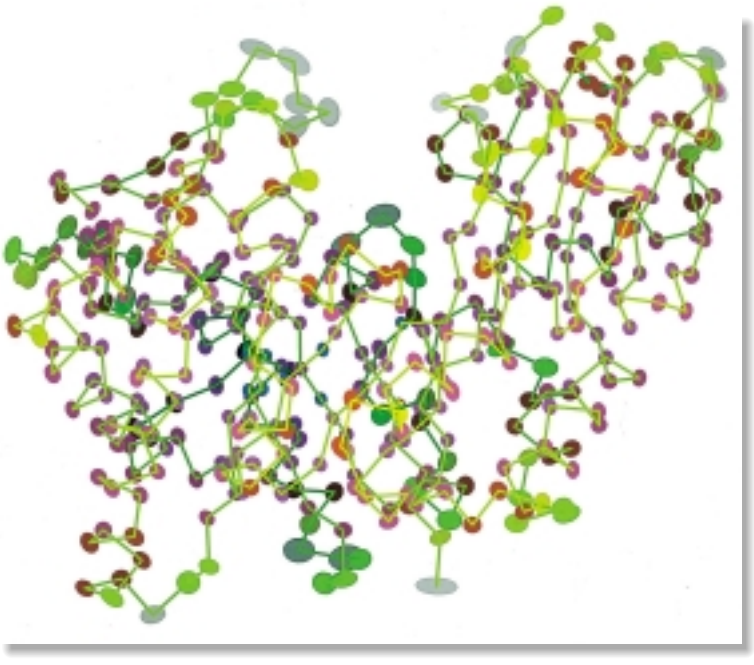

Fig. 1: Anisotropic displacement ellipsoids drawn at a 50% probability level for the 409 α-carbon atoms composing the catalytic domain of chitinase A1 (from Bacillus circulans).

program SHELX-97 using the diffraction data of up to 1.13 Å resolution [2]. The data were collected at room temperature by a Rigaku R-AXIS IV oscillation diffractometer installed at the beamline **BL44B2** (Figure 2). The current model contains 3,153 non-hydrogen protein atoms and 523 water molecules, and the current $R_{\text{-factor}}$ and the free $R_{\text{-factor}}$ are 0.196 and 0.212, respectively, against the 114,787 independent reflections (completeness: 0.826; $R_{\text{-merge}}$: 0.032).

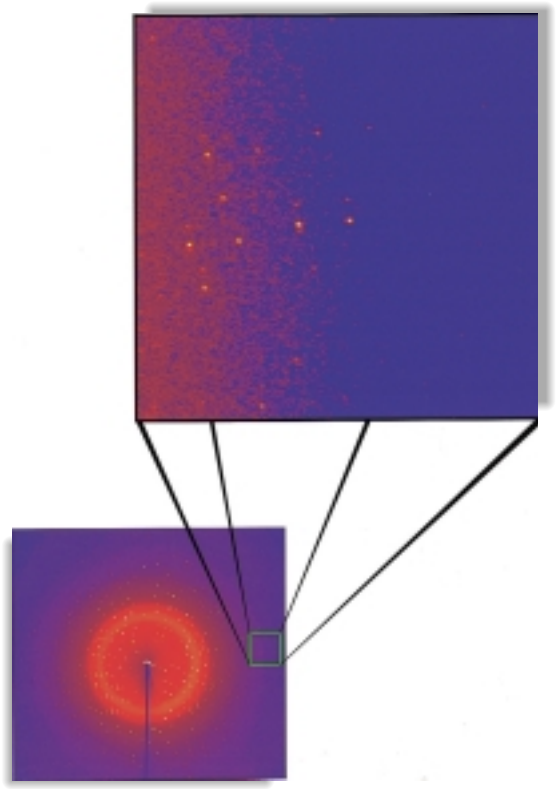

Fig. 2: X-ray diffraction image from a crystal of the catalytic domain of chitinase A1 (from Bacillus circulans) at the atomic resolution (1.13Å), measured by a Rigaku R-AXIS IV oscillation diffractometer.

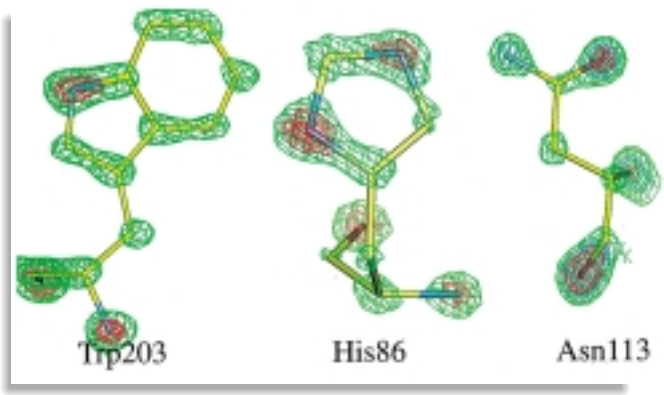

Fig. 3: Electron density maps for some of the amino acid residues of the catalytic domain of chitinase A1 (from Bacillus circulans).

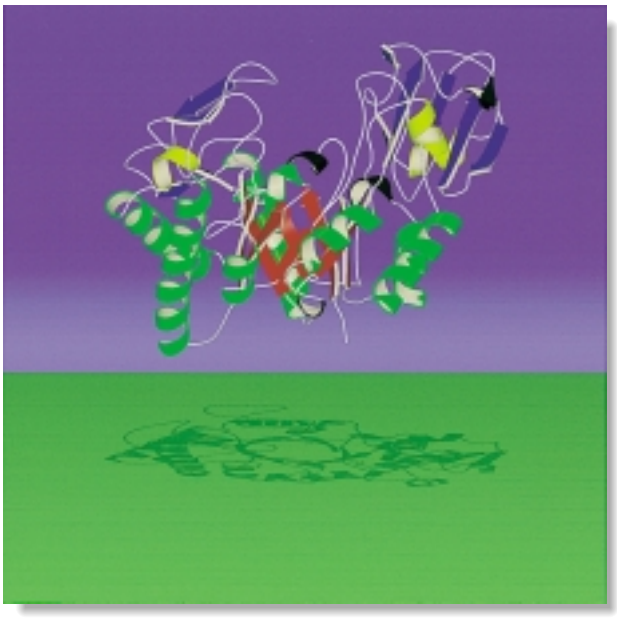

Fig. 4: Overall structure of the catalytic domain of chitinase A1 (from Bacillus circulans).

As a result of refinement at the atomic resolution, it became possible to identify the orientation of the imidazole ring of the histidine residues and to distinguish the nitrogen atom from the oxygen atom composing the side chain of the asparagine and glutamine residues (Figure 3). The three-dimensional structure of CA6 is composed of an α / β domain with a TIM barrel structure and two beta domains (Figure 4). The TIM barrel structure is common to all of the enzymes belonging to the family 18, whose three-dimensional structures are known.

Takuo Matsumoto and Takamasa Nonaka
Nagaoka University of Technology

E-mail : nonaka@vos.nagaokaut.ac.jp

References

[1] T. Watanabe *et al., J. Biol. Chem.* **265** (1990) 15659.
[2] T. Matsumoto *et al.,* to be published.

DIFFRACTION & SCATTERING

In the first year of utilization, most of the beam time had been consumed by test or preliminary experiments. Nevertheless, there have been many varieties of user activities in the field of X-ray diffraction and scattering, which covers structural analysis, high-resolution powder diffraction, phase transition, diffuse scattering, magnetic scattering, surface scattering, high-pressure experiments, nuclear spectroscopy and non-linear optics.

In particular, the activities in high-pressure experiment and nuclear spectroscopy have preceded among them. In high-pressure experiments, two projects deal with earth science and two others involve structural change through phase transition under high-pressure. In nuclear spectroscopy experiments, nuclear resonant scattering was applied to the analysis of atomic motions and fluctuations of magnetic moment in materials. In addition, the basic technique of coversion electron Mössbauer spectroscopy was developed.

Another topic that attracted attention was an electron-level structural analysis of fullerene compounds related to superconductivity. A fundamental study of X-ray parametric down conversion was also a significant work. These studies are expected to be developed further.

The scientific and engineering activities pursued at SPring-8 have clearly demonstrated that the facility is opening the door to a completely new world of diffraction and scattering.

Makoto Sakata

STRUCTURAL TRANSITION FROM SIMPLE CUBIC TO SIMPLE HEXAGONAL IN PHOSPHORUS AT 137 GPa

The phosphorus (P) of the group-Vb elements exhibits a unique sequence of structural phase transitions under pressure. At 4.5 GPa, black P which is the most stable form A17 structure (Cmca: P-I) at ambient conditions, undergoes a transition to the A7 phase ($R\bar{3}m$: P-II). At 10 GPa, it transforms further to the simple cubic (*sc*) phase ($Pm\bar{3}m$: P-III), which is metallic. The *sc* structure, a Bravais lattice with only one atom in the unit cell, is rare in all elements. The high-pressure stability of the *sc* phase has attracted special interest because it has the lowest packing fraction of atoms (0.524) and predicted Peierls' lattice instability. Because of the relatively low Z number of phosphorus, the X-ray diffraction studies had been limited to 83 GPa up to now. In this study, an angle dispersive X-ray diffraction technique has been applied to the study of the pressure-induced structural transition of phosphorus at the beamline **BL10XU**. The obtained powder diffraction patterns revealed that the *sc* phase transforms to the simple hexagonal (*sh*) phase (P6/mmm: P-V) at 137 GPa via an intermediate phase (unknown: P-IV). The instability of the *sc* phase was confirmed at 107 GPa. The typical powder patterns are shown in Figure 1. The *sh* structure is also as rare as the *sc* structure in the monoatomic system. The *sh* lattice can be easily derived from the *sc* lattice by a monoclinic distortion along the [110] direction (Figure 2). The volume reduction of the transition is estimated to be 7.6 % of the atomic volume of the *sc* phase ($-\Delta V = 0.74$ ^{3}) at 103 GPa. The estimation is done from the atomic volume versus pressure relation shown in Figure 3. The relatively large reduction comes from an increase in the coordination number from 6 to 8. Therefore, the structure of the P-IV phase may be found in the process of this distortion. The simplest and fundamental transition from the *sc* to *sh* structure is the first observation in the monoatomic system.

Iwasaki & Kikegawa [1] have proposed a transition to the (disordered-)bcc structure for the post-*sc* phase based on an analogy to the other group Vb elements (As, Sb and Bi), and another theoretical study has predicted the *sc*-*bcc* phase transition at 135 GPa [2]. However, phosphorus exhibited a different sequence of the structures from the one they proposed. Intense interest has thus been shown in the mechanism of the *sc*-*sh* transition. The fact that the *sh* structure has a lower packing fraction of the atoms (0.605) than any of the *bcc* (0.680), *fcc* and/or *hcp* (0.740) structures strongly suggests a survival of covalent bond in the cohesion of the metallic phase of phosphorus.

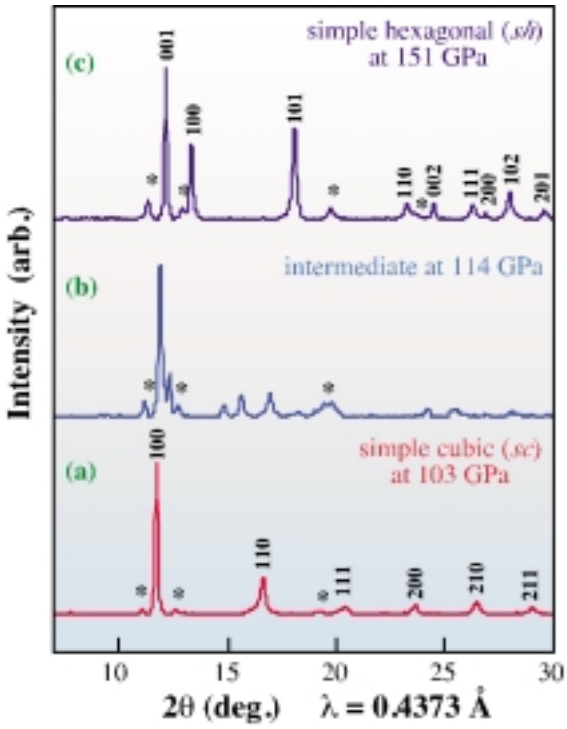

*Fig. 1: Typical powder diffraction patterns of the high-pressure phases of phosphorus at RT; **(a)** simple cubic (sc) phase at 103 GPa, **(b)** intermediate phase (P-IV) at 114 GPa, and **(c)** simple hexagonal (sh) phase at 151 GPa. They were obtained with an X-ray beam of λ=0.4373 Å. Miller indexes in **(a)** and **(c)** are appropriately assigned to the reflections from the sc (a=2.1374±0.0008 Å) and sh (a=2.1750±0.0004 Å, c=2.0628±0.0005 Å) phases, respectively. Since the P-IV phase exists in a narrow pressure region, it must be an intermediate phase between the sc and sh phases. The structure is unknown. Asterisk (*) represents reflection from an Re gasket. Courtesy of the Amer. Phys. Soc. [#].*

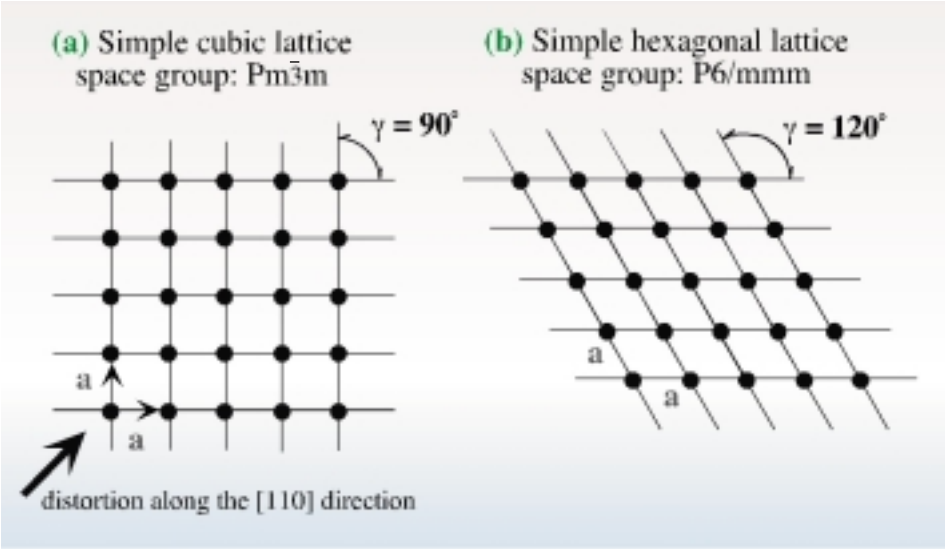

Fig. 2: Atomic arrangements of the sc lattice (a) and the sh lattice (b) projected onto the (001) plane. The sh lattice can be derived from the sc lattice by a monoclinic distortion along the [110] direction. The transition from the sc to sh structure is completed with a monoclinic angle γ of 120°. *Courtesy of the Amer. Phys. Soc. [#].*

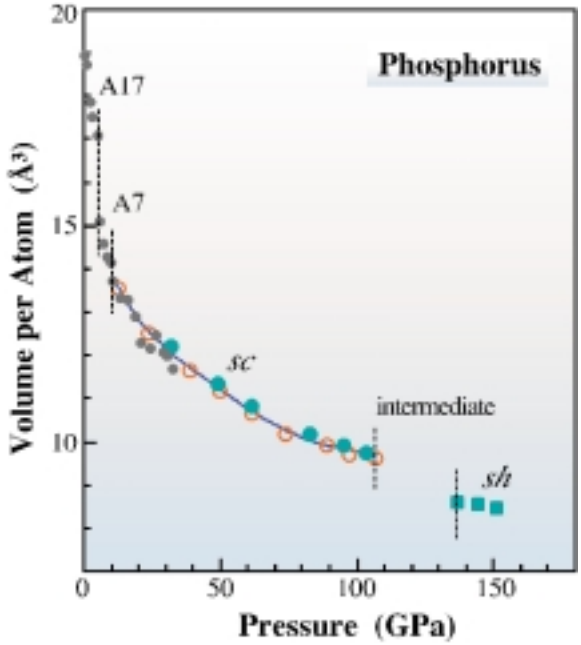

Fig. 3: Pressure dependence of atomic volume of phosphorus at 300 K. Present data are shown by open circles (for first run), and solid circles and squares (for second run). Small solid circles show previous data by Kikegawa & Iwasaki [3]. Solid line represents the result of a least-squares fitting of the Birch-Murnaghan equation of state to the present data of the sc phase: the bulk modulus (B_0)=70.7 GPa, its pressure derivative (B_0')=4.69 and relative atomic volume at atmospheric pressure (V/ V0)=0.815.
Courtesy of the Amer. Pys. Soc. [#].

Further extension of pressure in the multimegabar (>200 GPa) range must lead to a structure with a higher packing fraction of atoms, that is, a free-electron gas state such as the *fcc*-Al.

Yuichi Akahama
Himeji Institute of Technology

E-mail: akahama@sci.himeji-tech.ac.jp

References

[1] H. Iwasaki and T. Kikegawa, *Acta Cryst. B* **53** (1997) 353.
[2] T. Sasaki *et al., Jpn. J. Phys. Soc.* **57** (1988) 978.
[3] T. Kikegawa and H. Iwasaki, *Acta Cryst. B* **39** (1983) 158.

[#] Y. Akahama, M. Kobayashi and H. Kawamura, *Phys. Review B* **59** (1999) 8520.

IN-SITU MEASUREMENT ON RHEOLOGY OF SILICATE GARNET

We have examined the rheological properties of silicate garnet under *in-situ* mantle conditions with a multi-anvil high-pressure apparatus (SPEED-1500) equipped at the beamline **BL04B1**. One of the most important subjects of mantle rheology is to analyze the plastic behavior (*e.g.* flow law) of the mantle constituent minerals. In particular, the pressure effect on their plastic behavior is a major interest in the recent studies on mantle rheology. However, ordinary deformation apparatuses cannot directly elucidate the pressure effect due to the limitations of pressure ranges they generate.

Weidner *et al.* [1,2] have recently measured the yield strength and plastic behavior of diamond and $MgAl_2O_4$ spinel under *in-situ* mantle conditions by using a multi-anvil high-pressure apparatus with the aid of a synchrotron X-ray. This method is essentially a stress relaxation experiment. They focused on changes in the X-ray diffraction peak width from polycrystalline samples. The micro-scopic strain and stress, then the mechanical data of plasticity in samples can be evaluated from this observation. The most excellent point of this method is elucidation of the time-dependence on the micro-scopic strain while keeping high pressure and temperature. This method provides a measurement of plastic behavior of high-pressure minerals under the corresponding *in-situ* mantle conditions.

In this way we can estimate the pressure effect on plastic behavior of mantle constituent minerals. In the current study, we applied this method to the measurement of plastic behavior of silicate garnet, which is a major constituent mineral in the mantle transition zone and subducting slub, under high-pressure conditions.

We used ground Py50%Mj50% -garnet (50% pyrope and 50% majorite) which was synthesized with the multi-anvil high-pressure apparatus (ORANGE-2000) at Ehime University. The sample was compressed to 17 GPa at room temperature and heated stepwise to 450˚, 550˚, 650˚ and finally 750˚C in 300-, 240-, 180- and 60-minute intervals, respectively. The pressure increased from 17 to 19.5 GPa just after heating to 450˚C due to the thermal expansion of the sample; this pressure was kept constant throughout the heating treatment. Maintaining the pressure at 19.5 GPa and the temperature at the respective values, we analyzed the relaxation processes with time.

We estimated micro-scopic strains from the peak broadening and sharpening of (400), (420), (332) and (642) diffraction lines (Figure 1). During the pressurization at room temperature, the micro-scopic strain became nearly constant (ca. 0.025) over 10 GPa, which indicates that the sample

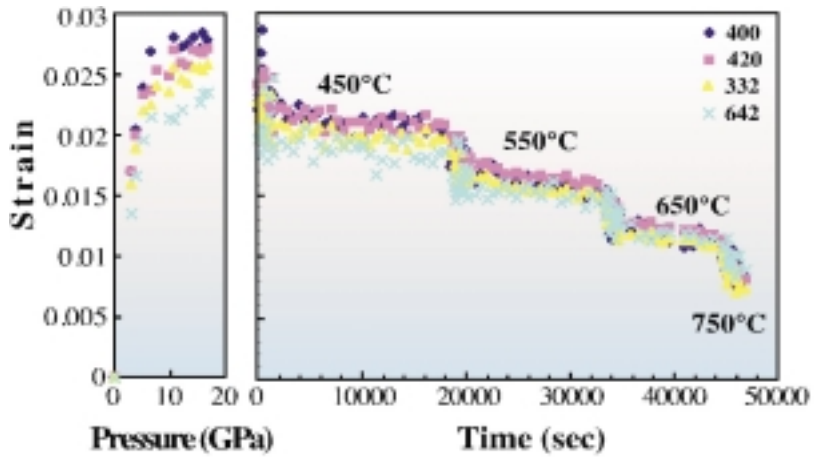

Fig.1: Microscopic strain in Py50%Mj50% -garnet as a function of load pressure, followed by heating at constant load.

reached its yield point. By multiplying the strain by an appropriate elastic modulus, the strain can be converted to elastic stress. Using 226 GPa as the elastic modulus (the value for Py59%Mj41% -garnet), the yield strength of Py50%Mj50% -garnet is calculated as *ca.* 6 GPa.

The micro-scopic strain decreased with time at each step of the heating, initially very fast and then much slower in the later stage. Even after heating to 750˚C, the micro-scopic strain did not become zero, which indicates the sample still had elastic strain.

We have previously conducted the relaxation experiments on Py50%Mj50%, Py100%, Py68%Al18%Gr14%Sp1% and Py23%Al48%Gr28%Sp1% -garnets at 7 GPa and 10 GPa by the same technique as used at Brookhaven National Laboratory. Here, Al, Gr and Sp denote almandine, grossular, and spessartine garnets, respectively. A comparison of all these data along with the current results suggests that the rheological behavior of silicate garnet strongly depends on its composition, namely that the plastic strength increases with an increasing component of either pyrope or majorite and with pressure.

Jun-ichi Ando[a] and Jiuhua Chen[b]
(a) Hiroshima University
(b) SUNY at Stony Brook

E-mail: ando@letitbe.geol.sci.hiroshima-u.ac.jp

References

[1] D.J. Weidner *et al.,* *Science* **266** (1994) 419.
[2] D.J. Weidner *et al.,* *Geophysical Monograph Series* **101** (1998) 473.

PRECISE DETERMINATION OF THE SPINEL-POSTSPINEL BOUNDARY IN Mg_2SiO_4 BY DIFFRACTION MEASUREMENT AT HIGH-PRESSURE AND HIGH-TEMPERATURE

Mg_2SiO_4 olivine is the most abundant mineral in the upper part of the Earth s mantle. By increasing pressure, this mineral is transformed in stages. The sequence is olivine, modified spinel, spinel structures, and finally two phases, *i.e.*, $MgSiO_3$ perovskite and MgO periclase (postspinel phase). The decomposition of Mg_2SiO_4 spinel to the postspinel phase is thought to be responsible mainly for the seismic discontinuity at the 660 km depth in the mantle. This speculation is supported by the experimental findings (*e.g.* [1]) that point out the coincidence between the transformation pressure and the pressures at the 660 km discontinuity. However, the pressure determinations in these studies have significantly large uncertainties because the pressures were indirectly estimated on the basis of calibrations using some fixed pressure reference points.

We have determined the P/T conditions of the spinel-postspinel phase boundary in a wide range of pressures and temperatures using a combination of white X-ray and a multianvil apparatus (SPEED-1500) [2] at the beamline **BL04B1** (Figure 1). A mixture of Mg2SiO4 olivine and gold powders was used as the starting material of the high pressure-temperature runs.

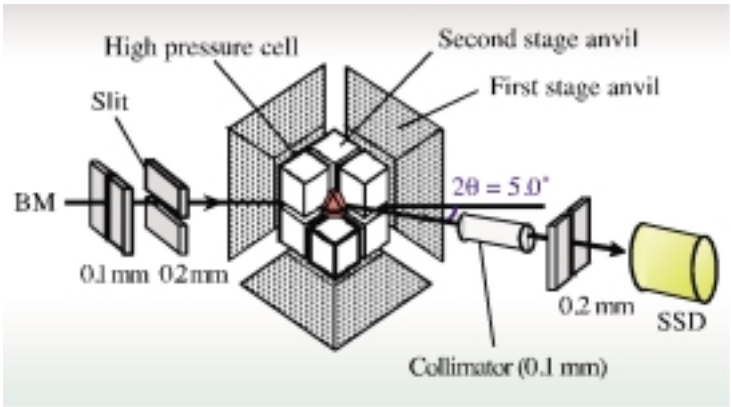

*Fig.1: Configuration of X-ray optics and multianvil apparatus (**SPEED-1500**).*

In the experiments, the pressure was increased first, and then X-ray diffraction data were acquired as increasing temperature. The phase at each P/T condition was identified from the X-ray diffraction patterns, the pressure was simultaneously determined by the molar volume of gold using an equation of state [3], and the temperature was measured by the thermocouple. Further details of the experimental conditions are given in Irifune et al. [4].

Figure 2 shows some examples of the X-ray diffraction patterns at various pressures and temperatures. In this run, we were able to observe the transformation from olivine (Fig. 2(**a**)) to the postspinel phase (Fig. 2(**c**)) through the metastable spinel phase (Fig. 2(**b**)). The postspinel phase transformed to the spinel phase when temperature was slightly changed near the phase boundary. A partial reverse transformation back to the postspinel phase was also confirmed by further experiments with different P/T conditions. In this manner, we precisely constrained the phase boundary between spinel and postspinel phases for the first time based on *in situ* X-ray diffraction measurements.

Figure 3 illustrates the spinel-postspinel phase boundary in Mg_2SiO_4 determined in this study. The transformation pressures were determined at temperatures up to 2000°C, whereas they were not well constrained at temperatures below 1000° C due to kinetic problems. The phase boundary has a negative Clapeyron slope of dP/dT = - 0.0025 GPa / °C , which is consistent with earlier results based on quench experiments [1]. However, it was found that the transformation pressures shift toward the low pressure side by more than 2 GPa compared with those of quench experiments.

The present results suggest that the spinel to postspinel transformation should occur at a depth of about 600 km in the Earth. This is inconsistent with the seismological observations, which show that the major seismic discontinuities in the Earth s mantle are only located at depths of 410 km and 660 km. It has been fairly well established that the 410 km discontinuity is caused by the olivine-modified spinel transformation on the basis of both quench and *in situ* X-ray diffraction experiments [5,6]. The present results, however, indicate the latter discontinuity is not due to the phase transformation in the mantle olivine.

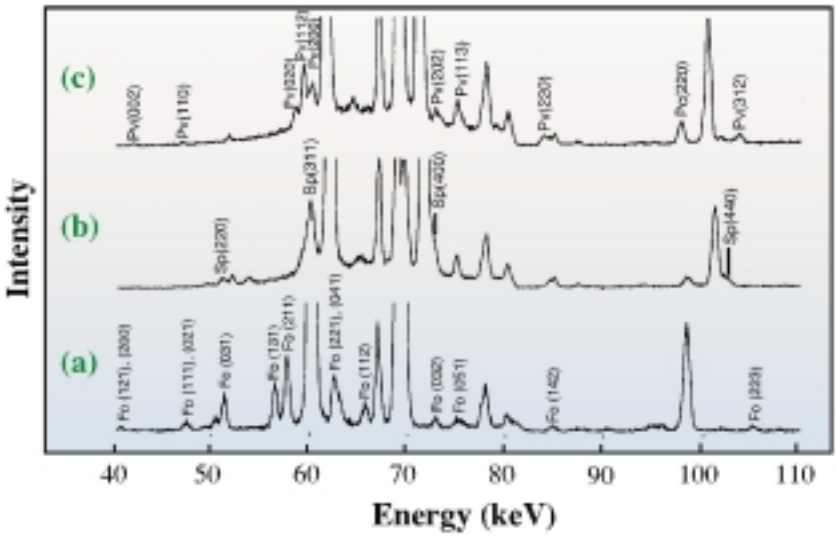

Fig.2: Examples of X-ray diffraction data obtained at ***(a)*** *the ambient pressure and temperature,* ***(b)*** *at 23.9 GPa, 1100°C, and* ***(c)*** *21.5 GPa, 1500°C in one of the in situ X-ray observations. Fo: Mg_2SiO_4 olivine; Sp: Mg_2SiO_4 spinel; Pv: $MgSiO_3$ perovskite; Pc: MgO periclase. Other lines are diffraction and characteristic peaks of gold, which was mixed with the olivine sample for pressure reference.*

The above inconsistency may be reconciled if some additional elements, such as Fe and Al, which are present in the actual Earth s mantle, significantly increase the transformation pressure.

Alternatively, the pressure scale based on the equation of state of gold may not be accurate enough to be applied to the P/T regimes of the present study. Although our results suggest that the conventionally accepted model for the cause of the 660 km discontinuity might be incorrect, these issues should be addressed before we reach a final conclusion.

Tetsuo Irifune and Norimasa Nishiyama
Ehime University

E-mail: irifune@dpc.ehime-u.ac.jp

References

[1] E. Ito and E. Takahashi, *J. Geophys. Res.* **94** (1989) 10637.
[2] W. Utsumi *et al., Rev. High Press. Sci. Technol.* **7** (1998) 1484.
[3] O.L. Anderson *et al., J. Appl. Phys.* **65** (1989) 1534.
[4] T. Irifune *et al., Science* **279** (1998) 1698.
[5] T. Katsura and E. Ito, *J. Geophys. Res.* **94** (1989) 15663.
[6] H. Morishima *et al., Science* **265** (1994) 1202.

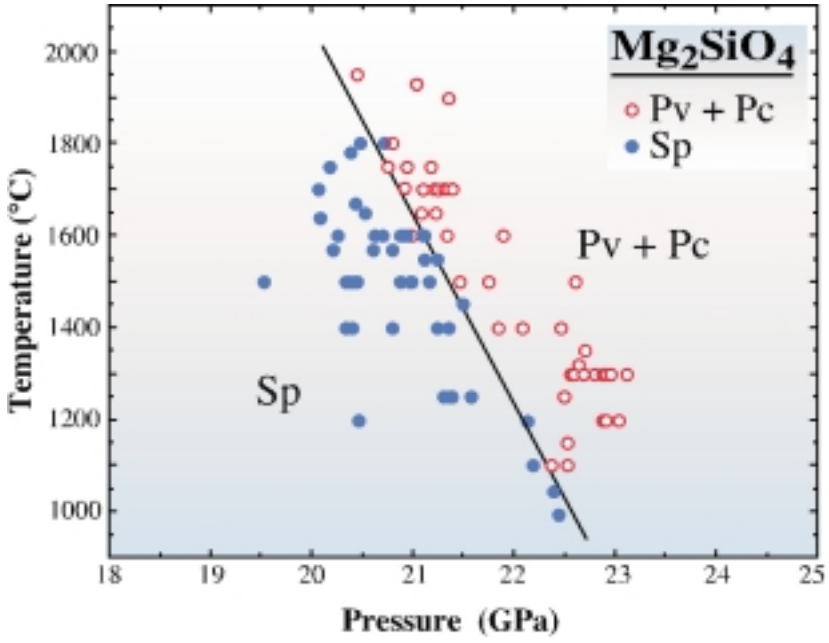

Fig.3: Phase boundary between the spinel and the postspinel phases. Closed circles denote P/T conditions where stability of the spinel phase was confirmed. Open circles show P/T conditions where the postspinel phase was stable.

X-RAY DIFFRACTION MEASUREMENTS FOR EXPANDED FLUID MERCURY

A substantial and continuous volume expansion from liquid to rarefied vapor occurs by the change of temperature and pressure around the liquid-vapor critical point without crossing the saturated vapor pressure curve. In the expansion process the mean interatomic distance increases by up to ten times compared with that under standard conditions. In metallic or semiconducting liquids, physical properties can drastically change. Liquid Hg, well known as a prototype of liquid metals, transforms into an insulating state when it is expanded up to the liquid-gas critical point (critical data of Hg [1] : T_c = 1478 ˚C, p_c = 1673 bar, ρ_c = 5.8 g/cm^3). The first indication of the metal-nonmetal (M-NM) transition, which occurs around 9 g/cm^3, was found in the electrical conductivity, thermoelectric power obtained by Hensel and Frank [2]. Many experimental and theoretical investigations focused on the M-NM transition have been made over the past few decades.

The information on the atomic arrangement of expanded fluid Hg is quite important for understanding the mechanism of the M-NM transition. However, the diffraction experiments for expanded fluid Hg are not easy because the critical pressure is very high. Tamura and Hosokawa [3] succeeded in measuring the X-ray diffraction pattern of expanded liquid Hg both in the metallic and critical regions using an in-house X-ray source.

We present new results of X-ray diffraction measurements using synchrotron radiation at SPring-8. These measurements extend from the liquid to the dense vapor region, which is beyond the liquid-vapor critical point.

Energy-dispersive X-ray diffraction measurements for expanded fluid Hg were performed using a diffractometer and high-pressure apparatus installed at the beamline **BL04B1**. White X-rays were used as the primary beam, and the scattered photons were detected by a solid state detector (SSD). The experimental conditions of high-temperatures up to 1520 ˚C and of high-pressures up to 1765 bar were achieved with an internally heated high-pressure vessel made of a super-high-tension steel. Fluid Hg was contained in a single crystal sapphire cell.

Figure 1 shows the density isochores of fluid Hg plotted in the pressure-temperature plane [1].

Figure 2 shows the pair distribution function g(r) for expanded fluid Hg under the different temperature and pressure conditions. To obtain the definite coordination number from the diffusive and broad atomic distribution in the non-crystalline state, we employed two different methods to integrate the first-neighboring atoms. In method **A**, $4\pi r^2\rho_0 g(r)$ is integrated up to the maximum position of g(r), r_1, and doubled. Here ρ_0 denotes the average number density of Hg. In method **B**, $4\pi r^2\rho_0 g(r)$ is integrated up to the first minimum position of g(r), r_{min}. We fixed r_{min} as 4.5 in the entire density range because r_{min} does not change so much except in the dense vapor region.

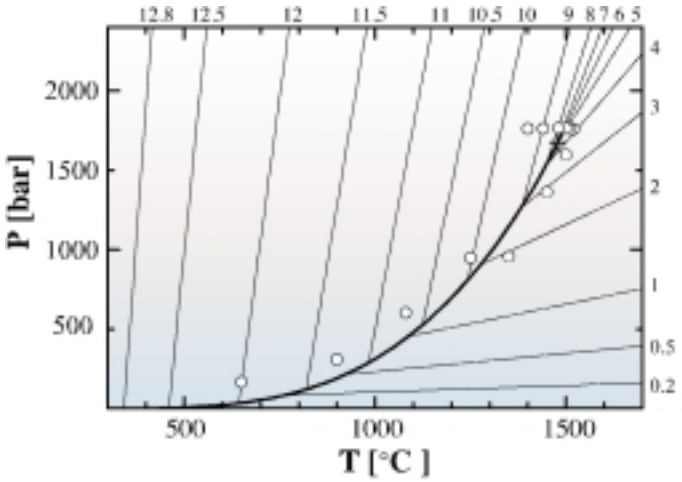

Fig. 1: Density isochores of fluid Hg plotted in the pressure-temperature plane [1]. Solid line indicates the saturated vapor-pressure curve and the cross shows the critical point. Open circles show the pressures and temperatures at which the X-ray diffraction measurements were performed [#].

The coordination numbers N_A and N_B obtained by methods **A** and **B** are plotted in Figure 3 as a function of density together with the nearest-neighbor distance r_1 at the bottom of the figure. N_B decreases substantially and linearly with decreasing density in the wide region from liquid to dense vapor. N_A also decreases almost linearly with decreasing density in the metallic region, but when the M-NM transition region is approached (*i.e.*, around 9-10 g/cm3), the deviation from the linear dependence appears. It seems that as the density deviation starts, the M-NM transition starts to occur.

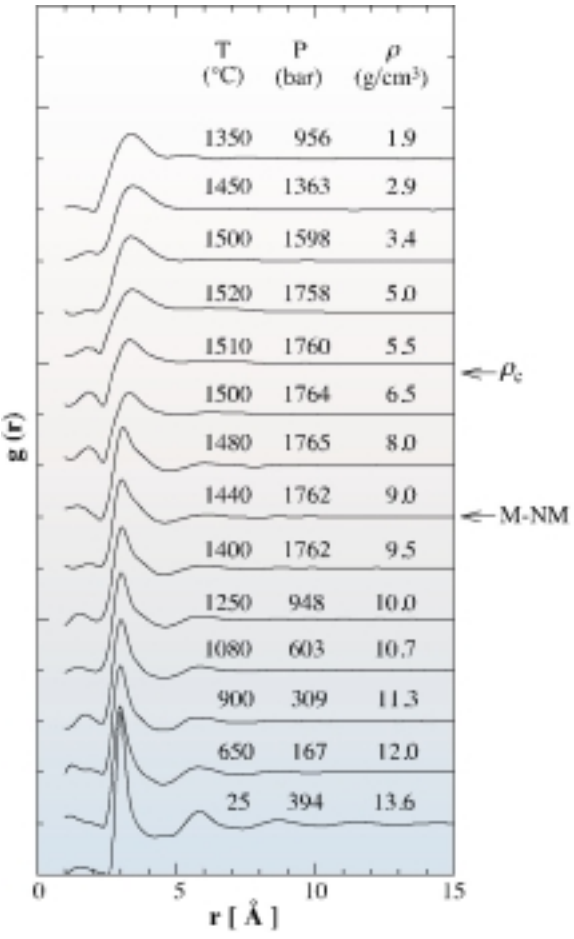

Fig. 2: Pair distribution function g(r) for expanded fluid Hg. Temperature, pressure and density are indicated on the upper right hand side of each data plot [*].

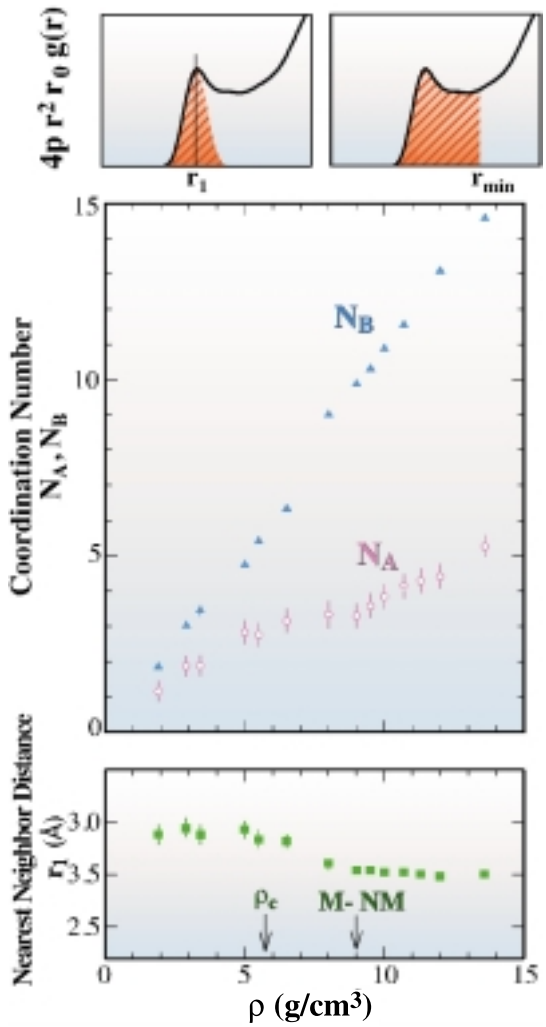

*Fig. 3: Coordination numbers N_A, N_B and nearest-neighbor distance r_1 of expanded fluid Hg as a function of density. Circles and triangles denote N_A and N_B obtained using methods **A** and **B**, respectively. Squares show variation of r_1 [*].*

In contrast to the N_A case, no anomalous behavior is observed in the behavior of N_B around this density region. In the dense vapor region the density variation of N_A changes again. As seen in the figure, r_1 in the metallic region remains almost unchanged with decreasing density, but when the M-NM transition region is approached r_1 starts to slightly increase. Such behavior coincides with that of N_A. In the dense vapor region r_1 substantially increases. The r_1 seems close to the interatomic distance of a Hg dimer in the rarefied vapor. From

these results, we can conclude that the density decrease of fluid Hg is essentially caused by the reduction of the coordination number through the entire density region as seen in the behavior of N_B. The variation in N_A gives more detailed information about the structural change accompanied by the M-NM transition. N_A represents the coordination number at the shortest distance in the first coordination shell, so the density variation of N_A suggests that the change in the nearest part of the first coordination shell is strongly related to the M-NM transition. As the most important observation, the gross feature of the density variation in N_A and r_1 in Figure 3 suggests that there exist three different regions in the density: the metallic region from 13.6 to about 10 g/cm^3, the M-NM transition region from 10 to the critical density of about 6 g/cm^3 and the dense vapor region.

Kozaburo Tamura and Masanori Inui
Hiroshima University

E-mail: tamura@mls.ias.hiroshima-u.ac.jp

References

[1] W. Gözlaff *et al., Z. Phys. Chem. NF* **156** (1988) 219; W. Gözlaff, *Ph.D Thesis,* University of Marburg (1988).
[2] F. Hensel and E. U. Frank, *Ber. Bunsenges. Phys. Chem.* **70** (1966) 1154.
[3] K. Tamura and S. Hosokawa, *Phys. Rev. B* **58** (1998) 9030.

[#] K. Tamura, M. Inui, I. Nakaso, Y. Oh'ishi, K. Funakoshi and W. Utsumi, *J. Phys. Condens. Matter* **10** (1998) 11405; [*] *Jpn. J. Appl. Phys., in press.*

CRYSTAL STRUCTURE ANALYSIS OF THE FULLERENE COMPOUNDS BY THE MAXIMUM ENTROPY METHOD

Alkali metal doped fullerenes in the form of A_2BC_{60} are fascinating substances. Many of them show superconductivity while a few others show no superconductivity. As the fundamental crystal structure, it is well known that C_{60} molecules form an fcc lattice and alkali metal atoms locate at both the tetrahedral and octahedral sites [1] . There is a close relation between the lattice constant of the compounds and their superconducting transition temperature, Tc [2,3]. For example, Rb_2CsC_{60} has a relatively high Tc. On the other hand, Li_2CsC_{60} shows no superconductivity.
It has been suggested that different bonding natures exist depending on their lattice constants and that they are closely related to the superconducting property [4]. Bonding nature may be divided into two regions, *i.e.*, the interatomic region between the doped metal atoms and the carbon-carbon region on C_{60} molecules. So far, there has been no definite experimental evidence on bonding nature. In this study, at the beamline **BL02B1**, the fine structure of Rb_2CsC_{60} and Li_2CsC_{60} are revealed [5], including the bonding nature for alkali metal doped fullerenes by the Maximum Entropy Method (MEM), which is an advanced imaging technique using diffraction data [6].
The MEM charge densities of Rb_2CsC_{60} and Li_2CsC_{60} are shown for a (110) plane in Figures 1**(a)** and **(b)**, respectively. At a glance, it can be easily seen that there are distinct structural differences between Rb_2CsC_{60} and Li_2CsC_{60}. A non-superconducting alkali metal doped fullerene, Li_2CsC_{60}, has uniform charge densities of the C_{60} molecule due to nearly free rotation of C_{60}. In contrast, a superconducting alkali metal doped fullerene, Rb_2CsC_{60}, has some kinds of disorder. To visualize three-dimensional distributions of the charge on the carbon cage in Rb_2CsC_{60}, the MEM electron density distribution of C_{60} and Rb atoms are shown by an equi-contour surface at 2.0 e Å^{-3} in Figures 2(**a**). In this figure, the characteristic features of the merohedral disorder, the hexagons facing toward Rb atoms and cloverleaf features,

be clearly seen. For reference, a schematic model of merohedral disorder is shown in Figure 2 (**b**). In order to show a strong structural contrast between Rb_2CsC_{60} and Li_2CsC_{60}, their three-dimensional equi-contour surfaces are shown in a Fig. 2 (**a**) and Figure 3, respectively.

In Figure 3, there are no localized densities in the interatomic region for these materials. Therefore, the chemical bond nature of doped alkali metals is ionic, which is independent of the existence of superconductivity. The electronic charges of doped alkali metals were estimated from the amount of electrons around a certain atomic site.

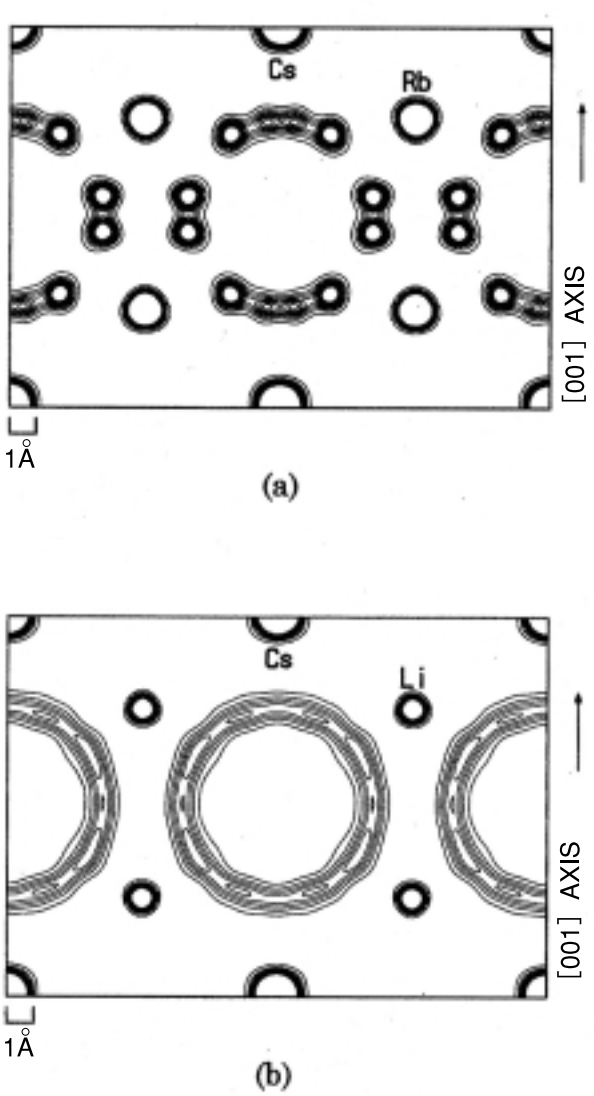

*Fig. 1: (110) plane MEM charge densities of **(a)** Rb_2CsC_{60} and **(b)** Li_2CsC_{60}. Contour lines are drawn from 0.0 to 5.0 e Å^{-3} with 0.5 e Å^{-3} intervals.*

The results are shown in Table I. Since it is well known that there is significant site exchange between the octahedral and tetrahedral sites for the present materials, a deficiency of charges at each site must be affected by the site exchange for each material. By taking possible site exchanges into account, it should be noted that these values cannot be considered the absolute valence of the atoms. However, it is evident that the total value, which must be a much more reliable value than that of each site, decreases as Tc decreases. This implies the charge transfer from the doped metal atoms to the C_{60} molecule could be a crucial factor for creation of superconducting fullerides. From the crystal structural point of view, the difference in the strength of interaction between the metal atoms and the C_{60} molecule seems to cause the difference for the disordered state of the C_{60} cage in a crystal, *i.e.*, the much stronger interaction between alkali metal atoms and C_{60} prevents free rotation of the C_{60} cage in Rb_2CsC_{60}. In the present electron level structural study, it was found that there are distinct structural differences relating to the superconducting

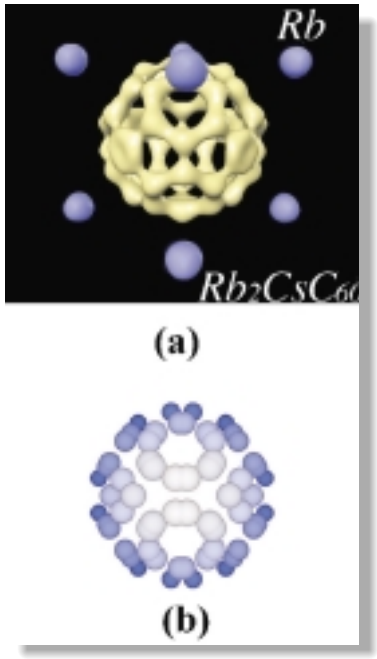

*Fig. 2: **(a)** Equi-contour (2.0 e Å^{-3}) density map for the MEM charge densities for Rb_2CsC_{60}. **(b)** Merohedral disorder model of C_{60}.*

Table I . Deficiency of charge at tetrahedral, octahedral sites and the total.

	Li_2CsC_{60}	Rb_2CsC_{60}
Tetrahedral site	0.3(1) e	2.1(2) e
Octahedral site	0.2(1) e	2.0(2) e
Total value	**0.5(2) e**	**4.1(4) e**

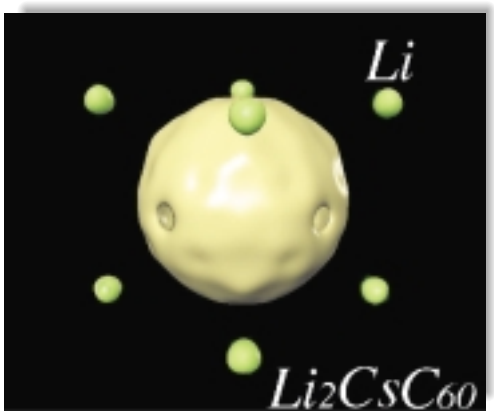

Fig. 3: Three-dimensional equi-contour (2.0 e Å^{-3}) density map of Li_2CsC_{60} .

Makoto Sakata[a] and Masaki Takata[b]
(a) Nagoya University
(b) Shimane University

E-mail : a40366a@nucc.cc.nagoya-u.ac.jp

References

[1] P.W. Stephens *et al., Nature* **351** (1991) 632.
[2] R.M. Fleming *et al., Nature* **352** (1991) 787.
[3] K. Tanigaki *et al., Nature* **356** (1992) 419.
[4] I. Hirosawa *et al., Science* **264** (1994) 1294.
[5] M. Takata *et al., Jpn. J. Appl. Phys.* in press (1999).
[6] M. Sakata and M. Sato, *Acta Cryst. A* **46** (1990) 263.

NUCLEAR RESONANT INELASTIC AND QUASI-ELASTIC SCATTERING EXPERIMENTS

Nuclear resonant inelastic scattering has many interesting features, and one of the most important is that it is possible to excite a specific nuclides [1]. For the compounds composed of more than one element, not all of the atomic motions are the same, and they depend on their mass differences, binding states and atomic positions. Furthermore, in a solution that contains different kinds of ions, the motion of each ion is different. For atomic motions limited to one- or two-dimensional regions, it is desirable to observe only their intrinsic dynamics without the influence of the surroundings. The nuclear resonant scattering method is effective for these areas of research and is expected to be a new tool for the study of dynamics of atoms. We have measured nuclear resonant inelastic and quasi-elastic scattering for several samples at the beamline **BL09XU**. Here, we introduce two examples of these.

Graphite is a typical layered material, which intercalates various atoms. Intercalated graphites show various stage structures depending on the sample preparations. We synthesized stage-1 graphite-ferric-chloride-intercalation compounds and measured the phonon energy spectra [2]. Our purpose is to study the dynamics of ferric chloride confined in the layers by observing the phonon densities of states projected to the layer direction and its vertical direction [3]. Energy spectra of nuclear resonant inelastic scattering were measured for two angles (0˚ and 90˚) between the direction of incident X-ray and the normal to the graphite layers.

The experimental setup is shown in Figure 1, and the observed spectra are shown in Figure 2. When the incident X-ray direction is parallel to the graphite layers, phonon modes with parallel components to the layers are excited. In case the incident X-ray direction is perpendicular to the graphite layers, phonon modes with perpendicular components to the layers are excited. The observed phonon modes parallel and perpendicular to the layers increase below 5 meV and around 10 meV, respectively. That is, the phonon modes

perpendicular to the layers are harder than those parallel to the layers. Because of the small recoilless fraction, multi-phonon contributions in the observed spectra are estimated to be large at room temperature from Mössbauer measurements. Though the angular dependence of the spectra are somewhat obscured by the multi-phonon contributions, an angular-dependent difference is observed.

This method is applicable to studying the dynamics of atoms in liquids, and, in a simple case, we can obtain the diffusion constant of the atoms. Quasi-elastic scattering was measured on iron ions in a Nafion membrane [4], which is of particular interest as an ion exchange membrane. In a water-soaked Nafion membrane, hydrated ferrous ions are assumed to exist in a region surrounded by sulphonic groups. The motion of ferrous ions was studied by Mössbauer spectroscopy below 250 K and is thought to be diffusive. As the membrane is usually used at room temperature, the motion at room temperature is important. It has been difficult to know the dynamics of ferrous ions at room temperature. However, the nuclear resonant quasi-elastic scattering method has made it possible to study the dynamics at room temperature. The measured spectrum is shown in Figure 3. The width of the monochromator resolution function is 6.5 meV, but the width of the spectrum is about 12 meV. This broadening is due to the diffusive motion of ferrous ions in the soaked Nafion membrane at room temperature. This indicates that the ions in the Nafion membrane move as in a solution.

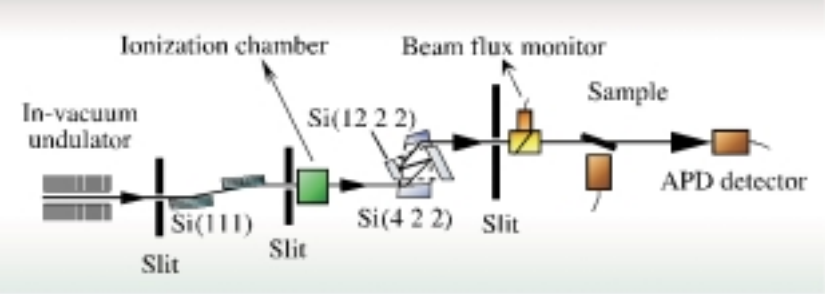

Fig.1: Experimental setup.

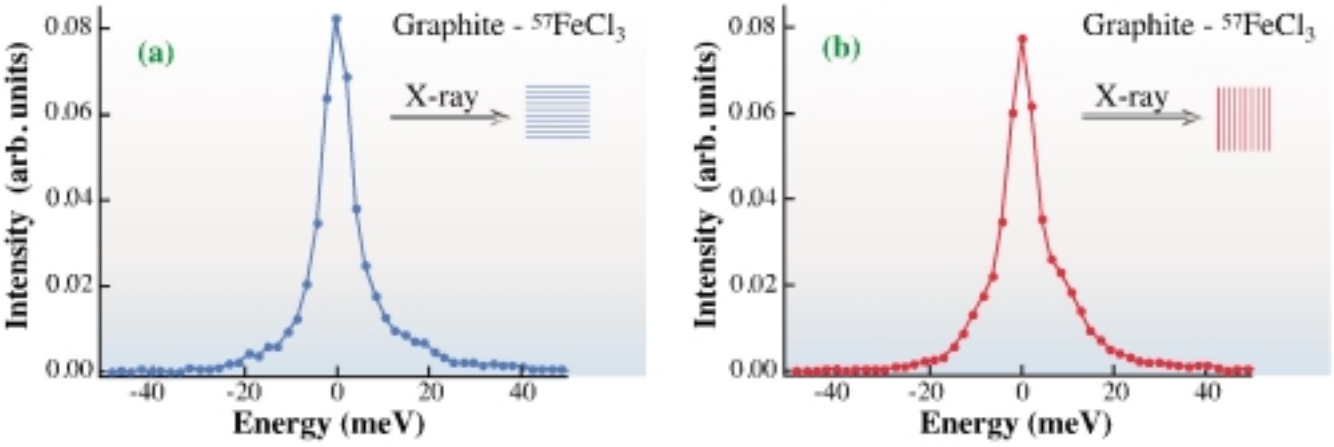

*Fig. 2: Nuclear resonant inelastic scattering of stage-1 graphite-$^{57}FeCl_3$ intercalation compounds at 298 K. Incident X-ray direction is **(a)** parallel and **(b)** perpendicular to the graphite layers.*

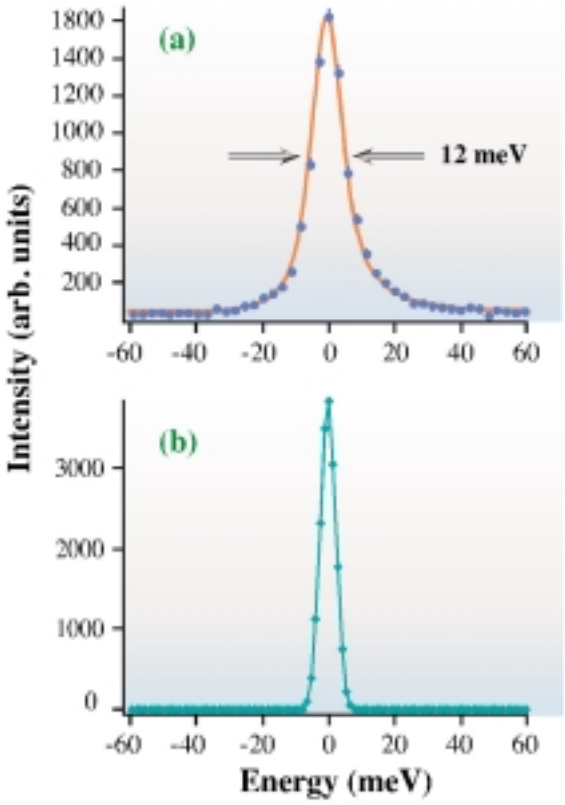

Fig. 3: ***(a)*** *Nuclear resonant quasi-elastic scattering from ^{57}Fe ions in Nafion.*
(b) *Nuclear resonant forward scattering from ^{57}Fe foil.*

OBSERVATION OF MAGNETIC RELAXATION IN AN $^{57}FeBO_3$ CRYSTAL BY USING NUCLEAR FORWARD SCATTERING

The Mössbauer time-domain spectroscopy using synchrotron radiation is suitable for the study of periodically perturbed nuclear resonant scattering. The time divided measurements are realized by phase-locking the periodic perturbation to the SR pulse. The quantum beats and dynamical beats give us information on the hyperfine interactions, the nuclear excited states and the motion of the resonant atom [1,2]. Recently, by applying the polarimetry technique, it has been shown that the oscillation of a hyperfine field on the plane perpendicular to the light axis can change the direction of the electric field vector of nuclear forward scattering (NFS) [3] (Figure 1).

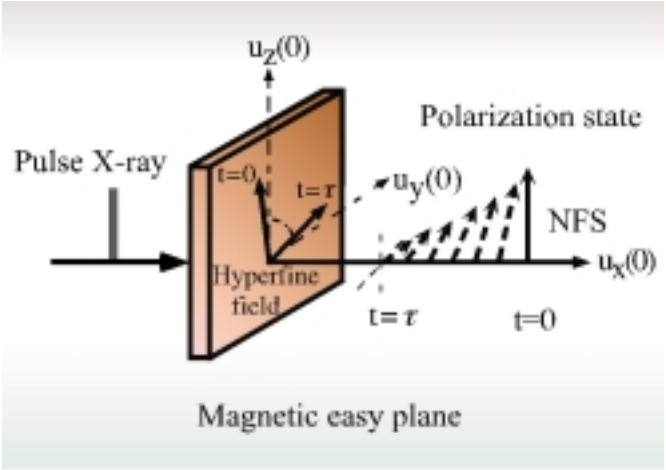

Fig. 1: Rotation of the polarization plane of NFS.

Makoto Seto[a], Rie Haruki[a] and Shinji Kitao[b]
(a) Kyoto University
(b) SPring-8 / JAERI

E-mail: seto@rri.kyoto-u.ac.jp

References

[1] M. Seto *et al., Phys. Rev. Lett.* **74** (1995) 3828.
[2] S. Kitao *et al.*, to be published in *Jpn. J. Appl. Phys. Suppl.*
[3] A. I. Chumakov *et al., Phys. Rev. B* **56** (1997) 10758.
[4] R. Haruki *et al.*, in preparation.

In the present study, we investigated the beam properties of NFS in the magnetic relaxation system of the $^{57}FeBO_3$ antiferromagnetic single crystal. The experiment was performed at the undulator beamline **BL09XU**. The storage ring was operated in 21-bunch mode at 20 mA. A SR pulse was emitted only at 228 ns intervals with a typically 50 ps width. The experimental setup is shown in Figure 2. The magnetic relaxation was caused by the fall-off of the external pulse magnetic field. Then, the

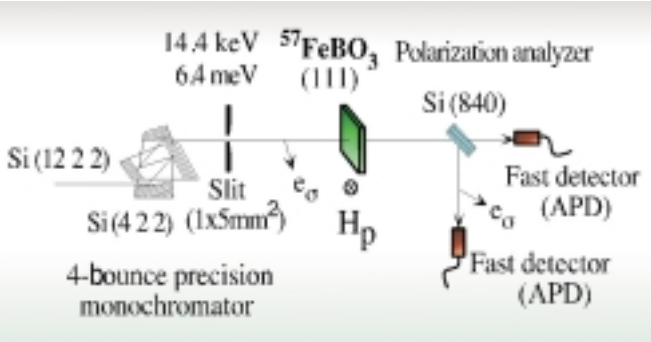

Fig. 2: Experimental setup.

magnetically unstable multidomain state (electron spin fluctuation system) was excited in the $^{57}FeBO_3$ single crystal over the magnetic relaxation time [4]. The magnetic field was phase-locked to the SR pulse signal. (Magnetic field parameters: strength 28 Oe, pulse width 80 ns, fall-off time 7 ns, frequency ~400 kHz.) The M ssbauer time spectra were measured with and without a Si(840) polarization analyzer crystal. (This crystal reflects only the s -polarized X-ray.) We measured eleven spectra at the intervals of 228 ns in the time range of 2.5 ms after the fall-off.

The normalized time spectra measured after 140 ns from the fall-off time are shown in Figure 3. From the comparison of plots (a) and (b) in Fig. 3, the intensity of the time spectrum with Si(840) is clearly lower.

This is explained as follows, at the instance of SR incidence after the fall-off time, NFS from the $^{57}FeBO_3$ crystal plate occurs with the σ -polarization as a result of nuclear transitions with $\Delta m = 0, -1$. Then, each magnetization (electron spin) vector in the multidomain of the crystal rotates randomly on the magnetic easy plane, $^{57}FeBO_3$ (111), due to the magnetic relaxation, and the hyperfine fields also rotate randomly. Therefore, the electric field vector of NFS is changed from the s -polarization to the mixed polarization. In our experimental arrangement, the π -polarized component of NFS cannot reach the detector in the case of using the analyzer crystal Si(840). As a result, the time spectra with Si(840) are reduced according to the mean velocity of the atomic spin rotation in the target material. A depolarization factor expressing the speed of the polarization mixing of NFS over the magnetic relaxation time, $\tilde{P}(t) = \tilde{I}^{\pi+\sigma}(t) - \tilde{I}^{\sigma}(t) / \tilde{I}^{\pi+\sigma}(t)$, was obtained from the time spectra with and without Si(840). Here, $\tilde{I}(t)$ is the normalized integrated intensity of the time spectra in the specific time range. The specific time ranges were set at 10~20 ns (fast rotation: This value is comparable to a nuclear Larmor precession time of $^{57}FeBO_3$ crystal) and 20~60 ns (slow rotation) in the time spectra. The corresponding parameter $\tilde{P}(t)$ of each time spectrum is shown in Figure 4. This figure indicates that, during 2.5 μs

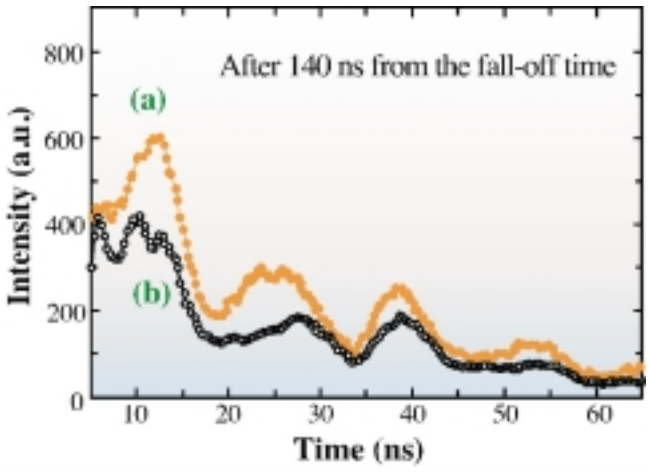

Fig. 3: Time spectra of the perturbed NFS.
***(a)** without and **(b)** with Si(840) polarization analyzer.*

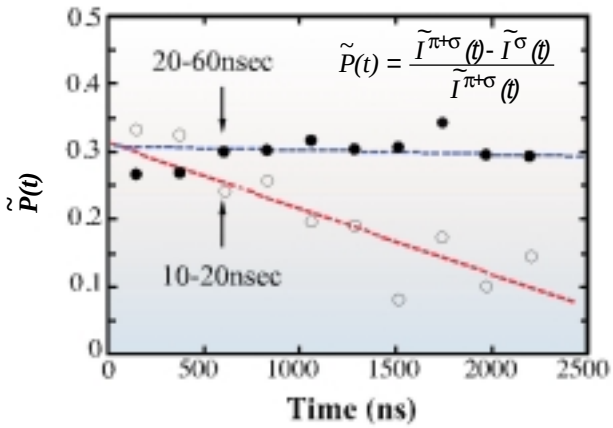

Fig. 4: Time dependent depolarization factor.

fall-off time, $\tilde{P}(t)_{10\sim20ns}$ shows a speedy reduction, whereas $\tilde{P}(t)_{10\sim60ns}$ keeps a nearly fixed value. Fluctuation of the magnetic moment in the crystal is decreased by the time development of the magnetic relaxation.

Takaya Mitsui
SPring-8 / JAERI

E-mail: taka@sp8sun.spring8.or.jp

References

[1] Yu.V. Shvyd'ko, *Hyp. Interact.* **90** (1994) 287.
[2] T. Mitsui *et al., Jpn. J. Appl. Phys.* **36** (1997) 6525.
[3] T. Mitsui *et al., Hyp. Interact.* (c) **3** (1998) 429.
[4] S. Kikuta, *Hyp. Interact.* **90** (1994) 335.

TIME AND ENERGY SPECTRA OF INTERNAL CONVERSION ELECTRONS FROM ^{57}Fe FOIL

Energy distribution and time spectra of internal conversion electrons from ^{57}Fe foil were measured at the **BL09XU** beamline. The emission signal of conversion electrons excited with incident X-ray photons was discriminated by electron energy analysis and intense prompt noise was excluded in the signal processing. The apparatus consists of an electrostatic electron energy analyzer and a sample manipulator contained in an ultrahigh vacuum chamber. The analyzer we developed was a planar electrostatic quadrupole type assembled on a 203 mm Conflat-type flange. The electrons incident through an entrance slit of the analyzer were deflected at an angle of 90˚ inside the hyperbolic electrostatic field. The acceptance angle and the energy resolution were 0.04 π and 4%, respectively.

An avalanche photodiode (APD) detector was attached at the exit of the analyzer. The APD detector proved high detection efficiency for high-energy electrons as well as excellent time response (< 1 ns) and noise characteristics (< 0.01 cps). The photons from an in-vacuum undulator are monochromatized to a band-width of 2 meV by a high-resolution nested channel-cut monochromator. The counting rate of APD detector for the prompt emission of photoelectrons was 1.4 x 10^6 cps. The energy spectrum of the electrons excited with a 14.413 keV X-ray is shown in Figure 1. To suppress the enormous counting rate of prompt emission of photoelectrons, the output pulse of the APD detector is discriminated in the time-domain between 10 and 190 ns after the incidence of synchrotron radiation. The peaks of K- and L-shell conversion electrons and KLL Auger electrons are clearly observed in the figure. The maximum counting rate at the peak energy of K-shell conversion electrons was 0.51 cps. The tail in the low energy side is due to the cascade inelastic scattering of electrons inside the sample. The energy resolution of 4% corresponds to the escape depth of 20 nm.

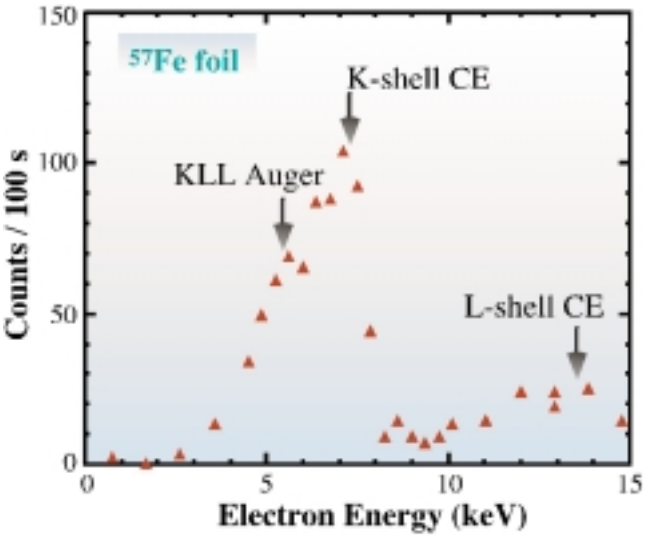

Fig.1: Energy distribution of electron emission from ^{57}Fe foil within a time-interval between 10 and 190 ns after incidence of primary photons.

The time spectrum of the K-shell conversion electrons is shown in Figure 2. The principal structure of the time spectrum is an exponential decay with the time constant of 131±17 ns, which coincides with the decay time of isolated ^{57}Fe nuclei, 141 ns. Compared with the time spectrum of the nuclear resonant photon emission for the same sample, neither the speed-up of decay process nor quantum beat structure is observed. The present results illustrate the incoherent nature and surface layer sensitivity of conversion electron emission.

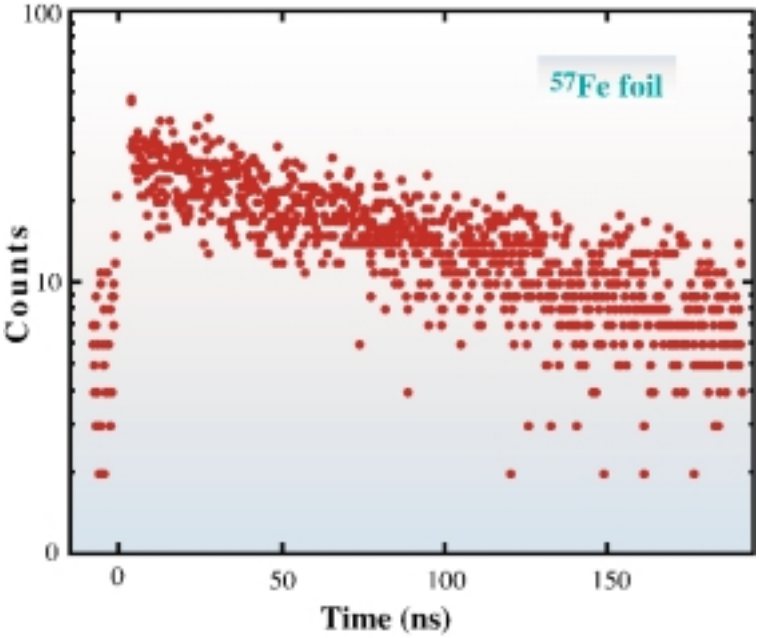

Fig. 2.: Time spectrum of K-shell conversion electrons from ^{57}Fe foil. Accumulation time of the spectrum was 7.8 hours.

Tatsuo Okano[a], Taizo Kawauchi[a] and Zhang Xiao-Wei[b]
(a) The University of Tokyo
(b) KEK

E-mail: okano@iis.u-tokyo.ac.jp

T.Okano, T.Kawauchi, X.-W. Zhang, K.Fukutani, Y.Yoda, U. Teerapongpipat and S.Kikuta, Submitted to *Japan J. Appl. Phys.*

X-RAY PARAMETRIC DOWN CONVERSION AT THE BREWSTER ANGLE

X-ray parametric down conversion originating from the property of free electrons is one of the nonlinear phenomena in the X-ray region. The phenomenon that one X-ray photon is converted to two photons was observed by Eisenberger *et al.* using an X-ray tube [1] and by Yoda *et al.* using synchrotron radiation [2]. The polarization dependence in X-ray parametric down conversion is different not only from that in Thomson scattering but also from that in optical parametric conversion. In the latter case, the spatial symmetry of a nonlinear optical medium restricts the form of the nonlinear optical susceptibility. The X-ray parametric down conversion was observed in such a geometry that the π -polarized X-rays are incident on the crystal at the Brewster angle where Thomson scattering is prohibited.

The experiment was performed at the beamline **BL09XU**. The linear polarized X-rays in the horizontal plane can be obtained by the in-vacuum horizontal undulator. The storage ring was operated in multi-bunch mode with 2 nsec pulse intervals and its typical current was 17 mA. X-rays from a Si (111) inclined double-crystal monochromator were incident on a diamond single crystal as shown in Figure 1.

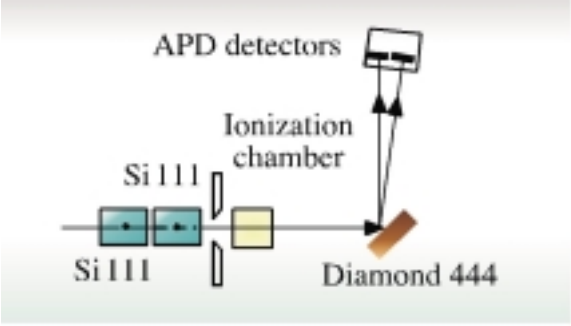

Fig.1: Experimental setup. Two APD detectors were arranged at scattering angles of nearly 90 degrees.

The combination of 0.72 Å wavelength of the monochromatized X-rays and the (444) reflection of diamond makes the Brewster angle. The symmetric Bragg-case was employed for the phase matching of parametric down conversion. Two avalanche photodiode (APD) detectors of 5 mm^2 were placed on the scattering plane with their centers 18 mm apart so as to be symmetric around the direction of the Bragg reflection. The coincidence technique with a time resolution of 1.5 nsec was used. The distance between the diamond crystal and the APD detectors was 290 mm.

The π-polarized X-ray beam was incident on the diamond crystal. The coincidence measurement was made by rotating the crystal step by step with a measuring time of 2850 sec at each point. The coincidence rate was obtained by subtracting the accidental coincidence, as plotted by solid circles in Figure 2. The Bragg reflection intensity is also plotted by open circles. The peak of Bragg reflection does not appear if the incident X-rays are 100% linear-polarized.

The coincidence peak is clearly seen at the higher angle side of the Bragg reflection peak, and its peak position agrees well with the estimated value 95 arcsec. The coincidence rate at the peak was 0.05 counts/sec and the accidental coincidence rate estimated from the counts at each detector was 0.001 counts/hour at most. At the peak position of the coincidence rate, the change in the coincidence rate was measured as a function of the time difference caused by two delay-cable lengths of the electronic circuits. No signal was counted in the region where the delay time was more than 1.5 nsec. This means that the peak of the coincidence rate in the angular scan is definitely formed owing to the simultaneous detection by the two detectors. The measured degree of linear polarization of the incident X-rays was 99.7%, and another measurement using σ-polarized incident X-rays at 90° showed that 0.3% σ-polarized incident X-rays did not contribute to the coincidence peak in Figure 2. Measurement at the Brewster angle will be effective to reduce the background noise in the experiment of X-ray parametric down conversion.

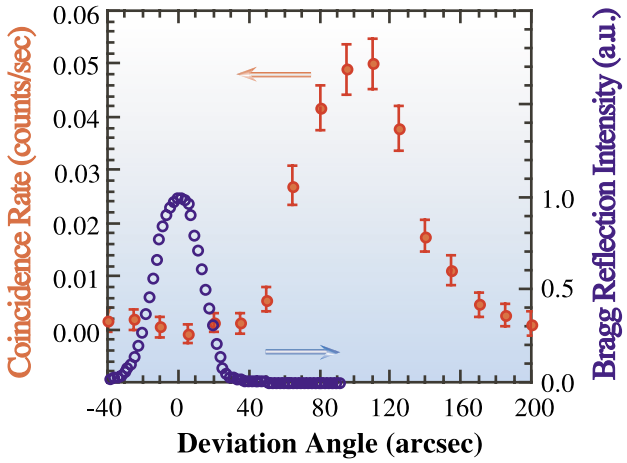

Fig. 2: Yield of X-ray parametric down conversion as a function of rotation angle of the diamond crystal. Red solid circles: coincidence rate of two APD detectors. Blue open circles: Bragg reflection intensity detected by one APD detector placed in the Bragg reflection direction.

Yoshitaka Yoda and Seishi Kikuta
SPring-8 / JASRI

E-mail: yoda@spring8.or.jp

References

[1] P. Eisenberger and S.L. McCall, *Phys. Rev. Lett.* **26** (1971) 684.
[2] Y. Yoda et al., *J. Synchrotron Rad.* **5** (1998) 980.

XAFS

X-ray absorption spectroscopy attracted the attention of only a handful of professional people in the early days, and no one was sure what kind of structural information could be extracted from the measurement. Around 1980, however, a new theory emerged which showed that distances to neighboring atoms from a selected element in amorphous materials can be determined by Fourier analysis of the wigglers that appear in absorption spectra. At the same time, several synchrotron radiation facilities started to supply intense white X-rays, improving the quality of the data by several orders of magnitude.

Since then, X-ray absorption fine structure spectroscopy or XAFS has been thriving at every synchrotron facility around the world, the number of which is increasing year by year. Unfortunately, however, X-rays available at most SR facilities are up to 25 keV or so, limiting such K-edge XAFS studies to elements with an atomic number less than ~ 45.

Now at SPring-8, X-rays up to almost 100 keV are available with sufficient intensity for XAFS studies. Hence, heavy elements can be investigated by K-edge XAFS, without resorting to L edges. By increasing the storage current in the near future, in addition to the high brilliance already achieved, various ambitious XAFS studies will be possible, from very dilute biological materials to very small samples in high-pressure vessel. While the search continues for scientific culmination, various routine XAFS measurements will also be carried out for both basic scientific and industrial applications .

Yasuo Udagawa

DIRECT EVIDENCE FOR ENDOHEDRAL STRUCTURE OF EuC_{60}

Since the discovery of $M_x@C_y$ at the beginning of the 90's, metal endohedral fullerenes ($M_x@C_y$, M: atom), in which M is expected to exist inside the fullerene cage, have attracted the interest of both chemists and physicists for their intrinsic potentials upon application to superconductors and organic ferromagnets. The establishment of the "endohedral structure", however, has not been straightforward chiefly because of difficulties in getting enough samples for structure analyses.

In 1995, Takata et al. first obtained direct evidence of the "endohedral structure" in $Y@C_{82}$ by applying the maximum entropy method to powder X-ray diffraction with synchrotron radiation [1]. The electron density of Y atoms exists inside the C_{82} .

Recently, the similar structures of several other $M_x@C_y$ have also been identified, except for $M@C_{60}$.

In 1996, we succeeded in obtaining a $M@C_{60}$-enriched solution by using the high-pressure liquid chromatography (HPLC) with aniline as the eluent [2,3]. However, its "endohedral structure" could not be confirmed due to the unavailability of a powder-sample with suitable purity. Recently, we found that soot prepared by the arc-heating of a graphite rod containing Eu_2O_3 showed a large amount of EuC_{60} compared with other fullerenes, as seen in the laser desorption time-of-flight (LD-TOF) mass spectrum shown in Figure 1.

We herewith report the structure of EuC_{60} obtained from EXAFS. The Eu LIII-edge XAFS spectrum of soot containing EuC_{60} was measured at room temperature in the transmission mode with an double-crystal Si(111) monochromator at the beamline **BL01B1**. Rh mirror was inserted in order to eliminate the harmonics. Figure 2 shows the radial structure function $\Phi(r)$ obtained by the Fourier transform of $k^3\chi(k)$. The imaginary part of $\Phi(r)$ showed two pronounced peaks at 1.63 and 2.08 , which could be assigned to the two Eu-C scatterings. The distance and the mean square displacement between the Eu and the first neighboring C atoms, $r_{Eu\text{-}C(1)}$ and $\sigma_1(2)$, and those between the Eu atom and the second neighboring C atoms, $r_{Eu\text{-}C(2)}$ and $\sigma_2(2)$, were determined by a least-squares parameter-fitting to the EXAFS spectrum obtained using the inverse Fourier transform of the $\Phi(r)$ as shown in Figure 2. The number of the first and the second neighboring C atoms were fixed both at six by assuming that the Eu atom lays on a six-membered ring in the C_{60} cage. The $r_{Eu\text{-}C(1)}$ and $r_{Eu\text{-}C(2)}$ were 2.338(8) and 2.84(1) , and the $\sigma_1(2)$ and $\sigma_2(2)$

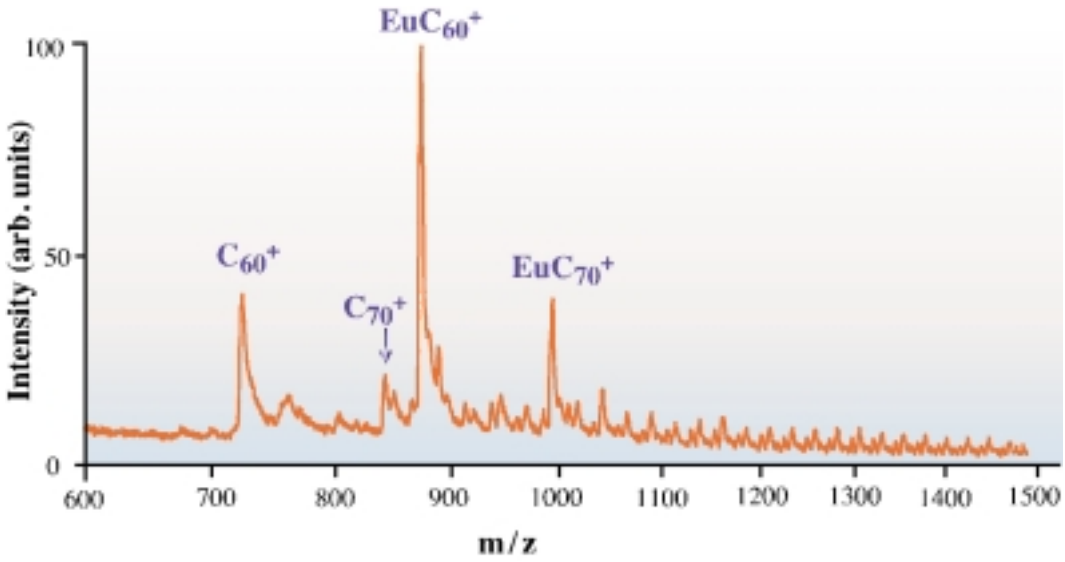

Fig. 1: LD-TOF mass spectrum for the soot prepared by arc-heating of graphite/Eu_2O_3 composite rods. Courtesy of IUCr.

were 0.0048(6) and 0.006(1) $Å_2$, respectively.

The $r_{Eu\text{-}C(2)}$, 2.338 Å clearly indicates that the location of the Eu atom is inside the C_{60} cage because $r_{Eu\text{-}C(2)}$ should be 3.73 Å long if the Eu atom is located outside the cage. This is the first direct evidence for the "endohedral structure" for M@C_{60}.

Figure 3 shows a schematic representation for the position of the Eu atom which is 1.4 Å off from the cage center. The XANES spectrum of the soot, shown in Figure 4, is composed of two components, suggesting that the oxidation state of the Eu atom is the mixed-valence of Eu^{+2} and Eu^{+3}.

We are planning to measure X-ray powder diffraction with synchrotron radiation to determine the three-dimensional structure for M@C_{60}.

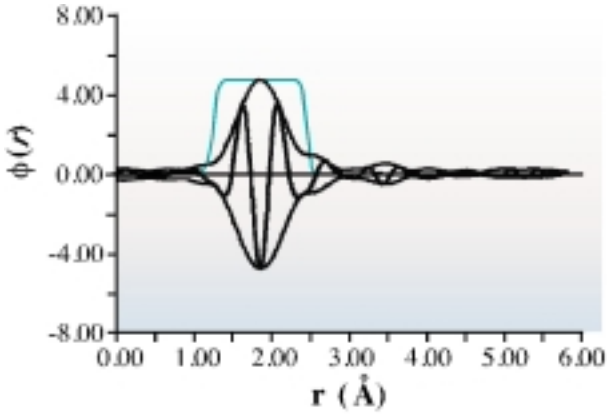

Fig. 2: Φ(r) obtained from XAFS for soot. The part used for the inverse Fourier transform is shown in the spectrum, by rectangular function. Courtesy of IUCr.

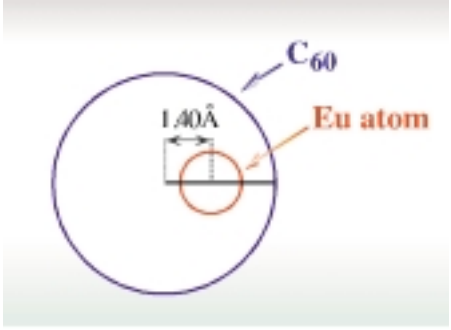

Fig. 3: Schematic representation for Eu@C_{60} .

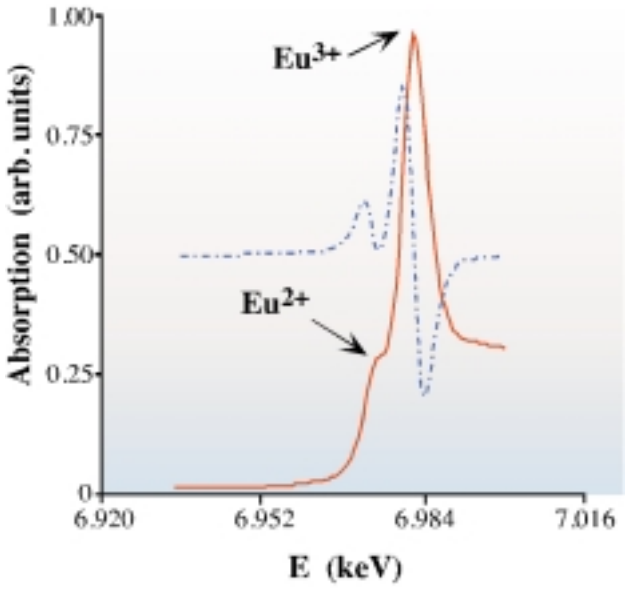

Fig. 4: XANES spectrum for soot. Dashed line is a derivative of the spectrum.

Yoshihiro Kubozono, Takashi Inoue and S. Kashino
Okayama University

E-mail: kubozono@cc.okayama-u.ac.jp

References

[1] M. Takata *et al., Nature* **377** (1995) 46 .
[2] Y. Kubozono *et al., J. Am. Chem. Soc.* **118** (1996) 6998.
[3] Y. Kubozono *et al., Chem. Lett.* **1061** (1996).

SOLVATION STRUCTURES FOR IODIDE ANIONS IN VARIOUS SOLVENTS BY EXAFS

Halide anions are the most common anions, in existence everywhere, from seawater to our bodies. The solvation structures for such important ions, however, are not well understood owing to their weak interaction with solvent molecules. The weak interaction may be reflected in their various reported hydration numbers, from zero to seven or eight depending upon the methods employed to determine them [1].

The weakening order in interaction with water molecule, $Cl^- > Br^- > I^-$, has been shown through studies on solvation enthalpy, by solvent extraction or liquid chromatography. It is of great interest to elucidate and compare the differences in solvation structure of these anions.

Our previous EXAFS study on bromide anion [2] verified suitability of the EXAFS method for determining local structures of ions dissolved in water, or in organic solvents where ion-solvent interaction is even weaker. However, the EXAFS method using conventional X-ray conditions has not been ideally suited to chloride and iodide due to the extremely low absorption edge energy of the former and, on the other hand, the very high edge energy (33 keV) of the latter. Therefore, bromide has been the only candidate for EXAFS experiments among the three ions.

Using SPring-8 X-rays, we are now able to explore the XAFS of iodide anions in various solvents and compare the results with those of bromide ions. The beamline **BL01B1** is used to obtain XAFS spectra by a transmission method at the I K-edge. It is equipped with a double-crystal monochromator and a double-mirror system, which effectively removes higher harmonic photons.

EXAFS oscillation signals $k^3\chi(k)$ have been extracted from absorption spectra for 0.1 mol/dm^3 iodide anions dissolved in several solvents and some of them are displayed in Figure 1. The small oscillation amplitudes and noisy spectra are due to two reasons, *i.e.*, first, the weakest interaction of iodide anions with solvents among the three halide anions, and second, the shortest lifetime of its core-hole state. In Fourier transformed (FT) spectra of the $k^3\chi(k)$ data, the identification of peaks was easy due to the atom-atom interaction between iodide anions and oxygen or carbon atoms in solvent molecules.

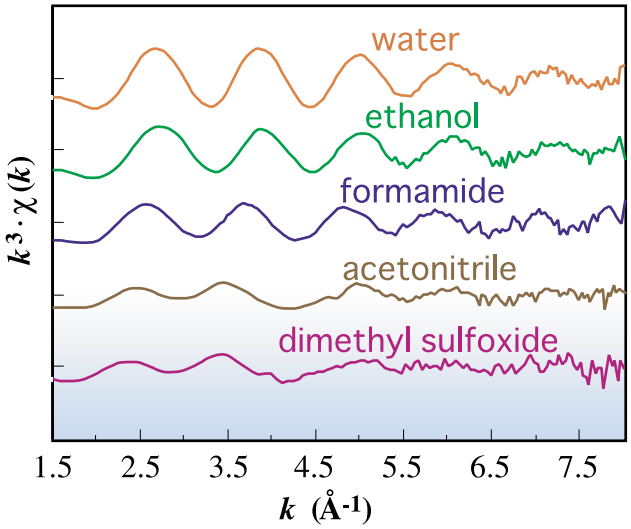

Fig. 1: EXAFS oscillation spectra $k^3\chi(k)$ for iodide anions dissolved in solvents.

The amplitude of the EXAFS oscillations in Figure 1 can be evaluated by using intensity h of the peak in the FT spectrum. It is interesting that a correlation exists between h and an empirical solvent parameter obtained from NMR measurement, the Mayer-Gutmann acceptor number A_N [3], indicating the strength of interaction between donor solute and acceptor solvent.

The correlation of h with A_N shown in Figure 2 is interpreted as follows. The oscillation amplitude will be greater for ions with a larger number of coordinating atoms N and also with a smaller disorder σ in the atom-atom distance. A larger N leads to greater electrostatic solute-solvent interaction and a smaller σ means a stronger solute-solvent bond. Therefore, h is intimately related to the solute-solvent interaction strength.

The present study suggests that EXAFS has been not only a quantitative tool to determine the geometrical structure, but also can be extended to become a qualitative tool for such complicated systems like a solution for which many empirical parameters are of practical use.

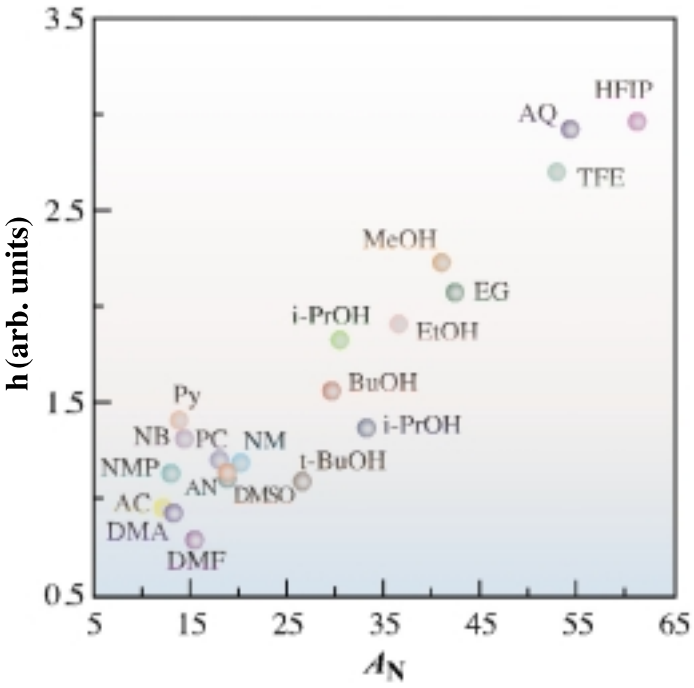

Fig. 2. Correlation of the first shell peak height h in an FT spectrum with acceptor number A_N of the solvent. HFIP for 1,1,1,3,3,3-hexafluoroisopropanol, AQ for water, TFE for 2,2,2-trifluoroethanol, EG for ethylene glycol, MeOH for methanol, EtOH for ethanol, i-PrOH for isopropanol, PrOH for n-propanol, BuOH for n-butanol, t-BuOH for t-butanol, NM for nitromethane, AN for acetonitrile, DMSO for dimethyl sulfoxide, PC for propylene carbonate, DMF for N,N-dimethylformamide, NB for nitrobenzene, Py for pyridine, DMA for N,N-dimethylacetamide, NMP for N-methyl-2-pyrrolidone and AC for acetone.

Iwao Watanabe
Osaka University

E-mail: watanabe@chem.sci.osaka-u.ac.jp

References

[1] H. Ohtaki and T. Radnai, *Chem. Rev.* **93** (1993) 1157.
[2] H. Tanida *et al., J. Chem. Soc. Dalton Trans.* **2321** (1994).
[3] V. Gutmann, *The Donor-Acceptor Approach to Molecular Interactions*, Plenum, New York, 1978.

EXAFS STUDY ON LIQUID SELENIUM UNDER HIGH-PRESSURE

High-pressure XAFS enables structural information difficult to obtain through conventional high-pressure X-ray diffraction studies to be accessed. We have successfully measured XAFS spectra of crystalline and liquid Se at pressure of 2.5 GPa and temperatures up to 1223K at the beamline **BL01B1** [1].

Liquid Se is a typical liquid semiconductor at atmospheric pressure and its main constituents are two-fold coordinated chain molecules. Recently, study on the semiconductor-to-metal transition of liquid Se in the pressure range from 1 GPa to 4 GPa showed that the transition has some features of a first-order transition [2]. We focus on how structural changes of the Se system associate with the changes in its electronic properties.

A large-volume Paris-Edinburgh press was used to generate high-pressure, high-temperature conditions. A mixture of Se powder and BN powder was put in a BN capsule, which was surrounded by a gasket made of Boron and epoxy. The sample was heated using two graphite disk-type heaters inside the gasket. The beam was focused vertically by a mirror. The size of the X-ray beam was reduced to 0.3(H) x 0.2(V) mm^2 by slits to adjust to the small sample size. The intensities of the incident and transmitted X-rays were measured with ionization chambers.

Figure 1 shows an example of XAFS spectra for liquid Se measured at pressure of 2.5 GPa and temperature of 773 K. Clear EXAFS oscillations were observed in spite of experimental difficulties. Figure 2 shows the temperature dependence of radial distribution function, $|F(r)|$, obtained by the Fourier transform of EXAFS function $\chi(k)$ multiplied by k, for crystalline and liquid Se at 2.5 GPa. The main peak corresponds to the covalent bonds. The peak height decreases continuously with increasing temperature due to the thermal factor. The radial distribution function changes little upon melting; this indicates that the two-fold chain structure is largely preserved in the liquid. A steep

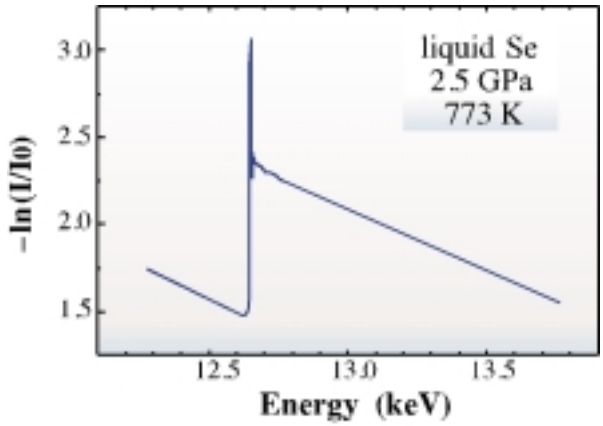

Fig. 1: XAFS spectra for liquid Se measured at pressure of 2.5 GPa and temperature of 773 K.

decrease in the amplitude of the EXAFS oscillation for liquid Se was observed above 1050 K. The decrease was larger than that expected from the normal thermal effect, and it indicates that the two-fold covalent bonds in liquid Se weaken and/or break under high-temperature. The change occurred near the boundary of the reported semiconductor-to-metal transition. This confirms that the transition is accompanied by a structural change.

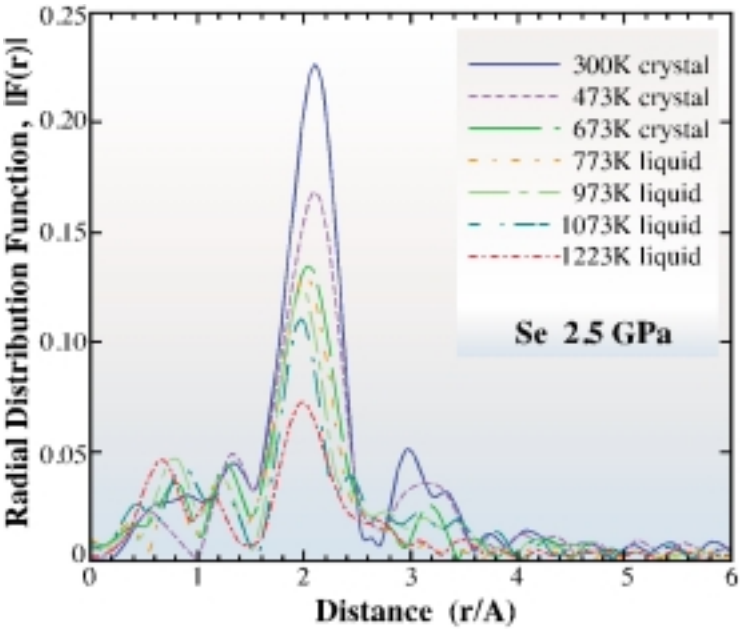

Fig. 2: Temperature dependence of radial distribution function, |F(r)|, obtained from EXAFS spectra, for crystalline and liquid Se at 2.5 GPa.

Yoshinori Katayama
SPring-8 / JAERI

E-mail: katayama@spring8.or.jp

References

[1] Y. Katayama et al., to be published in *J. Non-Crystalline Solids.*
[2] V.V. Brazhkin *et al., Phys. Lett. A* **166** (1992) 383.

XAFS SPECTRA IN THE HIGH ENERGY REGION

There is sufficient photon density even at 100 keV from a bending magnet at the SPring-8 storage ring. This enables qualitative XAFS spectra to be observed near K absorption edges for almost all heavy elements. Since an EXAFS signal above an L_{III} absorption edge is followed by an L_{II} absorption edge, the energy range is limited for the analysis. Therefore, EXAFS spectra with K absorption edges are anticipated in order to improve the accuracy of local structure parameters for elements, *e.g.*, lanthanoids. However, it has theoretically been pointed out that the finite lifetime of a core hole smears out EXAFS oscillations, and that this effect becomes more serious for K absorption edges of heavier elements [1,2].

Measurements were carried out at the beamline **BL01B1** in the transmission mode with the Si (511) planes of an adjustable inclined double-crystal monochromator, which is the standard monochromator at SPring-8 and can provide a wide energy range from 4.5 to 110 keV by inclining a pair of crystals. The incident and transmitted X-ray intensities were monitored with flowing Kr gas ionization chambers. It took 5 sec to monitor the X-ray intensities for each data point. The counting of higher-order harmonics was estimated to be less than 1% in comparison with that of the K edge energy, by considering both the photon flux of the source and the efficiency of the detector.

The highly brilliant X-rays of the third generation synchrotron radiation source enable us to measure XAFS spectra with better energy resolution than

before. Accordingly, the energy resolution near the Pt K edge was estimated to be 7 eV from the vertical size of the X-ray source (0.1 mm) and the width of the vertical slit at 47 m from the source (0.2 mm). Such an energy resolution allows us to discuss the EXAFS function even at low-k values. Since the width of the rocking curve of the monochromator crystal is sharp, the first crystal holder is equipped with a piezo-actuator to keep the crystals in parallel during a scan.

Figure 1**(a)** shows the X-ray absorption spectrum of Pt at room temperature. The width of the edge jump is as wide as 100 eV and dependent on the width of the initial state of the K level, Γ_K. The blunt edge jump makes it difficult to extract the EXAFS signal at low-k values, while the EXAFS signal is defined well up to 20 Å^{-1}, as shown in the inset.

The near-edge-structure is unusual in the ordinary sense. The energy at which the absorption saturates on average is converted to the wave number k = 6 Å^{-1}; the photoelectron has enough kinetic energy to transit between the central and neighboring atoms. The EXAFS oscillation of the outer shells seems to smear out. In particular, the amplitude of the EXAFS oscillation is reduced significantly at low-k values. It has been shown that local structure parameters such as the interatomic distance and the Debye-Waller factor obtained for the K edge are in good agreement with those obtained for the L_{III} edge.

Figure 1**(b)** shows the XAFS spectrum of the same sample at 12 K. The amplitude of the EXAFS oscillation increases considerably against the smearing effect due to the finite lifetime of the core hole, indicating that it is very sensitive to the Debye-Waller factor at high-k values. It has been shown that the K edge XAFS measurement in the high energy region is useful, which so far has been difficult. Very recently, we have succeeded in observing EXAFS oscillations above the Pb K edge (88.0 keV) at low temperatures.

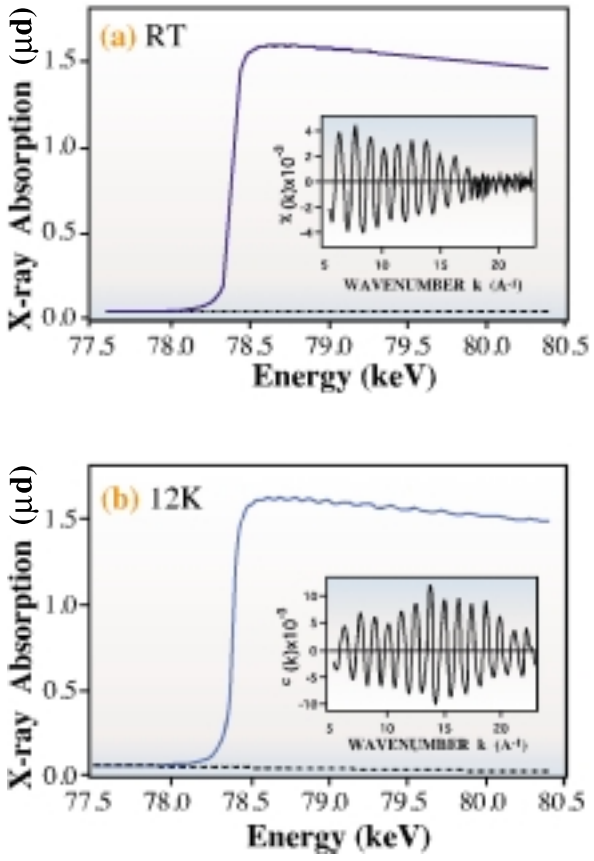

Fig. 1: XAFS spectra at the Pt K-edge for Pt foil ***(a)*** *at room temperature and* ***(b)*** *at 12K. Fig.1(a): courtesy of IUCr [2].*

Yasuo Nishihata
SPring-8 / JAERI

E-mail: yasuon@spring8.or.jp

References

[1] D. G. Stearns, *Philos. Mag.* **49** (1984) 541.
[2] Y. Nishihata *et al., J. Synchrotron Rad.* **5** (1998) 1007.

CAPACITANCE XAFS: SITE-SELECTIVE OBSERVATION OF CARRIER TRAPS IN SEMICONDUCTORS

Since the XAFS spectrum is obtained by measuring the X-ray absorption with an inner-shell excitation of a specific atom, the information related to the atom and its chemical environment can be obtained even though the atom is buried in a compound. However, if the atom has various local structures dependent on its chemical environment, the XAFS spectrum provides the average information of these local structures. This causes ambiguity of the XAFS analysis in relating the microscopic local structure to macroscopic material properties. Accordingly, there is a need for a site-selective XAFS, in which only the specific minor structure in the bulk structure can be detected.

We propose the "capacitance XAFS" by measuring the photon-energy dependence of the capacitance of the Schottky barrier diode as the site-selective XAFS for the local structure analysis of the low density carrier traps in semiconductors [1] . The concept of capacitance XAFS is shown in Figure 1. The DX center of AlGaAs:Se, which is a typical deep-level electron trap, is used as an example in this figure. In AlGaAs:Se, group-VI Se substitutes for the group-V site as the electron donor and is surrounded by group-III atoms. Under X-ray irradiation of this Schottky barrier diode, a core hole is formed in the Ga K-shell by X-ray absorption. If Ga in the DX center is excited, it is expected that the localized electron drops into the core hole, as shown in Figure 1**(a)**. Since the capacitance is proportional to the square root of the number of this electron relaxation in the carrier trap, the capacitance increases. In contrast, when the excited Ga is in the bulk AlGaAs instead of the DX center, it is relaxed by the capturing of the photoelectron, as indicated in Figure 1**(b)**. In this case, the capacitance is not changed, while the conventional XAFS by fluorescence detection predominantly reflects this absorption. Therefore, the photon-energy dependence of the capacitance is considered to correspond to the XAFS spectrum of only Ga in the DX center.

The capacitance XAFS analysis is applied to the observation of the DX center in $Al_{0.33}Ga_{0.67}As$:Se. The sample is grown by molecular beam epitaxy on a (100)-oriented n-type GaAs substrate. The Se concentration is $5x10^{17}/cm^3$. For the metal electrode of the Schottky diode, an Al dot ~0.5 mm in diameter and a thickness of ~100 nm is deposited by an evaporator. The hard X-rays can pass through this Al electrode. Experiments using synchrotron radiation are performed at the beamline **BL10XU**, a high brilliance XAFS station. The capacitance is measured by a capacitance meter with a 1 MHz oscillator.

As shown in Figure 2, a clear capacitance jump at the Ga K-edge and a XAFS oscillation are observed using this method (solid line). The conventional XAFS spectrum obtained using a solid state detector (SSD) is also shown in this figure (dashed line). An

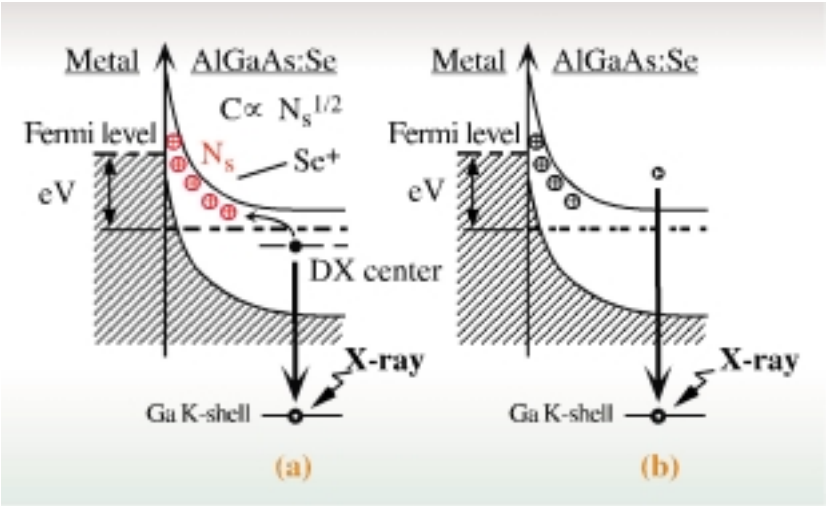

*Fig.1: Concept of the capacitance XAFS. X-ray absorption by carrier-trapping atoms **(a)** rather than bulk atoms **(b)** induces capacitance variation.*

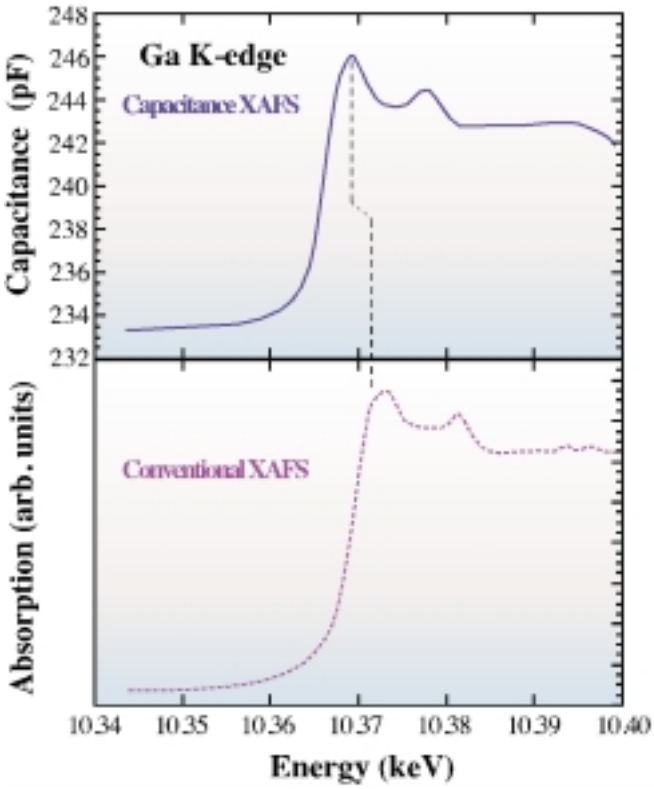

Fig.2: Photon-energy dependence of the capacitance of AlGaAs:Se at around Ga K-edge (solid line). The conventional XAFS spectrum obtained by using the SSD is also shown by dashed line.

energy shift of the absorption edge toward the low-energy side is observed in the capacitance XAFS, suggesting that only the Ga (<5x10^{17}/cm^3) neighboring Se, which constructs the DX center mixed in the bulk Ga (~1x10^{22}/cm^3), is selectively observed by the capacitance XAFS. The energy shift is considered to indicate the change in atomic coordination of Ga in the DX center. The capacitance XAFS spectrum provides direct evidence for the large lattice relaxation (LLR) model [2], in which Ga as the nearest neighbor of Se is displaced from the lattice site, instead of the donor itself, with the Ga-Se bond breaking.

Masashi Ishii
SPring-8 / JASRI

E-mail: ishiim@spring8.or.jp

References

[1] M. Ishii *et al., Appl. Phys. Lett.* **74** (1999) 2672.
[2] D. J. Chadi and K. J. Chang, *Phys. Rev. B* **39** (1989) 10063.

SPECTROSCOPY

The highly brilliant light from SPring-8 ranging from the hard to soft X-ray regions provides remarkable opportunities in the studies of electronic structures for a wide range of materials. Newly commissioned high performance beamlines for magnetic circular dichroism (BL39XU, BL25SU), Compton scattering (BL08W), nuclear resonant scattering (BL09XU) and photoemission spectroscopy (BL25SU) are beginning to produce important results that will have major impact on our understanding of condensed matter, primarily of magnetic materials.

In particular, a new helicity modulation technique for the hard X-ray region has been developed in SPring-8 for magnetic circular dichroism studies and has enabled the detection of signals weaker by orders of magnitude than that could be measured before, opening up new opportunities in the studies of magnetism, biology, etc. The photoemission experiments in the soft X-ray beamline are also unique in their energy resolution, the highest in the world in the soft X-ray region. This has enabled us to study fine structures near the Fermi level, such as Kondo peaks, using much higher photon energies than usually employed for such studies.

Atsushi Fujimori

XMCD MEASUREMENTS BY HELICITY MODULATION TECHNIQUE

Polarization properties may be one of the most promising items in the third generation SR. In particular, the polarization tunability is crucial for the measurement of magnetic effects through magneto-optical activity. Such measurement is attained by a combination of a linear undulator and a phase retarder, capable of controlling both linear and circular polarization states.

Diamond crystal functions as the phase retarder to convert linearly polarized X-rays, originally emitted from the undulator, to the circularly polarized state. Furthermore, it can alternate quickly between plus and minus helicities with almost circular polarization. In the energy range of hard X-rays, a diamond phase plate is suitable for modulating the photon helicity because of the high perfect-crystallinity and high transmittance. A helicity modulation technique has been successfully developed using the phase retarder with a synthetic diamond installed on **BL39XU** [1]. The efficiency of this technique has been demonstrated by a remarkable improvement in the accuracy of the X-ray magnetic circular dichroism (XMCD) at the Fe K-edge in Fe ferromagnetic compounds.

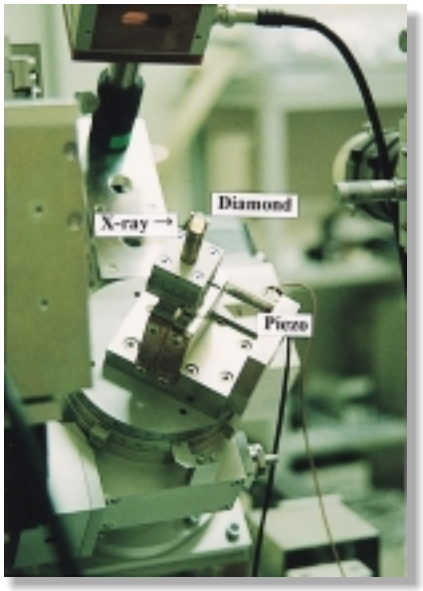

Fig.1: Assembly of the phase retarder. The diamond phase plate is fixed in a piezo-driven stage mounted on a 2-circle goniometer.

A diamond (111) slab 0.5 mm thick is used in the Laue geometry with 220 symmetric reflection plane tilted by 45° from the polarization plane of the incident beam. The phase plate can be operated by a piezo-driven oscillation stage. Figure 1 shows the phase retarder assembly.

Fast switching of the photon helicity is effectuated by flipping between plus and minus offset angles around the Bragg condition, previously determined from polarization measurements of the transmitted beam. The X-ray intensity as a function of the offset angle is shown in Figure 2. The photon helicity was alternately tuned at 40 Hz. The absorption

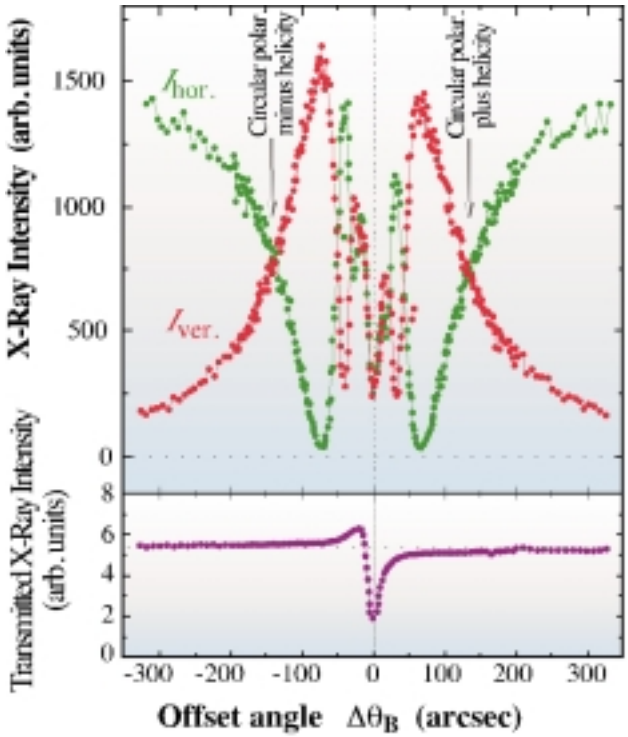

Fig. 2: Measured variations of X-ray intensities versus the offset angle with respect to the Bragg angle in the energy range of 8 keV. The vertical component is equal to the horizontal one at ±140 arcseconds, where the polarization state of the transmitted X-ray is converted into circular polarization. The phase retarder can also function as a λ/2-phase plate, that is, the polarization plane is rotated from horizontal to vertical at around ±70 arcseconds.

coefficient was monitored through a logarithmic converter circuit, and the XMCD signal was directly measured by a lock-in amplifier referring to the frequency of helicity alternation under a fixed magnetic field of 0.6 T.

Figure 3 shows an XMCD spectrum at the Fe *K* edge in ferromagnetic Fe_4N. The spectrum indicates that the experimental error is reduced to less than 10^{-4} and that a high signal-to-noise ratio can be obtained in the entire energy range measured. It took only about 60 min to record the spectrum. This was sufficient to ensure a high statistical accuracy. Hence, the measurement time can be reduced by an order of magnitude in comparison with the conventional method. Some fine structures are clearly resolved around the absorption edge, which is characterized by a positive and acute peak observed at just the threshold. Accordingly, this spectrum may be interpreted in the context of covalency due to charge transfer from the ligand atoms.

The helicity-modulation technique is also applicable to XMCD measurements under extreme condition (*e.g.*, high magnetic field, high pressure, low temperature, etc). In such cases, feeble magnetic effects accompanied by secondary processes of photoexcitation will be observed with high accuracy. This is suitable for recording natural circular dichroism and also linear dichroism as well. Consequently, this technique should open up new fields in the study of XMCD.

Hiroshi Maruyama
Okayama University

E-mail: maruyama@mag.okayama-u.ac.jp

References

[1] M. Suzuki *et al., Jpn. J. Appl. Phys.* **37** (1998) L1488.

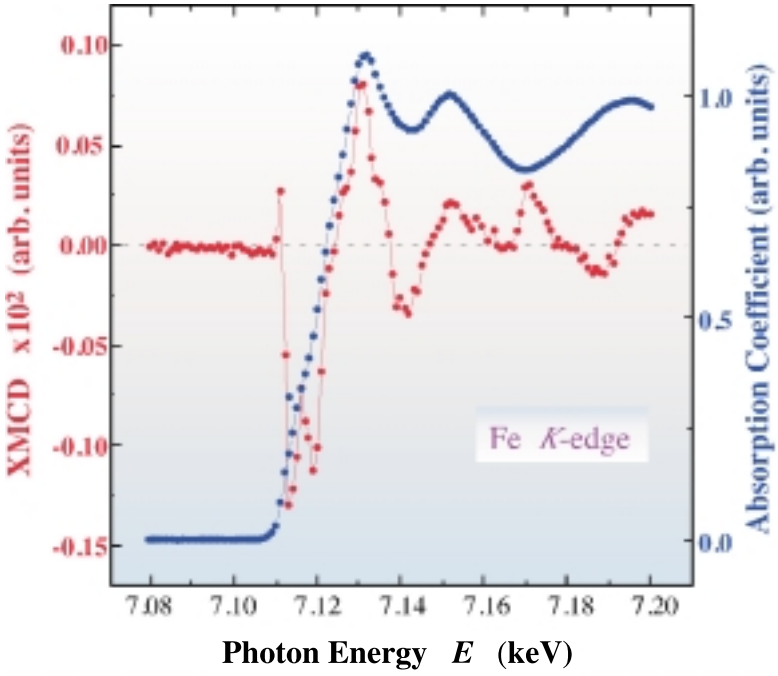

Fig. 3: XMCD spectrum at the Fe K edge in Fe_4N recorded by the helicity-modulation technique. The normalized XANES spectrum is also displayed.

MAGNETIC HYSTERESIS MEASUREMENTS OF XMCD IN Gd/Fe MULTILAYER

X-ray magnetic circular dichroism (XMCD) is one of the most useful types of measurement to investigate magnetic properties using synchrotron radiation X-rays. XMCD is measured at the X-ray absorption edge of a specified element in a sample, which enables element-selective measurement. The intensity of XMCD is proportional to the mean magnetic moment projected onto the direction of the incident X-ray, and the sign reflects the direction of the probed moment relative to that of the total magnetization.

In this study, the above features and a polarization-modulation technique which has been newly developed in SPring-8 have been brought together, and magnetic hysteresis loops of XMCD have been measured at the Gd L_3- and the Fe K-edges in Gd/Fe multilayers. The sample was prepared by alternately depositing Gd (20 Å) and Fe (20 Å) on a polyimide film using an rf magnetron sputtering system. The measurements were made at the beamline **BL39XU** with an X-ray phase retarder to modulate the circular polarization of the incident beam in the hard X-ray region, instead of a usual field-reversal method [1].

Figures 1 and 2 show magnetic hysteresis loops of XMCD at the Gd L_3- and the Fe K-edges, respectively. A magnetization curve is also plotted for comparison in Figure 1. The sign of XMCD at Gd is opposite to that at Fe. This result means that coupling between Gd and Fe moments is fundamentally antiferromagnetic, and also that the Gd moments are parallel and the Fe moments are antiparallel to the field direction at 20 K. The intensities of XMCD gradually decrease with increasing magnetic fields higher than 0.5 kOe, whereas the magnetization monotonously increases.

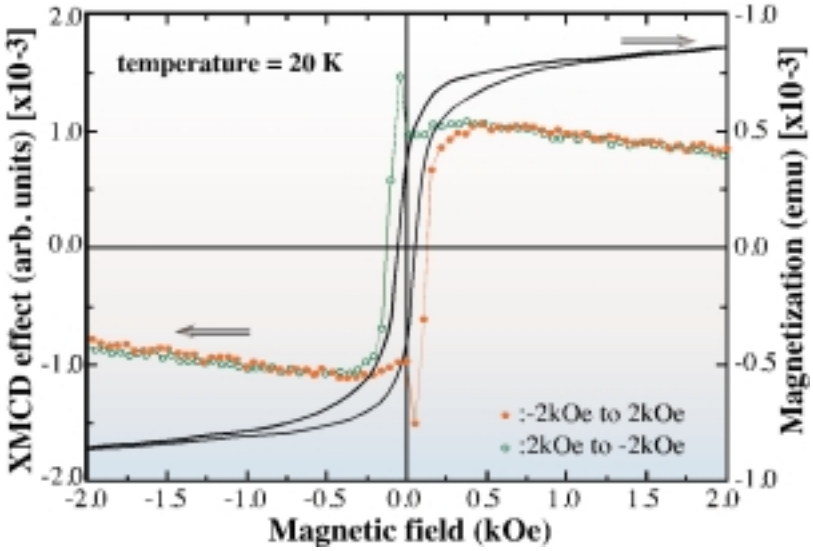

Fig. 1: Magnetic hysteresis loop of XMCD (○ and ● dots) measured at the Gd L_3-edge in a Gd(20Å)/Fe(20Å) multilayer, compared with its magnetization curve (solid line).

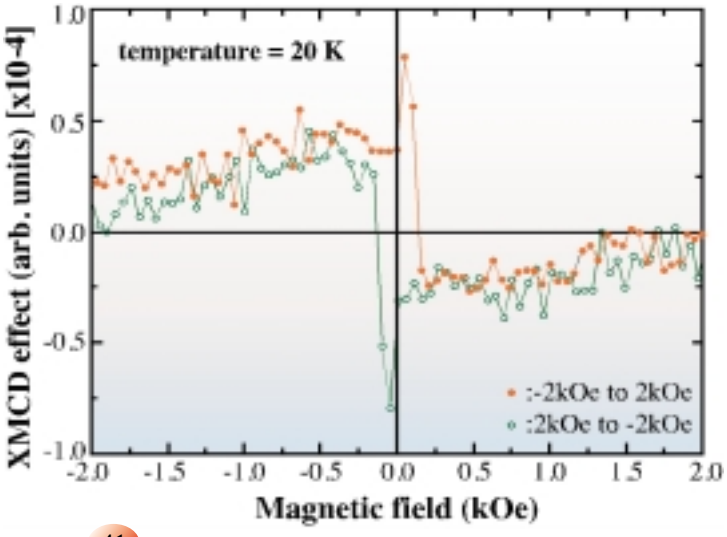

Fig. 2: Magnetic hysteresis loop of XMCD measured at the Fe K-edge in a Gd(20Å) / Fe(20Å) multilayer.

The difference in slope between the XMCD curves indicates that the Gd and Fe moments gradually tilt from the field direction at different rates. A quantitative evaluation suggested that the Fe moments tilt about three times as fast as the Gd moments as the magnetic field increases. Hence, the compensation between such Gd and Fe moments results in an increase in the bulk magnetization. This behavior is consistent with theoretical prediction, what we call the bulk-twisted state, that the effective exchange coupling between the spins in different layers and the Zeeman energy of the spins in an external field compete with each other [2].

The most important finding is a characteristic sharp peak appearing at a coercive field H_c = ±50 Oe soon after the magnetic field is reversed. No indication associated with the peak is observed in the magnetization curve. A possible spin state corresponding to this peak is an Fe-aligned state, where Fe moments are dominant and parallel and where Gd moments are antiparallel to the field direction. Since the Zeeman energies of the Gd and the Fe moments are completely canceled out at H_c, the antiferromagnetic exchange coupling at the interfaces between the Gd and Fe layers plays an important role in determining the magnetic structure, although the effect of the magnetic anisotropy cannot be disregarded.

In conclusion, magnetic hysteresis measurements of XMCD have precisely revealed the magnetization process of each element in Gd/Fe multilayers, which is impossible by magnetization measurements. These results show the indispensable availability of XMCD measurements with the polarization modulation technique, for the study of magnetism in complicated materials.

Akihisa Koizumi, Masafumi Takagaki and Nobuhiko Sakai
Himeji Institute of Technology

E-mail: akihisa@sci.himeji-tech.ac.jp

References

[1] M. Suzuki et al., to be published in *Jpn. J. Appl. Phys.*
[2] J. G. LePage and R. E. Camly, *Phys. Rev. Lett.* **65** (1990) 1152.

XMCD SPECTRUM AT PT $L_{2,3}$ EDGES RECORDED BY HELICITY MODULATION TECHNIQUE

X-ray magnetic circular dichroism (XMCD) at the Pt $L_{2,3}$ edge is a powerful tool for studying the magnetic properties of Pt 5*d* bands and sensitively reflects the TM 3d states in ferromagnetic TM-Pt_3 intermetallics (TM: transition-metal). We previously found that the Pt 5*d* magnetic states in MnPt3 have a quenched orbital component and are dominated by the spin character, whereas a main contribution in $CrPt_3$ is carried by the orbital moment rather than the spin component and the Pt moments couple antiferromagnetically with Cr moments [1].

To study this contrasting magnetic property, the Pt *L* edge XMCD in $(Cr_{1-X}Mn_X)Pt_3$ mixed crystal system is informative for a better understanding of the 3*d* magnetic states. In particular, we are interested in the crossover from orbital to spin character at an intermediate region, where the Pt magnetic moments will be quenched. The helicity-modulation technique [2] recently developed has been applied for measuring weak XMCD signals with a high accuracy. A synthetic diamond (111) crystal slab 0.73 mm thick is operated around the 220 reflection in the Laue geometry. The photon helicity is switched fast between plus and minus offset angles around the Bragg condition, which was previously determined from polarization measurements of the transmitted beam, as shown in Figure 1. In the energy range of the Pt $L_{2,3}$ edges, the photon helicity is alternately turned at 200 Hz by flipping between the offset angles of ±20 arcseconds.

Figures 2 and 3 show Pt L_3 and L_2 edge XMCD spectra, aligned at the absorption edge energy, in a $(Cr_{1-X}Mn_X)Pt_3$ mixed crystal system. When the Mn content is increased, the L_3 edge XMCD is systematically changed from positive to negative, and a dispersion type profile is observed in the intermediate range. This trend is interpreted as an increase in the volume fraction of ferromagnetic $MnPt_3$ in ferrimagnetic $CrPt_3$.

On the other hand, the L_2 edge XMCD always keeps a positive sign and shows a small amplitude at $(Cr_{0.5}Mn_{0.5})Pt_3$, which indicates the collapse of the Pt 5*d* magnetic moments. The L_3 (L_2) spectrum

with a negative (positive) sign means that the Pt 5*d* moments ferromagnetically couple with the 3*d* moments of the TM partner, whereas the positive L_3 edge XMCD on the Cr-rich side shows that the Pt moments dominantly arise from the orbital character, and that such a situation is maintained even by the substitution of Mn for Cr atoms. These spectra can be basically reproduced by the Lorentzian line-shape.

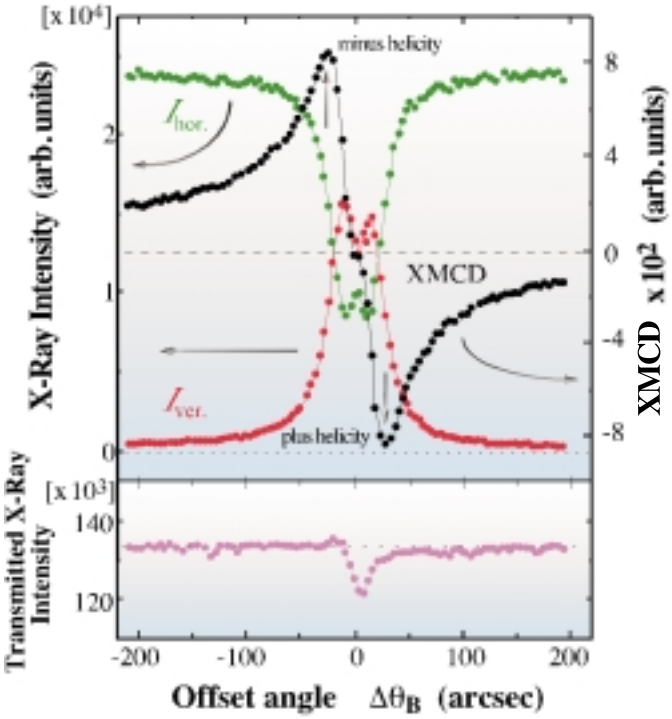

Fig.1: Measured variations of X-ray intensities versus the offset with respect to the Bragg angle in the energy range of 11 keV. The polarization state of the transmitted X-ray is converted into circular polarization at ±20 arcseconds. The XMCD amplitude was also monitored as a function of the offset angle at the Pt L_3 edge in 61.5at% Pt-Fe alloy. The XMCD sign is negative at the L_3 edge in ferromagnet, so that the minus helicity is obtained at the minus offset angle.

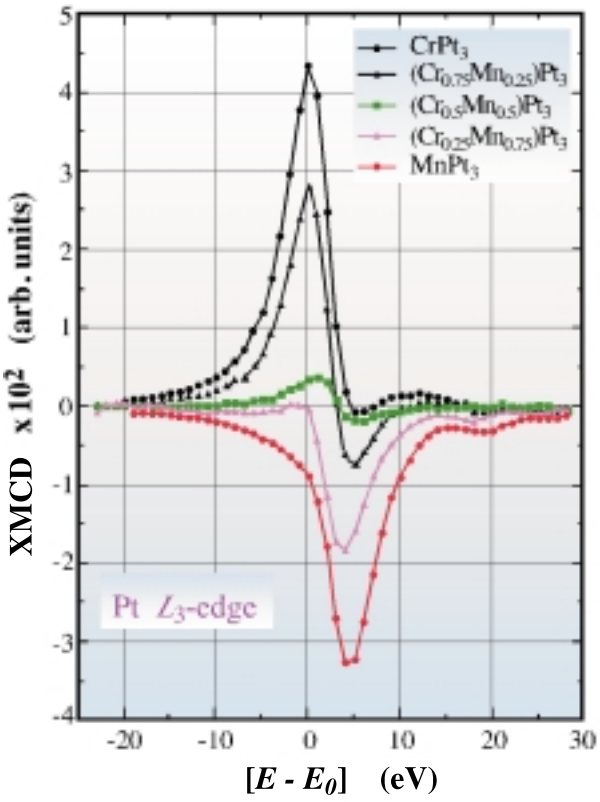

Fig.2: XMCD spectrum at the Pt L_3 edge.

To estimate the Pt magnetic properties using the sum rules [3], the standard procedure is applied for evaluating the intensity of the XMCD and XANES white-line [1], and the ground-state expectation values of orbital and spin moments are empirically obtained.

Figure 4 shows the dependence of Pt magnetic moments on the Mn content. We can see that the orbital moment in $MnPt_3$ is almost quenched,

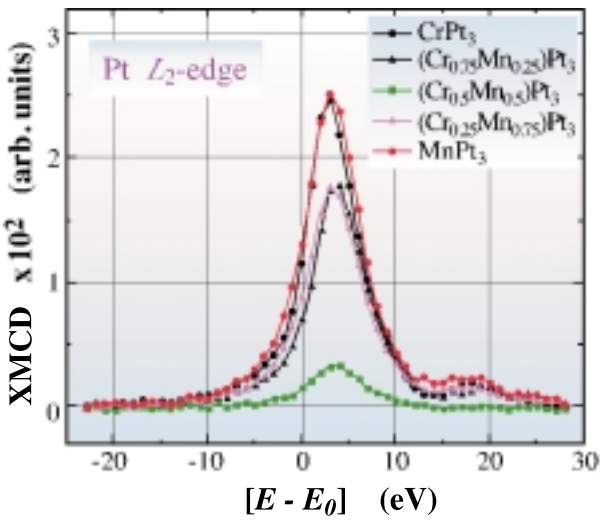

Fig.3: XMCD spectrum at the Pt L_2 edge.

whereas a relatively large orbital component remains in $CrPt_3$. The spin component always shows a positive moment in spite of the small amplitude on the Cr-rich side, as a result, the total moment increases linearly with the Mn content. In $(Cr_{0.5}Mn_{0.5})Pt_3$, the total moment is, however, almost cancelled out due to the opposite contribution between the orbital and spin characters, so that this sample has a relatively low Curie temperature.

The Pt *L* edge XMCD provides the evidence that the Pt 5*d* magnetic states sensitively depend on the neighboring TM atom and local environment. The magnetic properties of the $(Cr_{1-X}Mn_X)Pt_3$ system can be explained by taking the average over the volume fractions of ferromagnetic $MnPt_3$ and ferrimagnetic

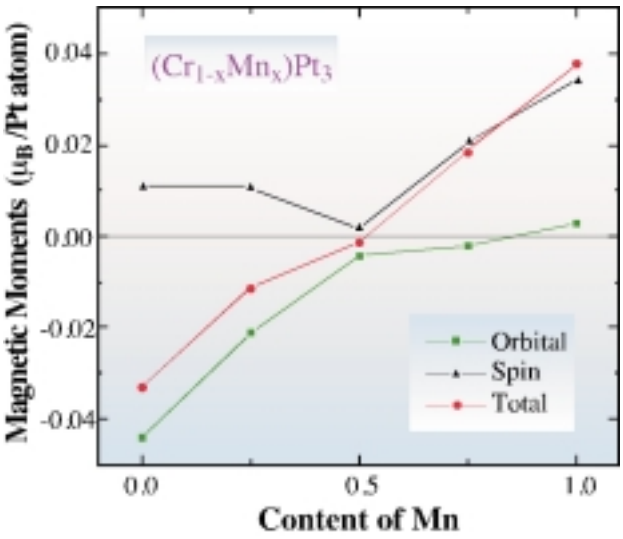

Fig.4: Orbital, spin and total magnetic moments of Pt atom estimated from the sum rules. These data are subjected to no correction for the saturation magnetization.

Hiroshi Maruyama
Okayama University

E-mail: maruyama@mag.okayama-u.ac.jp

References

[1] H. Maruyama *et al., J. Magn. Magn. Mater.* **43** (1995) 140.
[2] M. Suzuki *et al., Jpn. J. Appl. Phys.* **37** (1998) L1488.
[3] P. Carra *et al., Phys. Rev. Lett.* **70** (1993) 694.

HIGH RESOLUTION Ce 3*d*-4*f* RESONANT PHOTOEMISSION STUDY OF CeNiSn and CePdSn

Many Ce compounds have attracted interest widely due to their strongly correlated Ce 4*f* states hybridized with valence band states. High resolution photoemission spectroscopy is a useful technique to experimentally reveal the electronic states. It is known, however, that rare-earth 4*f* electronic states on the surface are remarkably different from those in bulk. Measurements at low $h\nu$ (< 200 eV) cannot faithfully probe the bulk Ce 4*f* states due to their surface-sensitivity.

In order to study such bulk electronic states using high energy excitations ($h\nu$ > 500 eV), a high resolution photoemission station has been constructed at the twin-helical undulator beamline **BL25SU** [1]. Here, we report high resolution Ce 3*d* resonant photoemission spectra of CeNiSn and CePdSn measured at this station.

CeNiSn is a so-called "Kondo semiconductor" where the Kondo temperature (T_K) is of the order of ~40 K and the Ce 4*f* electrons are valence-fluctuating [2]. For CePdSn, on the other hand, the Ce 4*f* electrons are more localized and T_K is thought to be lower than 7 K [3]. A Ce 3*d* resonant photoemission study was performed with the total energy resolution of ~0.22 eV, as shown in Figure 1**(b)**. The sample temperature was about 20 K.

Figure 1**(a)** shows Ce 3*d* resonant valence band spectra of CeNiSn and CePdSn together with the Ce 4d resonance spectra. The Ce 4*f* contributions are obtained by subtracting the Ce 3*d* off resonance ($h\nu \leq$ 875 eV) spectra from the on resonance ($h\nu$ ~882 eV) ones ("3*d*-4*f* spectra"). In the 3*d*-4*f* spectra of CeNiSn, one can see a strong peak due to the f^1 final states near E_F and the shoulder structure of the f^0 final states at ~2.4 eV. For CePdSn, the f^0 peak at about 1.9 eV and the f^1 peak near E_F, which is comparable to slightly stronger than the f^0 peak, are observed.

The Ce 4*f* contributions obtained by the same procedure in the Ce 4*d* resonance region ($h\nu$ ~120 eV, "4*d*-4*f* spectra") are also displayed. They were measured at beamline BL-3B of the Photon Factory. One can notice that the 4*d*-4*f* spectral shapes are

remarkably different from those of the 3*d*-4*f* ones. These striking differences are thought to originate from the differences of the *c*-*f* mixings in the bulk and surface, where c stands for the valence bands.

Details of the resonant spectra near E_F are shown in Figure 1**(b)**. In the Ce 3*d* on resonance spectrum CeNiSn, the binding energy of the maximum intensity is located at <0.2 eV. A further remarkable finding is that the mid-point of the leading edge in the Ce 3*d* and 4*d* resonance spectra is unambiguously located above E_F, suggesting the existence of a narrow and strong Kondo peak above E_F.

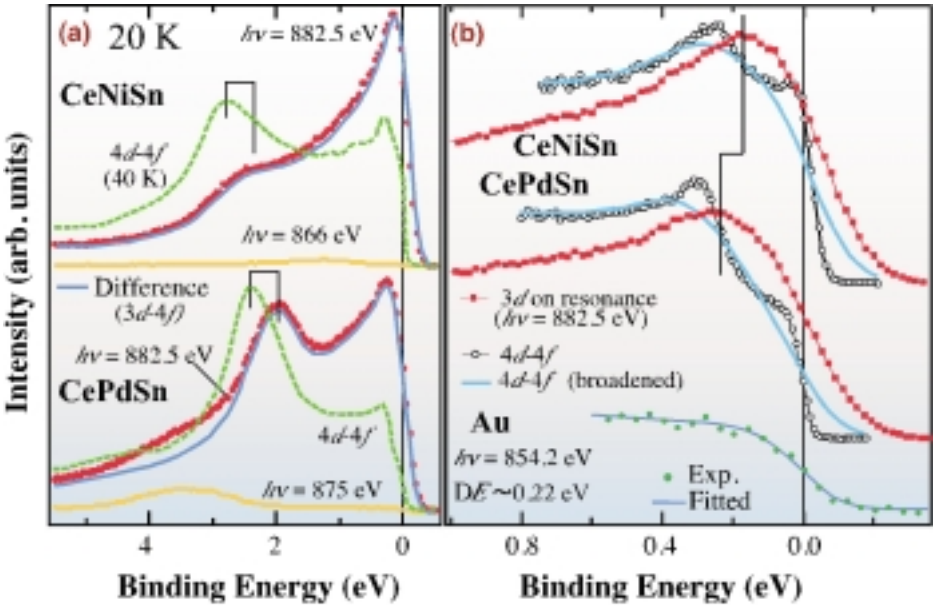

Fig. 1: ***(a)*** *High resolution Ce 3d resonant photoemission spectra: (on: hν ~ 882 eV, off: hν ≤ 875 eV) of CeNiSn and CePdSn compared with the Ce 4f contributions obtained from the Ce 4d resonant photoemission.*
(b) *Spectra near E_F.*

In the Ce 3*d* and 4*d* resonance spectra of CePdSn, on the other hand, the point at half-intensity of the edge is located fairly close to E_F. The point of the maximum intensity in the Ce 3*d* on resonance spectrum of CePdSn is positioned at ~0.25 eV, which is deeper than that for CeNiSn. This is considered to be reflected in the differences of the *c*-*f* mixings, and therefore, that of T_K between weakly hybridized CePdSn and more strongly hybridized CeNiSn. We also show the 4*d*-4*f* spectra near E_F, broadened by the resolution of the Ce 3*d* resonant spectra in Figure 1**(b)**. The broadened 4*d*-4*f* spectra do not coincide with the Ce 3*d* on resonance spectra for both materials, indicating that the different line shapes cannot be explained by the resolution effect only.

In order to understand the bulk Ce 4*f* contributions, we have performed spectral calculations using a non-crossing approximation (NCA) based on the single impurity Anderson model (SIAM) [4]. The properly fitted results of the calculations are compared with the bulk-sensitive 3*d*-4*f* spectra in Figure 2, in which the NCA-calculated spectra semi-quantitatively reproduce the experimental ones for both compounds. The estimated T_K's from the calculations are comparable to those mentioned above. For reference, we also show a properly broadened Ce 4*f* partial density of states (PDOS) obtained by a band-structure calculation for CeNiSn [5] in Figures 2 **(a)**.

According to an improvement of the beamline monochromator, the third resonant photoemission study is nowadays done at a total resolution of 100 meV.

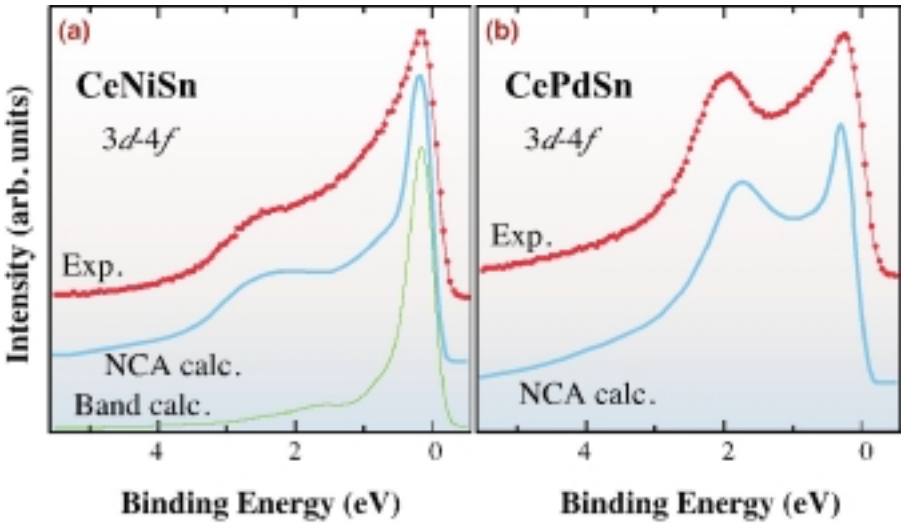

Fig. 2: Comparison of the 3d-4f spectra with theoretical calculations for ***(a)*** *CeNiSn and* ***(b)*** *CePdSn. For the experimental 3d-4f spectra, the secondary electron backgrounds of the integration type were properly subtracted from those in Fig. 1* ***(a)****.*

Akira Sekiyama[a], Shigemas[a] Sugaa and Yuji Saitoh[b]

(a) Osaka University

(b) SPring-8 / JAERI

E-mail: sekiyama@mp.es.osaka-u.ac.jp

References

[1] Y. Saitoh *et al., J. Synchrotron Rad.* **5** (1998) 542.

[2] T. Takabatake *et al., Phys. Rev. B* **41** (1990) 9607; *Phys. Rev.* **45** (1992) 5740.

[3] D. T. Adroja *et al., Solid State Commun.* **66** (1988) 1201.

[4] O. Gunnarsson and K. Schönhammer, *Phys. Rev. B* **28** (1983) 4315.

[5] A. Yanase and H. Harima, *Prog. Theor. Phys. Suppl.* **108** (1992) 19.

INSTRUMENTATION & TECHNIQUES

Since commissioning of beamlines in April 1997, intensive projects have been pursued in development of X-ray optics, monochromators, microbeams, imaging techniques, detectors and other advanced system. At present, SPring-8 provides the most intense X-ray beam in the hard X-ray regions that has never been achieved, but the improvement of instruments is still essential. Because we do not have enough space to describe every aspect of this research field, we will introduce here some typical examples of eminent works.

The key advantage of SPring-8 is its high brilliance and low emittance of X-ray beam, vertical emittance of electron beam (several tens of p m·rad) approaching to intrinsic emittance of hard X-ray photons. However, handling the spatially coherent X-ray beam involves the serious obstacles to beam position monitoring (BPM). In order to use a coherent X-ray beam, it is necessary to measure the beam position non-destructively with micrometer accuracy. A diamond photo-conductive detector is one of the candidates for transparent BPM. The recent results for this device are presented in this section.

X-ray focusing and collimating optics for hard X-rays are also pioneering work. Mirror optics is usually used in soft and hard X-ray regions below 20 keV. For higher energy, refractive optics is one of the candidates. "Bubble lens" is a unique optical device developed at SPring-8. Two-dimensional focus around 19 keV X-rays has been tested. These focusing optics may be very useful for the experiment where the preparation of a large sample is difficult.

Refractive optics is also applied to collimate divergent X-ray beam. Here, the array of parallel holes is used as a cylindrical lens. Undulator radiation from the SPring-8 storage ring is not perfectly parallel. By using the newly developed refractive collimator, the angular divergence is reduced to one-third. This collimator will be a powerful tool for speckle, interference, high energy resolution and high angular resolution experiments.

X-ray fluorescence holography has recently been developed to obtain direct three-dimensional atomic images. However, because of the lack of photon flux, only the holograms of single crystals with the known structure have been demonstrated. By using a high-intensity primary X-ray beam, the atomic structure around doped zinc atoms (200 ppm) in gallium arsenide has been revealed. The X-ray fluorescence holography is the only method for the direct measurement of a three-dimensional structure that has no long-range ordering. Application to structural analysis of biomolecules may be possible in the future.

Yoshio Suzuki

PERFORMANCE TEST OF DIAMOND DETECTOR FOR X-RAY BEAM POSITION MONITOR

Diamond is promising as a base material for the detector head of X-ray beam position monitors (XBPM) because of its high thermal conductivity, high electric resistivity and low absorption coefficient for X-rays. We have been developing an area-type XBPM that is operating in photo-conduction mode [1]. In this monitor, a bias voltage is applied to produce an electric field inside the diamond plate. When photons are absorbed inside, electron-hole pairs are created. These carriers drift along the electric field and generate a current in the circuit. The number of carriers is proportional to the energy of the absorbed photon, and thus the amount of signal current is proportional to the absorbed beam power. On the other hand, hard X-rays are nearly transparent. Therefore, the detection efficiency is expected to be greater at the energy of several keV. Moreover, the peak energy is expected to be higher by up to a few tens of keV, with the effective thickness of the plate. This property is suitable for detecting photon beams from undulators because this detector is less sensitive to low energy photons, which are dominant in background from the fringing field of bending magnets.

We designed and fabricated a test sample of the detector head for test measurements at the beamline **BL01B1**. Figure 1 shows the metalization pattern on the diamond plate. The dimensions of this CVD diamond sample is 20 mm X 40 mm X 0.24 mm. A pair of aluminum electrodes was formed by an evaporation technique on both sides of the plate. One electrode is for reading signals and the other is for applying bias voltage. The top part of the sample is for heat contact. This sample was set on a translation stage in two ways. One was to set it in parallel with the beam to evaluate the performance as a blade photo-conduction type. There are five spots of various effective thicknesses: 0.5, 1, 2, 4 and 8 mm. The other was to set it perpendicular to the monochromatic beam to evaluate the performance as an area photo-conduction type. The typical pressure of this chamber was about 10^{-5} Pa.

The response time observed upon opening and closing the shutter was relatively slow because of the low quality of the base material. Since high electric resistivity is desirable for use in photo-conduction mode, it is important to obtain a high-grade CVD diamond at a reasonable price.

The dependence of signal current on bias voltage and thickness was observed (Figure 2). The sample was set in parallel with a monochromatic beam of 20 keV. The signal current is proportional to bias voltage at each effective thickness. The current signal increased with the effective thickness along the beam path. Therefore, the blade photo-conduction type is a promising candidate for future XBPMs. The dependence of the detection efficiency on photon energy was also observed with the

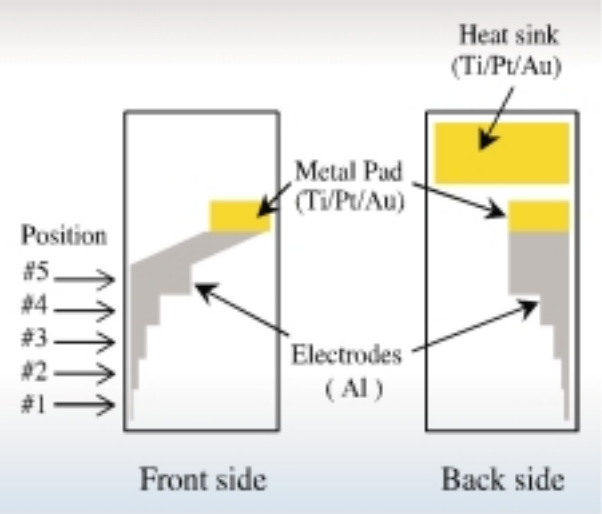

Fig. 1: Metalization pattern on diamond plate.

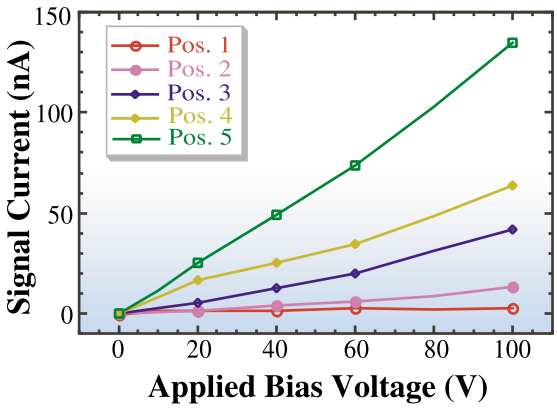

Fig.2: Bias voltage and thickness dependence of signal current.

range of the photon energy was from 4.5 keV to 70 keV. A preliminary analysis showed that the detection efficiency decreased in the photon energy range from 4.5 keV to 30 keV and increased over 30 keV. The latter increase seems to be due to Compton scattering. We are planning to measure the efficiency in the range below 4.5 keV to clarify the peak structure at the energy of several keV.

Hideki Aoyagi
SPring-8 / JASRI

E-mail: aoyagi@spring8.or.jp

References

[1] H. Sakae *et al., J. Synchrotron Rad.* **4** (1997) 204.

EVALUATION OF X-RAY REFRACTIVE LENS MADE OF LIQUID MATERIAL

In spite of the extremely small X-ray refractive index decrement, an X-ray refractive lens was first achieved in an array of pinholes on an aluminum alloy plate (compound refractive lens, [1]). A two-dimensional lens was also developed by crossing two linear arrays in perpendicular directions [2]. This was also discussed in a case of parabolic lenses [3]. When liquids and gases are used as the lens material, the surface tension seems to form spherical and parabolic shapes much more naturally. Lenses were manufactured in the following way. First, the so-called "bubble lens" was manufactured by forming bubbles in a liquid adhesive (Figure 1). A mixture containing glycerol was used as the liquid and an acrylic container was designed so that 168 bubbles with diameter of about 2.8 mm each could be aligned in a straight line in the liquid. Pure helium gas from a gas cylinder was injected into the liquid through a needle valve and a syringe needle with an outer diameter of 0.5 mm

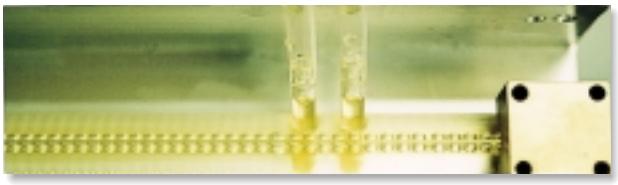

Fig. 1: Liquid container for X-ray "bubble lens" made from acrylic resin and Kapton films. Two pipes worked as inlet and outlet of the bubbles and a triangular ceiling kept the bubbles in a straight line. Courtesy of SPIE [4].

We further evaluated the so-called "micro-capillary lens". This lens was made by the Belarusian State University [5,6,7]. Bubbles were formed in a glue in thin glass capillaries and then solidified to obtain a solid X-ray refractive lens. The surface tension of the glue gives the surface of the bubbles an approximately spherical shape. So far, lenses with small apertures of around 0.2 mm in diameter have been developed (Figure 2). A similar lens with a diameter of 0.8 mm was also made with glycerol [7].

Fig. 2: Image of a micro-capillary lens taken with an optical microscope. The inner diameter of the glass capillary is 0.8 mm.

These two types of lenses were probably the first two-dimensional X-ray refractive lens systems using spherical lenses [4, 5].

An evaluation of the lenses was made at the beamline **BL47XU**. The demagnified image of the undulator source was taken, and the image size and gain at the focal plane were measured. The experimental conditions (ID gap and X-ray energy) were **(a)** 27 mm, 19 keV for the "bubble lens" and **(b)** 26 mm, 18.3 keV for the "micro-capillary lens". The observed focal lengths were **(a)** 5.4 m and **(b)** 0.8 m.

The distance between the source and the lenses was about 45 m. The coupling constant of SPring-8 was as small as 0.2%, and the vertical undulator source size was extremely small, i.e., less than 30 micrometer (FWHM) [8].

The vertical sizes and gains of the demagnified source image were measured at the focus of these lenses. Here, gain means the increase of flux from the condition of a tiny pinhole. The transmissivities of these lenses were measured with an air-filled ionization chamber as the ratio of the currents with and without the lenses as summarized in **Table I**.

The measured vertical sizes at the focus of these two lenses were larger than the geometrically expected size. For both "bubble" and "micro-capillary" lenses, however, a relatively high gain of 12 was obtained.

The "bubble lens" together with the "micro-capillary lens" have the advantage of high transmissivity and high gain. The solidified "bubbles lens" was also extremely stable to high flux of $4X10^{12}$ photons/sec/0.03 mm^2 at 18 keV (gap = 10 mm, 1 hour exposure). To improve gain, much more precise formation of the bubbles would be required.

The surface tension of the bubbles should be larger to keep them in perfect spherical shape. This may be done by using liquids with larger surface tensions or by pressurizing the bubbles. Moreover, it would be interesting to vary the focal length of the "bubble lens" by changing the pressure inside the liquid container.

The "micro-capillary lens" is most promising in terms of the focus size, but development of lenses with a larger aperture and parabolic surfaces is needed.

Table I. *Results of two-dimensional focusing test using "bubble lens" and "micro-capillary lens".*

	X-ray Energy (keV)	Vertical Image Size (μm, FWHM)	Transmissivity (%)	Gain
Bubble Lens	19	~60	16	12
Micro-capillary Lens	183	8	18	12

Yoshiki Kohmura
SPring-8 / RIKEN

E-mail: kohmura@spring8.or.jp

References

[1] A. Snigirev *et al., Nature* **384** (1996) 49.
[2] P. Elleaume, *Nucl. Instrum. and Meth. in Phys. Res. A* **412** (1998) 483.
[3] B. Lengeler *et al., J. Appl. Phys.* **84** (1998) 5855.
[4] Y. Kohmura *et al., SPIE Proc.* **3449** (1998) 185.
[5] Yu.I. Dudchik and N.N. Kolchvsky, *Nucl. Instrum. and Meth. in Phys. Res. A* **421** (1999) 361.
[6] Yu.I. Dudchik *et al.*, submitted to *Rev. Sci. Instrum.*
[7] Y. Kohmura *et al.*, submitted to *Rev. Sci. Instrum.*
[8] S. Dat *et al., PAC Proc.*, New York, 1999.

Y. Kohmura, M. Awaji, Y. Suzuki, T. Ishikawa, Y.I. Dudchik, N.N. Kolchevsky, F.F. Komarov, submitted

A REFRACTIVE COLLIMATOR FOR SYNCHROTRON RADIATION

A lens will collimate the radiation from a point source placed in its focus. Thus the development of compound refractive lenses for focusing X-rays [1] has the corollary that such lenses can be used for *collimation*. While the present third generation synchrotron radiation facilities provide beams from insertion devices that are relatively well-collimated, the high brilliance of these sources means that many high resolution experiments are now being done that would benefit from an even more collimated X-ray beam. In this context, one considers high-energy resolution for, *e.g.*, inelastic or nuclear scattering measurements, as well as high-angular resolution (or, in fact, nearly any measurement making use of Bragg reflections in perfect crystals - including polarization control and analysis). Here we show that a refractive lens may be used to collimate the radiation from an undulator to <3 μrad full width at half maximum (FWHM), with only a small (~10%) loss in intensity [2].

The essential concept of our collimator is shown in Figure 1. A piece of material with holes drilled normal to the beam propagation direction acts as an X-ray lens [1]. Collimation is achieved by choosing the number of holes so that the distance to the source point is the focal length of the lens. In selecting the material, it is important to avoid photoelectric absorption. Therefore, for low- to medium-energy X-rays (approximately 10 to 40 keV), one should choose materials with a low atomic number (at higher energies, Compton scattering must be considered). After extremely promising results using plastic lenses [3], we had some lenses fabricated out of beryllium. While a variety of practical concerns (lens acceptance, transmission, aberrations, etc.) are relevant to lens fabrication, here we do not go into detail but refer the reader to longer papers (*e.g.* [4]). We do note, however, that the long focal length for collimation makes these lenses relatively efficient, as it has large apertures without too much absorption.

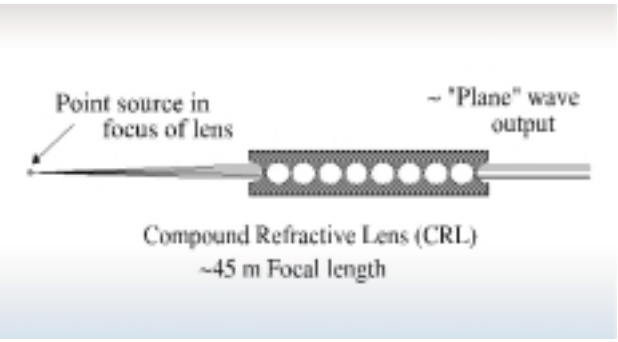

Fig.1: Principle behind refractive collimator. Matching the focal length to the distance to the point source leads to collimation of transmitted radiation.

We tested the collimator at the beamline **BL47XU** [5]. 18.5 keV X-rays were selected from the third harmonic of an in-vacuum undulator using a cryogenically-cooled Si monochromator [6]. In order to measure the divergence of the incident beam and the effect of the collimator on that divergence, we used a pair of Si (555) reflections in a dispersive (+,+) setting. In this geometry, assuming the bandwidth of the incident beam is sufficiently large, scanning the second crystal provides a map of the divergence incident on the first crystal with a 2:1 resolution: if the width of the rocking curve of the second crystal is $\Delta\theta$, the divergence of the beam incident on the pair is $\Delta\theta/2$.

The effect of the beryllium refractive collimator (ϕ 2.2 mm holes, 13 interfaces of 100 microns each) is shown in Figure 2. It reduced the beam divergence from 11.5 to <3 μrad (FWHM) an improvement of about a factor of four, while preserving 89% of the incident flux. Similar results were obtained using a lens of seven interfaces at 14.4 keV, with the beam collimation improving from 14 to < 3 μrad (FWHM) and transmission of about 92%.

We have shown that a refractive collimator is an efficient method for collimating an undulator beam, leading to a significantly reduced divergence without a large sacrifice in intensity. Compared with crystal optics, our method has the very important advantage that it does not lead to an increased beam size. In addition, the bandwidth of the collimator (>~1%) is much larger than an asymmetric reflection, and this collimator neither displaces nor modifies the direction of transport of the X-ray beam. Also, the strong chromatic

aberration of asymmetric crystals (leading to an energy-angle correlation in the output beam) does not appear.

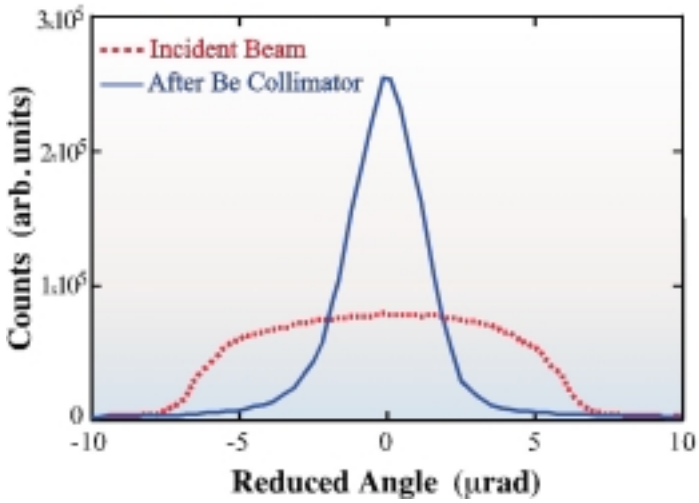

Fig.2: Effect of beryllium collimator at 18.5 keV. Dashed line shows beam divergence without the collimator. Solid line shows divergence measured after the collimator. X-ray divergence is reduced from 11.5 to < 3.0 μrad (FWHM) while 89% of incident intensity is transmitted. Note that "reduced" angle for x-axis corresponds to measured divergence of X-ray beam (see text).

Alfred Q.R. Baron
SPring-8 / JASRI

E-mail: baron@spring8.or.jp

References

[1] A. Snigirev *et al., Nature* **384** (1996) 49 .
[2] A.Q.R. Baron *et al.*, to be published in *J. Synchrotron Rad.*.
[3] A.Q.R. Baron *et al., Appl. Phys. Lett.* **74** (1999) 1492.
[4] P. Ellaume, *Nucl. Instrumen. and Meth. A* **412** (1998) 483.
[5] Y. Kohmura *et al., SPring-8 Information* (in Japanese) Vol. **3**, No. 4 (1998) 28.
[6] T. Mochizuki *et al.*, work in progress.

ATOMIC IMAGING AROUND Zn IN GaAs:Zn USING MULTIPLE -ENERGY X-RAY HOLOGRAPHY

The X-ray fluorescence holography makes it possible to obtain direct three-dimensional atomic images around atoms emitting fluorescent X-rays [1]. However, only the holograms of single crystals, whose atomic configurations are already known by the X-ray diffraction method, have been measured because of the weakness of the primary X-rays. Therefore, we applied this method to imaging the atomic structure around zinc (Zn) atoms doped in gallium arsenide (GaAs) with synchrotron radiation [2]. X-ray fluorescence holography has two types of experimental techniques. One is called "X-ray fluorescence holography" (XFH) and the other is called "multiple-energy X-ray holography" [3] (MEXH). MEXH is the result of the optical reciprocity theorem applied to XFH and has the advantage of suppressing the twin image effect. We adopted here the MEXH mode for obtaining the hologram. The incident X-ray energy 9.8 keV was selected, which is between the Zn and Ga K absorption edges, so as to avoid excitation of the Ga and As X-ray fluorescence. The sample was mounted on a two-axis rotatable stage. Figure 1 shows the experimental setup. The Zn Kα X-ray fluorescence intensity was measured as a function of azimuthal (ϕ) and incident (θ) angles by an Si PIN detector, and the resulting holographic pattern was obtained, as shown in Figure 2.

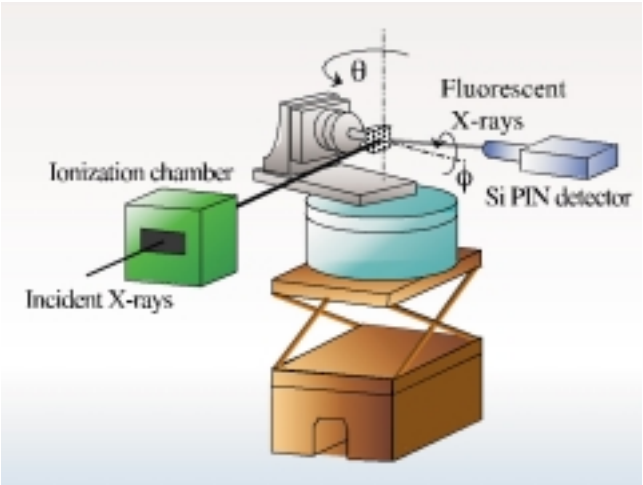

Fig. 1: Experimental setup.

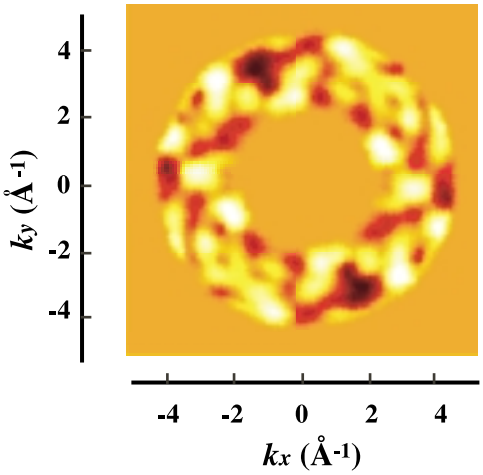

Fig. 2: Measured hologram from Zn doped in GaAs. Courtesy of Jpn. Anal. Chem. [2].

A real space atomic image was calculated by Fourier transformation from the hologram. The reconstruction in Figure 3 **(a)** is the environment around Zn atoms on the (001) plane. Four atoms were found in the image at a distance of 4.0 Å from the center. The Ga and As layers stack alternately along the c-axis; these two layers are separated by 1.41 Å. The atomic configuration of the Ga layer is the same as that of the As layer, and the nearest Ga-Ga and As-As distances are 4.00 Å. It was found from the reconstructed image in Fig. 3 **(a)** that the Zn atoms substitute for Ga or As host atoms. We also observed four blurry atoms at a distance of 2.0 Å from the center Zn atom in Fig. 3 **(a)**. This image is a superposition of two different Ga or As layers above and below the emitter, because the spatial resolution along the z-axis was not good. In order to determine the structure of the layer above the Zn atom, we reconstructed the atomic image of the (004) plane situated at z = 1.41 Å above the emitter, as shown in Figure 3 **(b)**. The atomic image exhibits two enhanced atoms at a distance of 2.0 Å from the center, revealing that the Zn atoms substitute selectivity for one site of Ga or As. The possibility of As-site substitution may be negligible because of the charge neutrality.

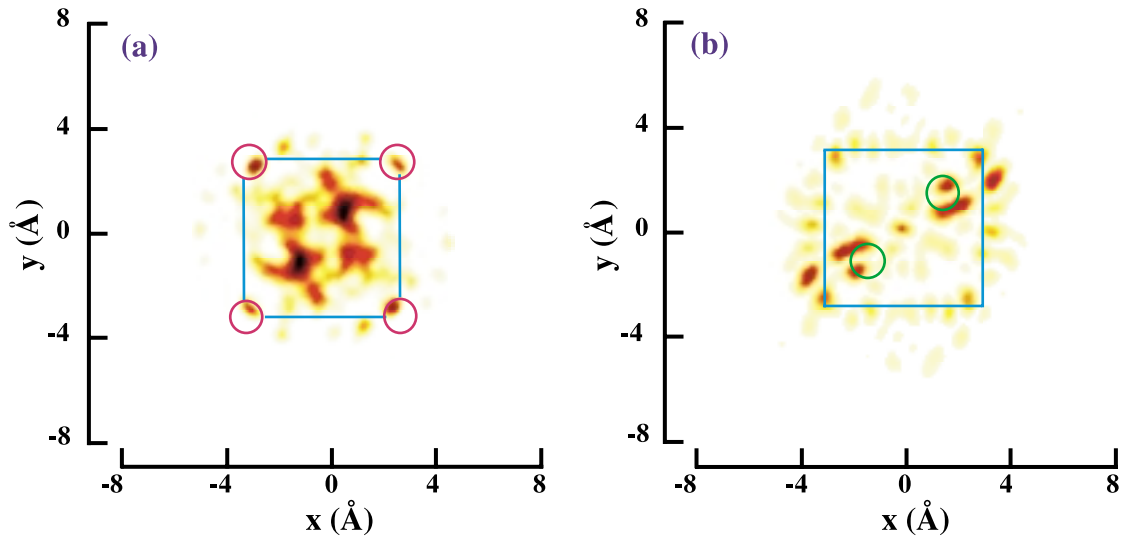

Fig. 3: Reconstructed holographic images around Zn. ***(a)*** *(001) plane, center is the Zn atom.* ***(b)*** *(004) plane, 1.71 Å above the Zn atom. Solid lines show outline of crystal cell. Courtesy of Jpn. Anal. Chem. [2].*

In conclusion, we measured the X-ray fluorescence hologram of 0.02 wt% (200 ppm) Zn in a GaAs wafer and successfully obtained local atomic images around Zn. These images revealed that Zn atoms occupy the substitutional site. The results demonstrate that the X-ray holography technique is applicable to practical structural analysis of trace impurities for a reasonable measurement time using the third-generation synchrotron radiation facility.

Kouichi Hayashi[a], Jun Kawai[a] and Shinjiro Hayakawa[b]
(a) Kyoto University
(b) Hiroshima University

E-mail: hayashi@karma.mtl.kyoto-u.ac.jp

References

[1] M. Tegze and G. Feigel, *Nature* **380** (1996) 49.
[2] K. Hayashi *et al., Anal. Sci.* **14** (1998) 987.
[3] T. Gog *et al., Phys. Rev. Lett.* **76** (1996) 3132.

Accelerators & Beamlines Frontiers

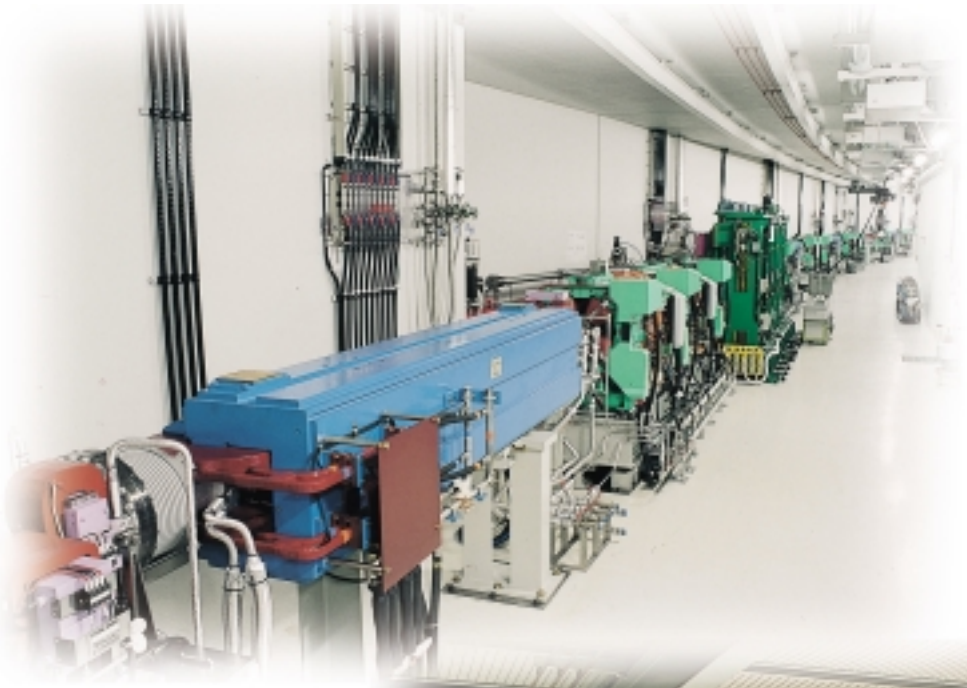

Beam Performance

Since the beam commissioning of the storage ring in March 1997, machine performance has been intensively evaluated, and the beam performance achieved up to now is shown in Table I together with the storage ring specifications. It became clear that the storage ring provided a much higher performance than that we had expected in the design phase.

Table I : *Performance of the SPring-8 Storage Ring*

	Designed	Achieved
Cell type	Chasman-Green	
Number of cells (normal / straight)	44 / 4	
Circumference	1435.948 m	
Energy	8 GeV	
Stored current multi / single	100 mA / 5 mA	100 mA / 12 mA
Tunes (ν_x,ν_y)	51.22 / 16.16	51.16 / 16.31
Chromaticities (ξ_x,ξ_y)	0 / 0	3.21 / 3.93
Emittance	7 nm·rad	6.8±0.5 nm·rad
Coupling ratio	≤ 10%	≤ 0.06%
Bunch length	35 psec	36 - 40 psec
Energy spread ($\Delta E/E$)	0.0011	0.0012
Lifetime 100 mA (full fill) 1 mA (single bunch)	 24 hr	 60 hr 6 hr
Impurity		< 10^{-6}
COD		
horizontal (rms)		≤ 0.1 mm
vertical (rms)		≤ 0.1mm
Residual dispersion at non-dispersive section		
horizontal (rms) vertical (rms)	0 0	1.4 cm 0.4 cm

Beam Lifetime

In the 2/3 filling mode, total beam lifetime is about 70 hours at 70 mA. This lifetime is determined not only by the dynamic vacuum pressure but also by the Touschek effect, even in multi-bunch mode. In the case of 2/3 filling mode (0.043 mA/bunch), gas scattering lifetime and Touschek lifetime are 140 hours and 120 hours, respectively.

In the full filling mode, beam lifetime is about 60 hours at 100 mA, which is significantly longer than that of the partial filling mode at the same intensity. It seems that the electron beam size grows as a result of an instability due to an ion-trapping effect.

In single-bunch mode, lifetime decreases rapidly with the bunch current as shown in Figure 1. Lifetime at 1 mA/bunch is about 6 hours, and that at the design value of 5 mA/bunch is shorter than 2 hours. The dependence of lifetime on bunch current is mainly attributed to the Touschek effect.

Bunch Length

In the SPring-8 storage ring, the bunch length measured by a streak camera increases rapidly with bunch current as shown in Figure 1. At a bunch current of 12 mA, the bunch length becomes 2.5 times longer than that at the low current. This increase in bunch length is consistent with the simulation results for bunch lengthening due to the inductive impedance of vacuum elements.

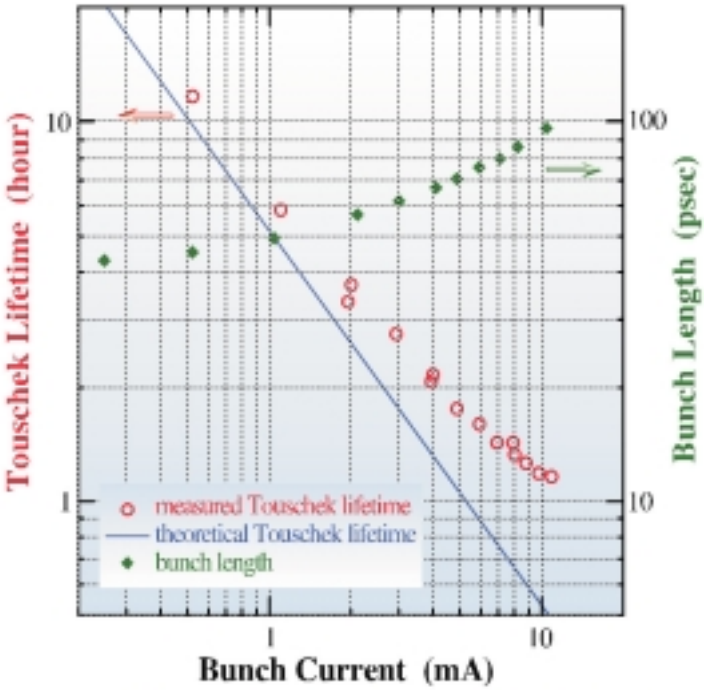

Figure 1: Beam lifetime and bunch lengthening as a function of bunch current.

Emittance

The horizontal emittance was estimated from the horizontal beam size and a beta function at the position of the size measurement. The horizontal beam size was measured from the relation between the electron loss rate and the amplitude of injection bump orbit with a half-sine shape of 8 msec width, assuming a transverse distribution of electron beam as Gauss distribution. The measured horizontal emittance was 6.8–0.5 nm·rad.

The vertical emittance depends on the coupling between the horizontal and vertical betatron oscillations. The coupling ratio of the SPring-8 storage ring is extremely low without the use of skew correction due to good magnet alignment and appropriate COD correction. The coupling ratio was estimated from the following four measurements:

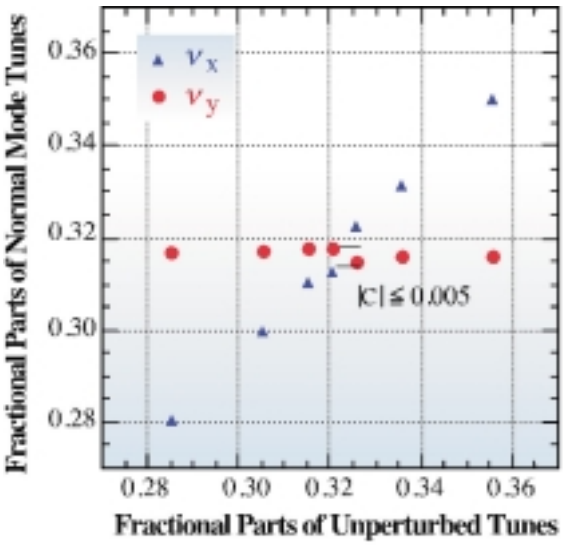

Figure 2: Tune separation for resonance difference; the resonance width (|C|) is about 0.005.

1. Coupling measurement from mode frequencies

The operation point (ν_x,ν_y) of the SPring-8 storage ring is (51.16, 16.32). The betatron coupling is mainly induced by the resonance difference of ν_x-ν_y=35. The width on the resonance difference in single resonance approximation is estimated from the relation (Figure 2) between the unperturbed tunes and the measured ones neighboring the resonance. The coupling ratio, calculated by using the measured width (of less than 0.005) and the distance from the resonance difference, is about 0.06% at the normal operation point (ν_x=51.16, ν_y=16.32).

2. Coupling Measurement from Coherent Oscillations

The coupling ratio (κ) can also be directly measured from the form of the coupled oscillation following a dipole kick in the horizontal direction. The coupled oscillations (Figure 3) were measured turn-by-turn with beam position monitors (BPM) for five coupling ratios estimated from the measurement of the frequency mode together with the beam lifetime. At the normal operation point corresponding to κ=0.06% (upper most graph), the coupled oscillation in the vertical direction cannot be observed by BPM within a resolution of a few μm. From these data, the coupling ratio was recalculated from the ratio of the minimum to the maximum horizontal oscillation and the beat period of the oscillations. The coupling ratios obtained by these two different measurements were consistent within a few tenths of a percent.

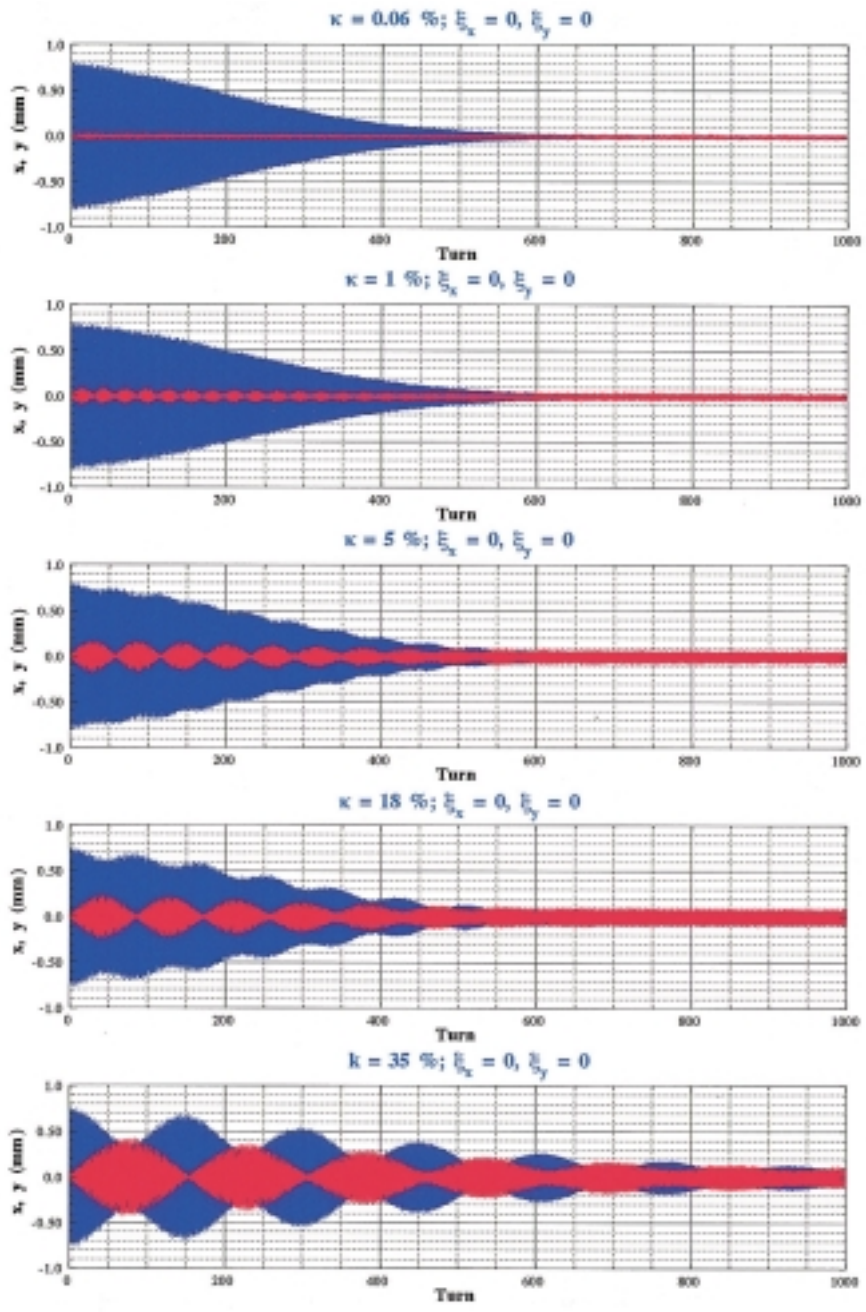

Figure 3: Horizontal (blue) and vertical (red) coherent oscillations measured after a horizontal kick.

3. Coupling Dependence of Touscheck Lifetime

The Touscheck lifetime has a high sensitivity to the coupling ratio in the single-bunch mode of the SPring-8 storage ring. The measured lifetime as a function of the coupling ratio estimated from the measurement of the mode frequencies at the single-bunch mode of 1 mA/bunch is shown in Figure 4. The 0th order dependence of Touscheck lifetime (τ_T) on coupling ratio (κ) is given by the following equation.

$$\tau_T = c \times \sigma_x \times \sigma_y \times \sigma_\ell = A \times \sigma_\ell \times \sqrt{\kappa}/(1+\kappa) ,$$

where σ_x is the bunch width, σ_y the bunch height and σ_ℓ the bunch length. Only the constant of A was calibrated by using the relation between lifetime and coupling ratio obtained by the four measurements of the coherent oscillation. The theoretical lifetime obtained as a function of coupling ratio is a solid line in this figure. The agreement between the theoretical line and the measured data is very good. From the lifetime of about 3 hours measured at the operation point of (51.11, 16.32), the minimum coupling ratio is estimated to be around 0.04%.

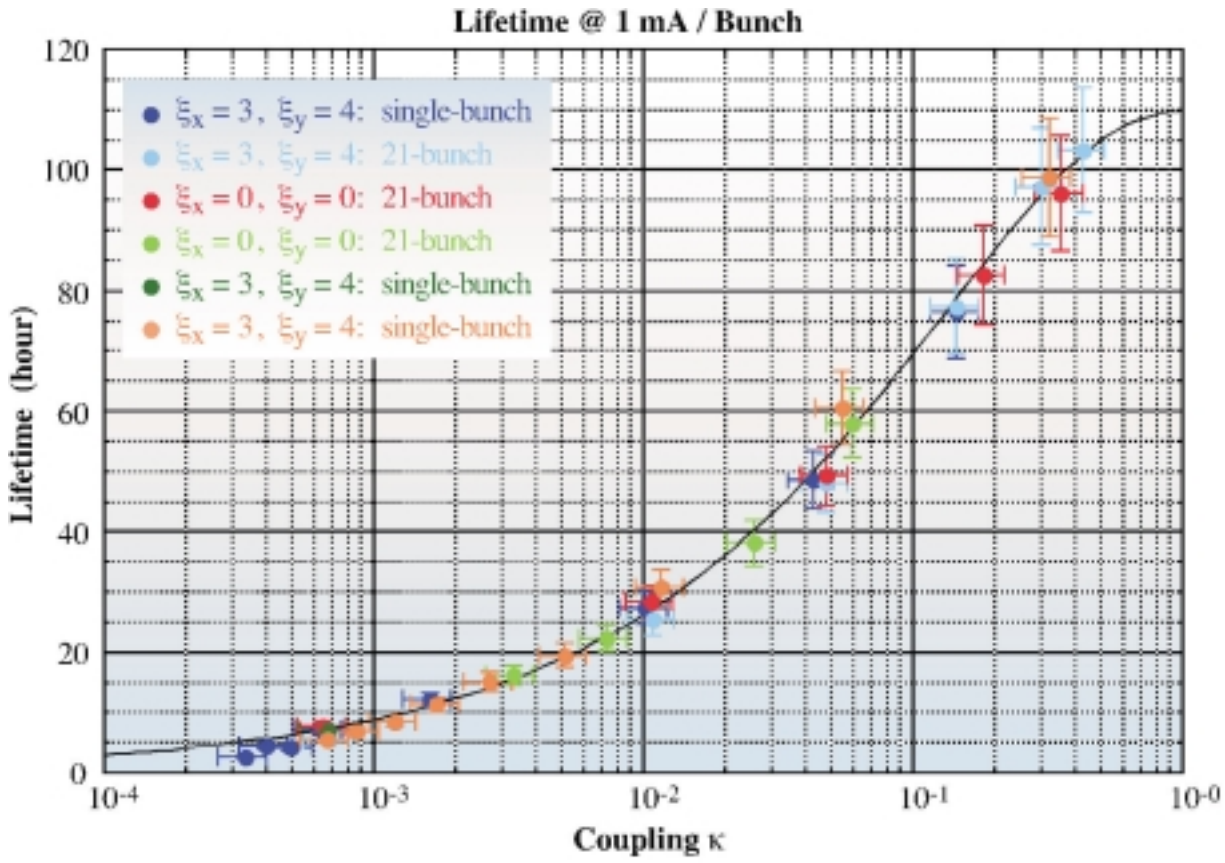

Figure 4: Beam lifetime as a function of betatron coupling (κ); solid line shows the theoretical Touschek lifetime.

4. Measurement of Visibility by Interferometer

The visibilities of visible light from a bending magnet and an X-ray from an ID taken by an interferometer directly give the vertical electron beam size. These visibility measurements are now underway. As a preliminary result for visible light, a beam size corresponding to the coupling ratio of 0.2% as an upper limit has been obtained under normal operation (51.16, 16.32).

Orbit Stability

In the third generation synchrotron radiation source, stability of the electron beam orbit is one of the most important performance requirements for achieving a highly brilliant photon beam. In the construction design of the SPring-8 storage ring, the effect of perturbation sources inducing orbit movement was minimized. Consequently, an orbit stability of less than 70 μm was achieved in the horizontal and vertical planes without any feedback control. The digital feedback system was developed to further stabilize the electron orbit. The system corrects only the COD components corresponding to the betatron tune harmonics and those of its satellite in the horizontal and vertical directions and a beam energy at intervals of 1 min. The results are shown in Figure 5. The obtained beam stability is 0.8 μm (in rms) for the 51st betatron tune harmonic in the horizontal COD and 0.5 μm (in rms) for the 16th harmonic in the vertical COD. Also, the circumference change corresponding to the 0th harmonic in the horizontal COD was corrected within 0.3 μm (in rms) by adjusting the RF frequency. The system is now routinely employed in the user service mode operation.

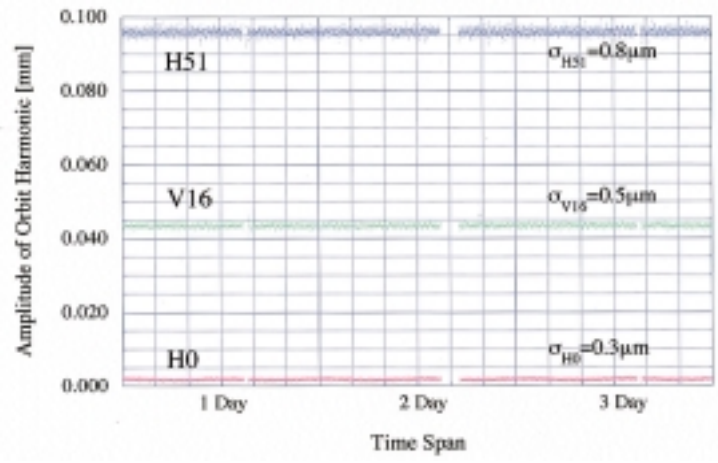

Figure 5: Amplitude changes of tune harmonics (51st for horizontal (blue) and 16th for vertical (green)) and 0th harmonic (circumference change (red)) in COD for three days with periodic correction of global orbit.

Brilliance

In the SPring-8 storage ring, the brilliance of the photon beam is achieved to nearly the diffraction limit in the vertical plane due to an extremely low coupling ratio. In Figure 6, the relative brilliance, normalized by the value of the vertical limit, is plotted for three different vertical betafunctions at the ID section as a function of the wavelength. The relative brilliance at the wavelength of 1 Å is about 0.3 at the present operation of β_y=8 m. This value is almost the diffraction limit for the user because the photon beam size at a user position of more than 30 m away from the source point is not determined by the vertical emittance of the electron beam and the vertical beta function at the ID position but mainly by the angular divergence of the photon beam. Therefore, we now have no plans for the optimization of β_y in the ID section to improve brilliance.

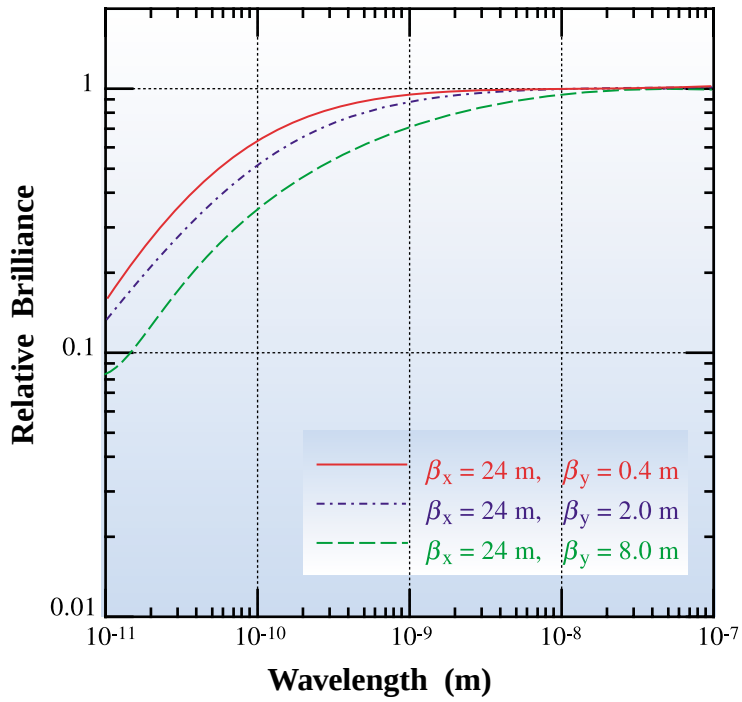

Figure 6: Relative brilliance as a function of wavelength for three different β_y at ID section: β_y = 8.0 m in normal operation and β_y = 0.4 m with optimization of brilliance to maximum value.

Plans for Next Year

We are scheduling:

- the installation of a top-up operation mode to effectively improve lifetime,
- the development of new-type injection magnets to achieve an injection orbit error of less than 0.1mm in top-up operation,
- the correction of fast orbit movement with a frequency of more than 0.1 Hz,
- the correction of the coupling ratio and residual vertical dispersion by skew quadrupole magnets, and
- the construction of a long straight section of 30 m, with beam commissioning scheduled for the autumn of 2000.

Noritaka Kumagai
SPring-8 / JASRI

In-vacuum undulators

The in-vacuum undulator is an insertion device (ID) adopted as a standard light source at SPring-8. Because magnet arrays are contained in the vacuum chamber, the magnetic field of the in-vacuum undulator is much stronger than that of conventional undulators. In order to construct in-vacuum undulators, many techniques and procedures have been developed: magnetic-field correction, attachments for impedance reduction and bake-out systems for ultra-high vacuum. The first four devices were installed in the SPring-8 storage ring from November 1996 to February 1997, and the first radiation was observed in April 1997 without any problem.

Introduction

The insertion device is one of the most important apparatus determining the performance of a synchrotron radiation facility. In order to meet the various requirements of users, many kinds of insertion devices (IDs) such as elliptic wiggler, in-vacuum, helical and figure-8 undulators have been constructed and installed in SPring-8 [1-5]. Using these IDs makes it possible to obtain photons with circular and linear polarization in the energy range between 100 eV and 300 keV. Among them, the in-vacuum undulator is regarded as a standard ID at SPring-8. It provides an X-ray between 5 keV and 80 keV using up to the 5th harmonic.

The in-vacuum undulator is an ID with magnet arrays inside the vacuum chamber. Because no obstacle exists within the magnet gap (*i.e.*, no intervening vacuum-chamber wall), the vacuum gap is equal to the magnet gap, meaning that the vertical aperture is variable. Thus, the in-vacuum undulator is suitable for the commissioning of the storage ring. Therefore, four in-vacuum undulators were installed before starting commissioning of the storage ring. The in-vacuum undulators have another advantage in that the magnetic field is stronger than that of the conventional IDs of out-of-vacuum type. In order to construct in-vacuum undulators, many techniques have been developed at SPring-8. This report provides an outline of these techniques.

Figure 1: Photograph of in-vacuum undulator; ion and NEG pumps are not attached yet.

Specifications

Figure 1 is a photograph of the in-vacuum undulator. The specifications of the device are shown in Table I. Each 4.5 m undulator consists of three1.5 m segments. The mechanics, vacuum chambers and pumps are all standardized for easy maintenance and mass production. The periodic length of 32 mm was determined so that the energy of the 1st harmonic could range from 5 keV to 18 keV. Actually, up to 80 keV is possible by using 3rd and 5th harmonics. Figure 2 is a photograph of one magnet unit used in the in-vacuum undulator. In order to achieve an ultra-high vacuum, mechanical clamps are used to fix the magnet block instead of glue.

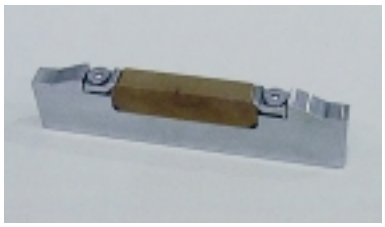

Figure 2: One magnet unit of the in-vacuum undulator; four magnet units form one period.

Table I *: Specifications of the standard in-vacuum undulator at SPring-8.*

Type	Pure Permanent Magnet
Magnet material	NdFeB
Length	4.5 m
Periodic length	32 mm
Number of periods	140
Minimum gap	8 mm
Maximum K value	2.3
Available energy (1st harmonic)	5 keV ~ 18 keV

Field Correction

Because the magnets forming the ID field are not perfect, some corrections are necessary before installation. In general, there are two kinds of field corrections. One is spectral correction for restoring spectral intensity of radiation, and the other is multipole correction for reducing the multipole component of the ID field error. In both cases, chip magnets are inserted into holes made in magnet holders to increase or reduce the magnetic field. Chipping is used instead of shimming for field correction to avoid an increase in impedance.

For spectral correction, the conventional method is to reduce the optical phase error [6]. At SPring-8, however, another quantity called error storage is used to estimate the spectral performance [7]. This represents how the field error is stored at each period of the ID and is closely related to the optical phase error. Because the error storage is found by a simpler calculation than that for optical phase, the procedure for spectral correction is simplified. For the multipole correction, special holders in which more chip-magnets can be inserted are attached to both ends of the magnet arrays, and a chip-magnet arrangement is determined to minimize the multipole component by the simulated-annealing method [8]. In the calculation, the dipole components are neglected because steering coils located upstream and downstream can easily correct them.

Figure 3 shows an example result this spectral correction. The peak flux density at each harmonic normalized by the ideal value is shown before and after spectral correction. The standard deviations of the error storage before and after correction are 5.5% and 1.3%, respectively. With an increase in harmonic number, the restoration of intensity is more remarkable. For example, the normalized flux density at the 11th harmonic before correction is only 23% of the ideal one, while that after correction is 60%. It should be noted that the standard deviations of the peak field at each magnet pole before and after correction are 0.34% and 0.32%, respectively, meaning that the restoration of intensity is not a result of a reduction in the deviation of the peak field. In addition, the r.m.s. phase error before and after spectral corrections are 15.4 and 3.9 degree, respectively, showing that the reduction in error storage causes the reduction in phase error. From these observations, we can conclude that reducing error storage is an adequate method of spectral correction.

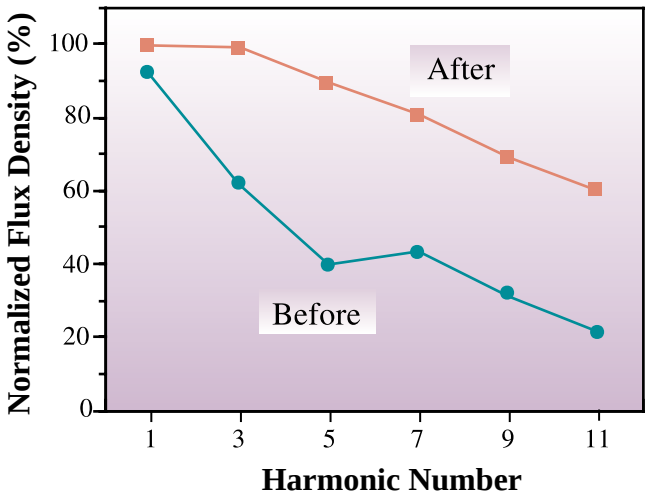

Figure 3: Comparison of the normalized flux density for various harmonics before and after spectral correction.

Table II shows an example result of multipole correction. Normal-quadrupole, normal-sextupole, skew-quadrupole and skew-sextupole components are shown as functions of the gap before and after multipole correction. Clearly, all multipole components were reduced considerably.

Table II : Multipole components before and after correction.

Gap (mm)	Normal Quad. (G.cm/cm)		Normal Sext. (G.cm/cm^2)		Skew Quad. (G.cm/cm)		Skew Sext. (G.cm/cm^2)	
	Beafre	After	Beafre	After	Beafre	After	Beafre	After
8	343	4	-97	25	-11	-11	-207	2
10	306	23	-80	-1	11	-5	-148	23
12	275	29	-69	-42	27	-4	-102	11
15	238	26	-57	-59	41	5	-102	33
20	188	41	-35	-43	48	0	-31	3
30	121	38	-22	-20	41	-2	-5	2

Impedance Reduction

Unlike conventional IDs, the in-vacuum undulator is equipped with two special attachments to reduce the impedance in the electron path. One is an RF finger to smoothly connect the end of the magnet array and adjacent vacuum duct. The RF finger developed at SPring-8, called a flexible transition, is made of a woven strip of copper and can follow the movement of the ID gap from 8 mm to 50 mm (Figure 4). The other attachment is a thin metal foil covering the magnet surface. This is necessary because the magnet surface as seen by an electron is not smooth but has many gaps between adjacent magnet units.

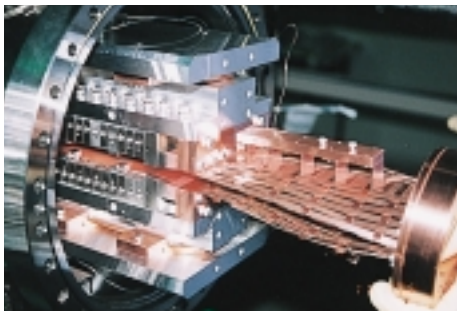

Figure 4: RF finger developed at SPring-8; the cooling water channel is attached before assembling all other components

In the first stage of in-vacuum undulator development, a 50 μm stainless steel sheet was used to cover the magnet surface and no cooling channel was attached to the RF fingers. In the beam test of this in-vacuum undulator at the ESRF in August 1996 [7], it was observed that the temperature of the RF finger rose 473 K and the beam was completely lost at a gap of 8 mm. In addition, the stainless steel was found to be partially melted after opening the vacuum chamber. To solve these problems, two improvements were made. One was to attach a cooling channel to the RF finger to remove the heat. The other was to replace the stainless-steel sheet with a 50 μm Ni sheet for thermal contact between the sheet and the magnet blocks by the attractive force. Because the magnet blocks are cooled by water during operation, heat originating in the sheet can easily escape. In addition, the Ni sheet is coated with a 10 μm copper layer to reduce the resistive wall heating.

Bake-out and Vacuum System

The bake-out system is one of the most important and difficult factors in constructing the in-vacuum undulator. Specifically, there are two important requirements. One is that the temperature of the magnet should not exceed 408 K to avoid demagnetization. The other is that the difference in heat expansion between the aluminum beam and the vacuum chamber (made of stainless steel) should be within 1 mm so that no unnecessary stress is placed on the RF fingers and bellows, these absorb the movement of the gap. To meet these requirements, the temperature of the magnet arrays is finely controlled with pressurized hot water to keep it at 403 K during the 48-hour bake-out process.

The in-vacuum undulator contains a large number of components. For example, the number of magnet blocks and holders is over two thousands. Accordingly, six ion pumps capable of 125 l/sec and twelve NEG pumps (non-evaporated getter pumps), capable of 500 l/sec are attached to obtain sufficient pumping speed. The surface of each magnet block is coated with a 5 μm layer of TiN to avoid outgas from pure-permanent magnet material.

After assembling all components of the first in-vacuum undulator except for the connecting parts between the device and the vacuum duct of the storage ring, an off-line vacuum test was performed. Figure 5 shows the results. The horizontal axis shows time after the end of the bake-out process and the vertical axis shows pressure. Two values of the pressure measured by different ion gauges attached to the upstream and downstream segments are shown. The figure shows that there is no difference between the upstream and downstream pressures and that a pressure is 5.6×10^{-9} Pa can be achieved, which is sufficient for installation in the storage ring.

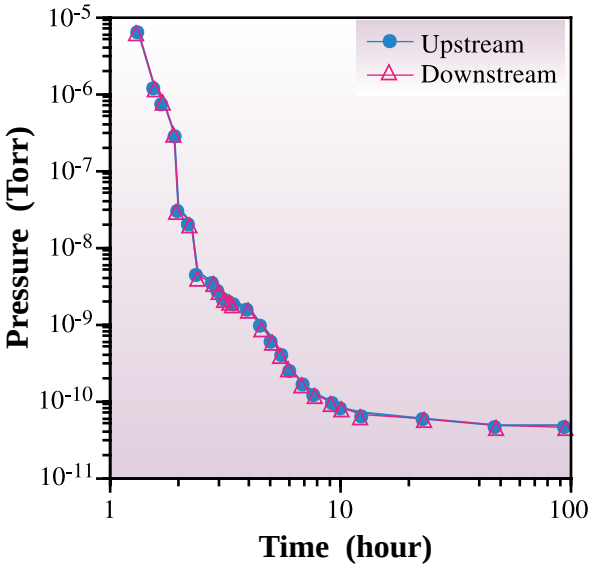

Figure 5: Off-line result of vacuum test of the in-vacuum undulator (pressure is shown as a function of time after the end of the bake-out process).

Installation and First Observation

The first four in-vacuum undulators were installed in the SPring-8 storage ring between November 1996 and February 1997. The pressure of all these devices reached below 1×10^{-8} Pa after the bake-out process. One of them was a vertical undulator having a horizontal magnetic field instead of a vertical field to obtain vertically polarized radiation [9]. After commissioning of the storage ring, the first radiation of the in-vacuum undulator installed at the beamline BL47XU was observed in April 1997. Figure 6 shows a photograph taken at that time. The radiation from the in-vacuum undulator irradiated a screen monitor located at the front-end section of the beamline. The gap was 20 mm and the storage-ring current was 0.047 mA. The bright circle seen in the center is the radiation from the in-vacuum undulator.

Figure 6: Photograph of screen monitor irradiated by radiation from the in-vacuum undulator.

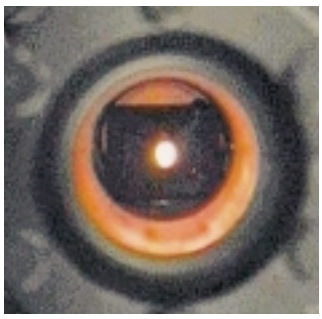

Operation

At present, twelve in-vacuum undulators are in operation at SPring-8. In the early operation, a degradation of lifetime was observed while closing the gap. For example, the lifetime degraded 30% at gap of 8 mm. Such degradation has not been observed recently due to improvement of the storage ring's vacuum. Thanks to the improvements described in Section 4, no significant temperature rise in RF finger and magnet arrays has been observed so far. The closed orbit distortion (COD) during tuning of the photon energy, *i.e.*, changing the ID gap, has been corrected by steering coils located upstream and downstream of the ID. After such COD correction, it was found that the displacement and the deflection due to tuning are within 10% of the electron-beam size and divergence, respectively. Measurements of radiation spectra from the in-vacuum undulators have been performed at various beamlines and have shown that the measured spectral shape is equivalent to our expectations.

Summary

Construction and operation of the in-vacuum undulator at SPring-8 have been described. Many other techniques besides those described here have been developed in construction and operation of the in-vacuum undulator. These all techniques have been applied to constructing not only in-vacuum undulators but also other IDs such as elliptic wiggler, helical undulator and figure-8 undulator.

References

[1] H. Kitamura, *J. Synchrotron Rad.* **5** (1998) 184.
[2] X. M. Marechal *et al., J. Synchrotron Rad.* **5** (1998) 431.
[3] T. Hara *et al., J. Synchrotron Rad.* **5** (1998) 403.
[4] T. Hara *et al., J. Synchrotron Rad.* **5** (1998) 426.
[5] T. Tanaka *et al., J. Synchrotron Rad.* **5** (1998) 459.
[6] R. P. Walker, *Nucl. Instrum. Meth. A* **335** (1993) 328.
[7] T. Tanaka *et al., SPring-8 Annual Report* (1998).
[8] S. Kirkpatrick *et al., Science* **220** (1983) 671.
[9] T. Tanaka *et al., J. Synchrotron Rad.* **5** (1998) 414.

Takashi Tanaka and Hideo Kitamura
SPring-8 / RIKEN·JASRI

Transport Channel and Optics

One and a half year's experience in operation of standard double crystal monochromators for both X-ray undulators and bending magnet beamlines demonstrated their precision and performance. However, minor revisions were made on the monochromators for the second phase beamlines to improve controllability and exchangeability. Vacuum chambers, which used to be differentiated between the bending magnet (BM) and undulator (U) types, have been standardized with the CF152 inlet and outlet light path flanges. Zero-length conversion flanges (CF152-CF70) are used for the U-type. Horizontal translations perpendicular to the beam axis for both first and second crystals were changed from manual to stepping-motor driven. Horizontal translation of the vacuum chamber perpendicular to the beam axis was also introduced.

In the standard undulator's double-crystal monochromator, the first crystal is cooled by water flowing into the pinpost structure just underneath of the irradiated surface (Figure 1). To fabricate the pinpost water path structure, we are developing a strain-free diffusive bonding technique [1]. We found no thermal problems in our (world's strongests) undulator beamlines. However, the initial design of the water path (Figure 2) was found to introduce pressure-induced strain. Accordingly, we made a new design (Figure 3) and fabricated some prototype crystals. Pressure-induced strain has been greatly suppressed by this new design, although some bonding strain still remains. We are now working to improve the bonding process in collaboration with NEC Corp..

Liquid nitrogen (LN) cooling of the undulator monochromator was tested at an optics R&D beamline (BL47XU). Copper blocks at liquid nitrogen temperature were used to indirectly cool both the first and second crystals. The test result is fairly good as reported from ESRF and APS. However, we found some operational problems in our current system, so we will start development of a new LN circulating system with a liquid He refrigerator.

Near-perfect and large-size diamond crystals synthesized by Sumitomo Electric Industry Co. Ltd. have widened the applications of the diamond crystal to SR X-ray optics [2]. One of the most promising is that for an X-ray phase retarder [3-5], which converts linear polarization to circular polarization. Owing to the birefringence effects in the dynamical diffraction of X-rays, easy switching of the left-hand circularity (LHC) and right-hand circularity (RHC) throught slight changes in the crystal orientation is realized. We developed a PZT-driven bi-stable crystal oscillator which gives rise to LHC and RHC alternatively at two stable positions with an oscillation frequency of more than 40 Hz. The output currents of two ionization chambers are lock-in amplified in synchronization with the PZT oscillation. This technique was successfully applied to the measurement of magnetic circular dichroism (MCD) for transition metal compounds and other materials [6]. The MCD data accumulated in 30 min by this method was proven to have higher quality than the data accumulated in 10 hrs at elliptical multipole wiggler beamline at the Photon Factory.

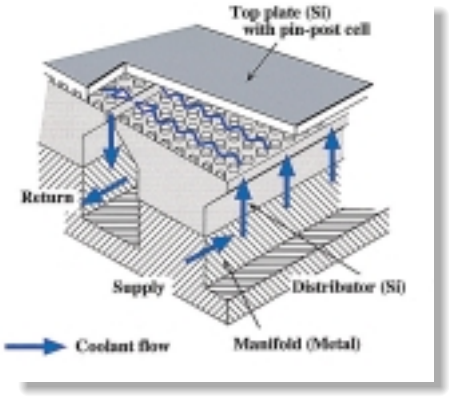

Figure 1: Pinpost water cooling.

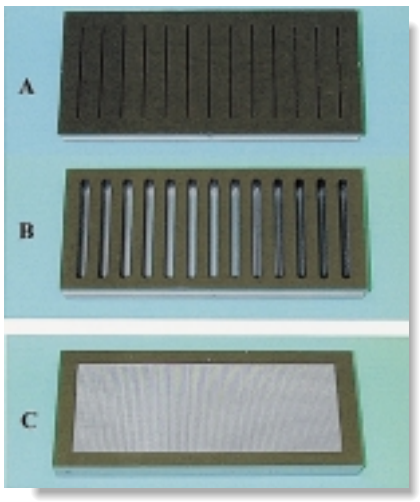

Figure 2: Initial-design pinpost crystal: (A) water distributor (bonded side), (B) water distributor (rear side) and (C) top plate with pins.

Figure 3: Improved-design pinpost crystal: (A) water distributor (bonded side), (B) top plate with pins before mechano-chemical polishing.

The Optics Group has been developing a novel mechanism of crystal bending for dynamic sagittal focusing. The mechanism is to be used for the second crystal of the standard bending-magnet X-ray monochromator. Our technical concern is to keep the fixed exit feature of the double crystal along monochromator with a varying bending radius [7]. With some modification from the initial design, the bending mechanism became nearly perfect. We could obtain a fairly good focus point at 40 keV without affecting the fixed exit feature.

In collaboration with Shin-Etsu Semiconductor Co. Ltd., SPring-8 is developing a large diameter <110>-grown FZ silicon crystal for various crystal monochromators. The advantage of the <110>-grown crystal is that we can cut large size (111), or more generally (hkk), plates that are parallel to the growth axis. In 1995, when we started the collaborative development, the technical limit of the maximum diameter was 3 inches and that of the maximum length was around 500 mm. However, in 1997 Shin-Etsu succeeded in growing 4-inch diameter ingots and the maximum length now exceeds 700 mm. These ingots are routinely used for monochromator crystals, in particular for the rotated-inclined crystals in X-ray undulator monochromators where such a large crystal plate is essential to accomodate the long footprint on the surface.

For the development and fabrication of the newly designed crystal optical elements, SPring-8 set up a crystal machining facility (Figure 4) that includes a numerically controlled (NC) cutting machine with diamond saw, a NC diamond milling machine, a grinding machine for silicon and a mechano-chemical polishing machine for silicon. The crystal stage for the cutting and milling machines are compatible with that of the X-ray diffractometer, which enables accurate agreement between the cut surface and the desired crystal orientation. Most of the trial fabrications of the crystal optical elements can, in principle, be made in-house. For the off-line test of these crystal optical elements, two sets of versatile multiple-axis diffractometers were equipped with rotating-anode X-ray generators as the X-ray source. The two diffractometers were identical, components were fully compatible and have the same design principle as many similar diffractometers in the SR beamlines.

SPring-8 is preparing to set up a mirror characterization facility, which will be operational from October 1999. This facility will be equipped with a Long Trace Profiler, Wyko interferometer and Zygo interferometer. Incorporating the work of Prof. Kinoshita of the Himeji Institute of Technology, we will have the most advanced mirror characterization facility in Japan at the SPring-8 site.

Figure 4: Crystal fabrication facilities at SPring-8: (A) grinder, (B) diamond cutter, (C) diamond milling machine and (D) mechano-chemical polisher.

References

[1] M. Kuroda *et al., J. Synchrotron Rad.* **5** (1998) 1211.
[2] N. Toda *et al., SPIE Proc.* **3151** (1997) 329.
[3] K. Hirano *et al., Jpn. J. Appl. Phys.* **30** (1991) L407.
[4] K. Hirano *et al., Rev. Sci. Instrum.* **66** (1995) 1604.
[5] T. Uruga *et al., Rev. Sci. Instrum.* **66** (1995) 2254.
[6] M. Suzuki *et al., Jpn. J. Appl. Phys.* **37** (1998) L1488.
[7] Y. Furukawa and T. Ishikawa, *SPring-8 Annual Report* **1995** (1996) 191.

Tetsuya Ishikawa
SPring-8 / RIKEN·JASRI

DETECTORS

Requirement for New Detectors in SPring-8: an Overview

SPring-8 is a third generation storage ring characterized by its low emittance of radiation. The detectors in SPring-8 have to match this characteristic of the source. The detectors currently used at SPring-8 are mostly those, that have been used in other synchrotron radiation facilities and even with laboratory X-ray sources, such as ionization chambers, scintillation counters, solid-state detectors and image plates. These detectors are useful in many experiments and their best advantage is that users are familiar with them. However, in order to make full use of the synchrotron radiation from SPring-8, it is clearly desirable to find and develop detectors that match the characteristic of SPring-8.

The low-emittance X-ray radiation of SPring-8 is currently posing two requirements on area detectors: fast readout and high spatial resolution. The former has partially been fulfilled by the use of CCD as a readout device: although the readout time of CCD is slower than most photon-counting detectors, it is probably the fastest among integrating detectors such as an image plate. The latter problem has also been partially solved by the use of CCD: the pixel size of CCD is small enough for most purposes. SPring-8 also provides high photon flux which is hard to handle with photon-counting detectors. Since CCD is an integrating-type detector, it is suitable for SPring-8 for this point, also. As an X-ray detector, CCD is versatile and easy to use, which has been demonstrated by its popularity among users of many fields.

Current Status of Area Detectors

R-AXIS IV

As an area detector, an image plate is still the most widely used detector in SPring-8. In diffraction experiments in both biological and non-biological fields, RIGAKU R-AXIS IV is the detector most often. At the moment, BL10XU, BL24XU, BL41XU, BL44B2 and BL45XU are equipped with it. Among these beamlines, all except BL10XU are for protein crystallography: in fact, all protein crystallography beamlines are using R-AXIS IV at the moment. R-AXIS IV has two plates of 30x30 cm so that when one is scanned by a laser for readout, the other can be exposed.

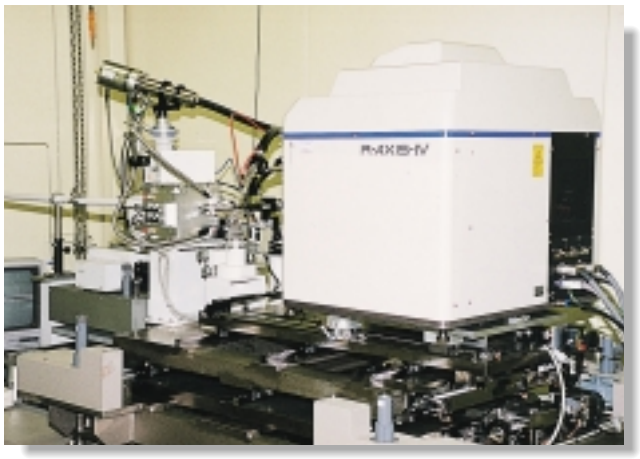

RIGAKU R-AXIS IV detector.

This choice of R-AXIS IV is generally welcomed by users because most of them use the same detector with their laboratory X-ray source. On the other hand, since this detector was for laboratory use, it is designed for a long exposure time and so the readout takes 5.5 minutes. For beamlines in SPring-8 where an exposure is typically 5-60 seconds, this is unreasonably long.

X-ray image intensifier and fast CCD

For the fast time-resolved recording of images, a fast CCD is used with an X-ray image intensifier. The X-ray image intensifier with a beryllium window was developed in a SPring-8 R&D program in collaboration with Prof. Amemiya of Tokyo University and Hamamatsu Photonics. At the BL45XU small-angle station, this combination is used extensively in both the time-resolved and static measurements of X-ray diffraction and scattering from biological specimens. To improve the time-resolution, the phosphor in the exit window of the image intensifier is P43 which has a persistence shorter than 3 msec. The CCD is Hamamatsu C4880-80-14A with air-cooling to 0˚ C and a frame rate of 28 per second with 656x494 pixels. The ADC is 10 bits with a noise level within one bit. By reducing the number of lines in each frame, the rate can be increased to 500 frames per second with 656x15 pixels. So far, time-resolved experiments on skeletal and cardiac muscles and purple membranes have been made using this detector. It has also been used at BL44B2 to record time-resolved white Laue diffraction.

Beam monitor

High-resolution imaging detectors are becoming increasingly important because the low-emittance of the SPring-8 radiation provides a smaller and parallel X-ray beam. This makes it possible to observe the interference or refraction of X-rays that appear as fringes of a few microns to a few tens of microns. As this is probably one of the most adequate applications of the low-emittance beam of SPring-8, detectors targeted for this purpose have been developed. Currently, the detector most widely used is called the "beam monitor" since it was designed to observe a monochromatized direct X-ray beam in an undulator beamline. In its design, it is capable of recording a beam whose flux is as high as on the order of 10^{12} per mm^2. It is composed of a phosphor (P43) and a tandem lens, and a reflecting mirror. In order to reduce the radiation damage in the optic system, a pair of lead glasses is placed behind the phosphor. The present design uses a 1000x1014 pixel cooled-CCD (Hamamatsu C4880-10-14A) as the camera. The spatial resolution is about 25 μm. It has been used in most of the imaging experiments done at BL47XU. For time resolved experiments with a high spatial resolution, the camera can be replaced by a fast CCD (C4880-80-14A).

"Beam monitor".

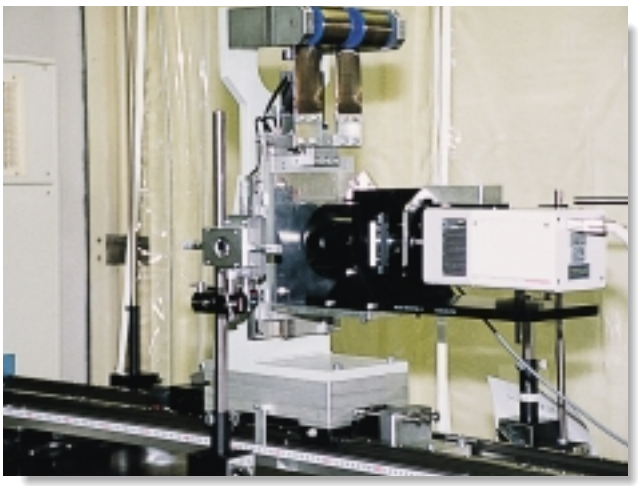

"Beam monitor" detection system at BL47XU.

Future Prospects

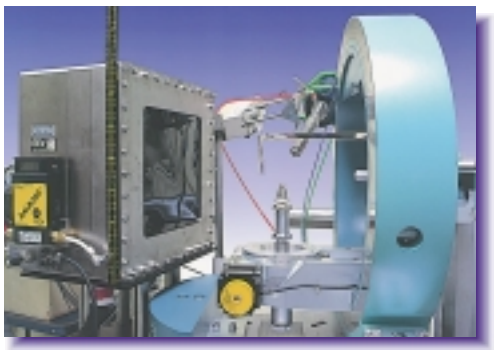

MCCDX detector system.
Ref. Suzuki et al., Nucl. Instrum. Meth. Phys. Res. A (1999) - in press.

CCD detectors for protein crystallography

Although R-AXIS IV is widely used, some beamlines for protein crystallography will also be equipped with a CCD detector with tapered fiber optics. For the BL45XU protein crystallography station, a detector with 4x4 CCDs (1242x1152 pixels each) has been developed. It will be installed when the data processing software to be used becomes ready. The readout is 6 seconds. This will be short enough to match the typical exposure time in the undulator beamline.

Shortening the readout of R-AXIS IV

Improving R-AXIS IV to reduce the turn-around time to shorter than 1 minute has been discussed with RIGAKU and prototypes will be manufactured in 1999. As there will be no change in the basic design, it will remain friendly to users. On beamlines that provide a moderately strong beam, it may remain as the user's best choice.

Improving the resolution of CCD detectors

For high resolution imaging, CCD detectors must be improved to achieve a higher resolution. In principle, by using optics similar to that in a microscope, it is possible to achieve spatial resolution of a few microns. However, attention should be paid so as to avoid radiation damage on the optical components by the intense X-ray beam. Discussions on new designs for CCD detectors are currently underway with Hamamatsu Photonics who will be manufacturing detectors for tests.

High energy X-ray detector

One important feature of SPring-8 is that it is a high energy storage ring that can produce X-rays of high energy (>100 keV). Since this energy range has not been available in most synchrotron radiation facilities to date, detectors have not been developed extensively. Actually, this range will be the region of exploration in SPring-8. CdZnTe is an obvious candidate in such an energy region because of its high photon stopping power. However, considerable R&D will be required to achieve detectors that are usable in actual experiments.

Fast detectors

Since CCD is now widely used in commercial products, its technical development has been rapid. Along that line, it will be feasible to make a very fast CCD camera with a frame rate higher than 1000 per second. A time resolution higher than this can be obtained by using photon counting detectors. A wire detector using microstrip technology has been developed for the BL45XU small-angle station by Dr. Tanimori of the Tokyo Institute of Technology, but it is still not usable in actual experiments. Typically, the requirement for a high time resolution accompanies that for a high counting rate since a certain number of photons are required in recording an image or a diffraction pattern of an acceptable quality. Most wire detectors can handle only less than 3 million photons per second, which is not sufficient. Therefore, more sophisticated electronic equipment is required to solve this problem.

Naoto Yagi
SPring-8 / JASRI

Facility Status

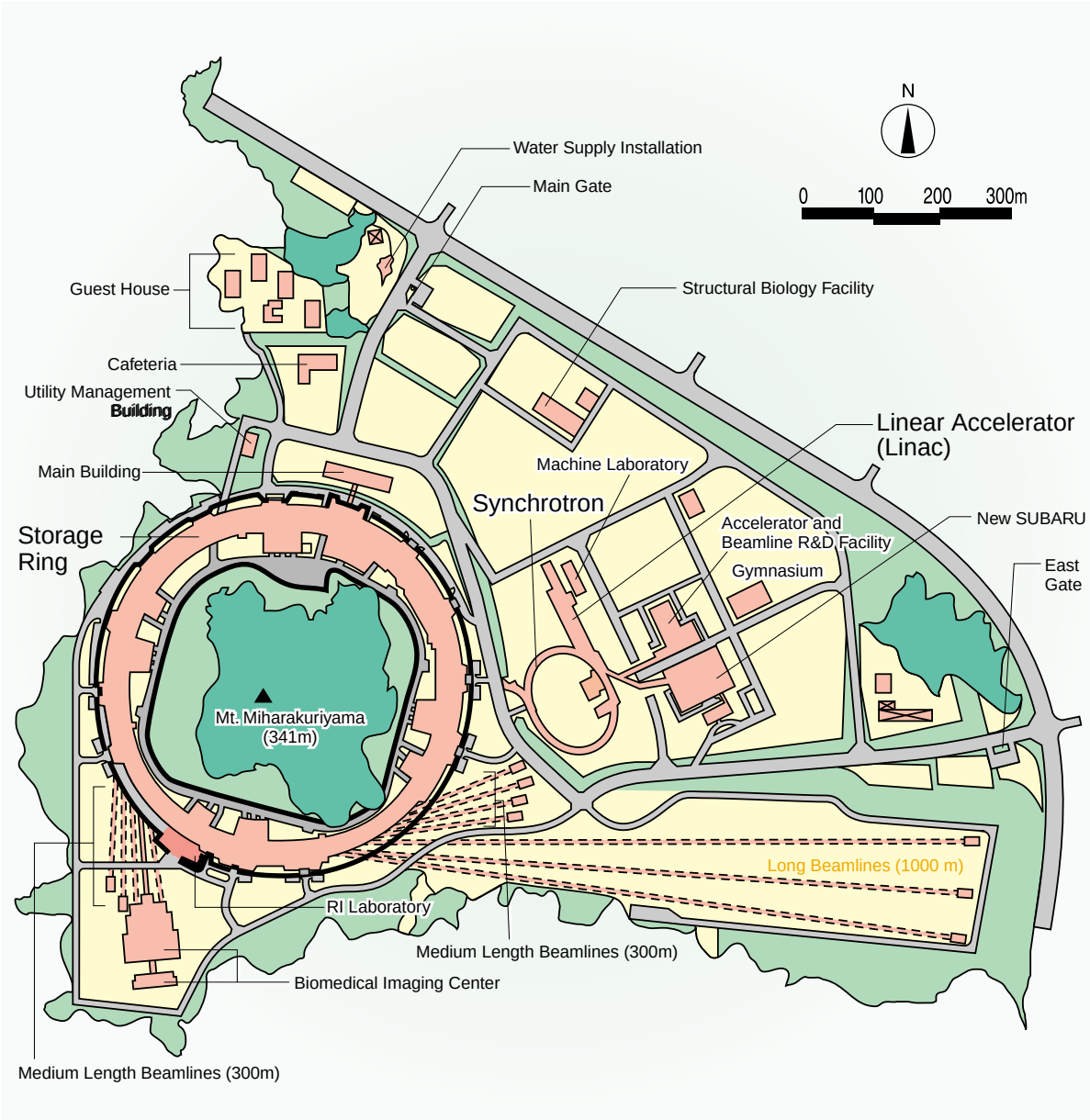

MACHINE OPERATION

In 1998, the SPring-8 storage ring was stably operated in two- or three-week modes for one cycle. The total operation time of the storage ring was 4190 hours. Within this operation time, 2624 hours (62.6%) had been provided to the users and 110 hours (2.6%) was loss time due to failures of machines and beamlines. The most significant failure in 1998 was the breakdown of the power supply of sextupole magnets which caused loss time of 15 hours. The remaining 1456 hours were used for the tuning and study of accelerators (Linac, synchrotron and storage ring) and beamlines, and for the commissioning of new beamlines.

The filling modes in the user time are shown in Figure 1. A 62.3% of the total user time was operated in multi-bunch mode, as full filling mode or 2/3 filling mode, and the remaining time was several-bunch mode, such as a 21-bunch mode (21 equally spaced trains of 3 or 7 bunches) with a total current of 70 mA, 10-bunches + partial filling and so on. A current of 0.5 or 1 mA/bunch was stored, and the purity was better than 10^{-6} in the user operation. Also, the current /bunch was stored until 12 mA without observing any beam instability in a machine study, and the bunch current was limited by decreasing vacuum pressure due to heating of the bellows port.

The beam lifetime depends strongly on these filling modes. The lifetime at a total current of 70 mA for full filling mode is about 90 hours, and that for several-bunch mode with 1mA/bunch is less than 6 hours when the insertion device's (ID) gap was fully opened and about 15-20 hours when the ID gap was closed (in user-service mode). It appeared that the increase in lifetime was due to the very weak skew component in the ID. The electron beam was refilled or accumulated at a repetition of once or twice a day.

Furthermore, service of a 1 GeV electron beam to the New SUBARU ring was started from September 1998 as a parasite mode of the Linac operation. The New SUBARU ring is a 1.5 GeV synchrotron/storage ring built by the Himeji Institute of Technology for their synchrotron radiation use. At present, a current of about 10 mA can be stored with a lifetime of several minutes, and irradiation of the chamber surface by the photon beam is now being studied to improve the lifetime.

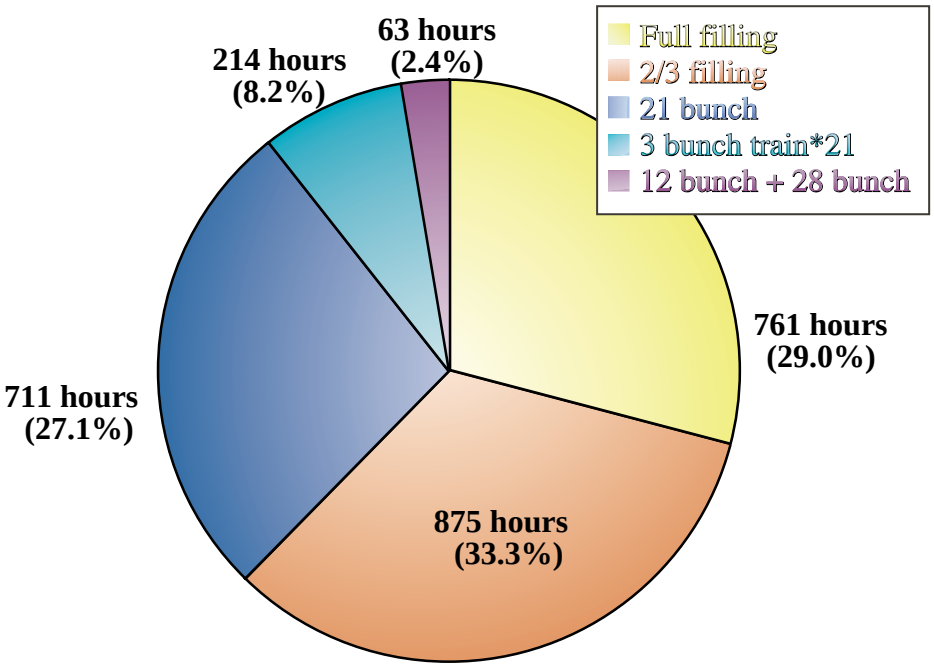

Figure 1: Filling modes during user time in 1998.

BEAMLINES

SPring-8 decided to accept an additional beamline proposal for infrared studies, so the total number of available beamlines is 62 instead of 61 as initially planned.

Beamlines at the SPring-8 Facility are categorized into four types:

- Public beamlines constructed by SPring-8 and open to public use
- JAERI/RIKEN beamlines constructed by JAERI/RIKEN for their exclusive use
- contract beamlines constructed by the proposers for their exclusive use
- R&D beamlines constructed by SPring-8

At the end of 1998, ten public beamlines were operated for public use as:

BL01B1	XAFS
BL02B1	Crystal Structure Analysis
BL04B1	High-Temperature Research
BL08W	High-Energy Inelastic Scattering
BL09XU	Nuclear Resonant Scattering
BL10XU	Extremely Dense State Research
BL25SU	Soft X-ray Spectroscopy of Solid
BL27SU	Soft X-ray Photochemistry
BL39XU	Physicochemical Analysis
BL41XU	Bio-Crystallography

A Biomedical Imaging beamline, BL20B2, which extends over 200 meters from the X-ray source point, was completed in the autumn of 1998. In 1998, construction began for several more public beamlines:

BL02B2	Powder Diffraction
BL04B2	High-Energy Scattering/Diffraction
BL20XU	Medical Use
BL20B2	Medical and Imaging Application R&D
BL28B2	White Radiation Topography
BL35XU	High-Energy Resolution Inelastic Scattering
BL40XU	High-Flux Undulator
BL40B2	Structural Biology
BL43IR	Infrared Studies

Of these, the bending magnet beamlines, BL02B2, BL04B2, BL20B2, BL28B2 and BL40B2, were scheduled to be finished by the end of FY1998 and will be available for trial use in 1999.

An R&D beamline, BL47XU, was completed and partly made available for public use mainly in the fields of imaging and detector development. The second R&D beamline, BL46XU, will be completed with an experimental hutch.

BL46XU	R&D (1) (RIKEN)
BL47XU	R&D (2) (RIKEN)

Six beamlines of JAERI and RIKEN have been constructed for exclusive use by JAERI/RIKEN scientists:

BL11XU	Materials Science (JAERI)
BL24B1	Materials Science (JAERI)
BL23SU	Actinide Studies by Soft X-ray (JAERI)
BL29XU	Coherent X-ray Studies (1 km beamline) (RIKEN)
BL44B2	Structural Biology II (RIKEN)
BL45XU	Structural Biology I (RIKEN)

Of these, the BL29XU undulator beamline will be extended out of the Experimental Hall to an experimental station 1 km from the source. RIKEN started construction of a 30-m-long straight section beamline, BL19IS, from FY1998 and will complete it in FY 2000. Several units of undulators are to be installed for coherent hard X-ray studies.

BL19IS	RIKEN(4) (30 m beamline)(RIKEN)

Six contract beamlines exist at SPring-8, either under construction or in operation:

BL15IN	Materials Science (Nat. Inst. for Res. in Inorg. Mat.)
BL16XU	Materials Science (Industrial Consortium)
BL16B2	Material Science (Industrial Consortium)
BL24XU	Multi-purpose (Hyogo Prefecture)
BL33LEP	Laser Electron Photon Studies (Osaka University)
BL44XU	Macromolecular Assemblies (Osaka University)

All of the beamlines are shown in the Beamline Map, including those that are still in the design stage.

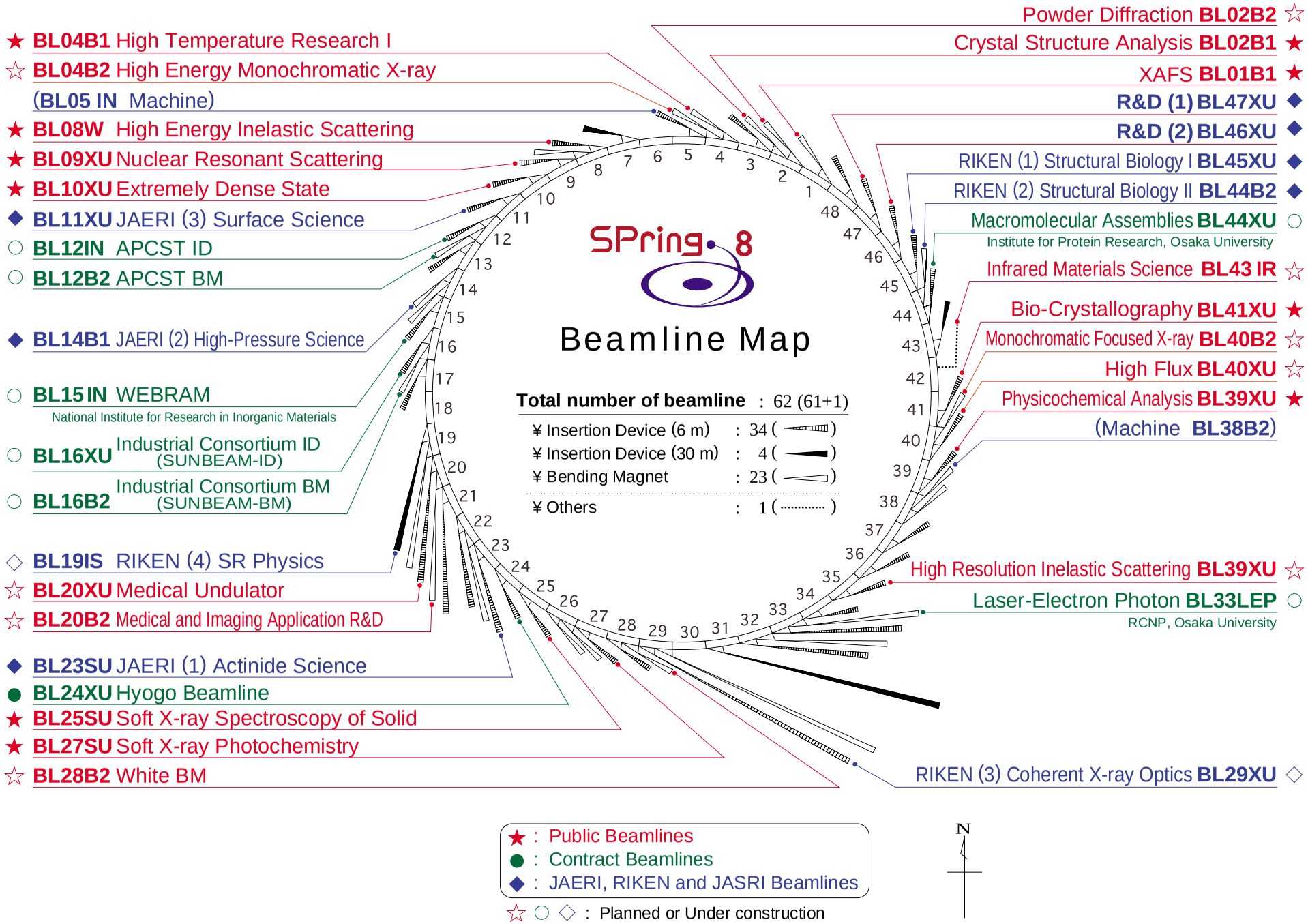
SPring-8
Beamline Map
Total number of beamline : 62 (61+1)
¥ Insertion Device (6 m) : 34
¥ Insertion Device (30 m) : 4
¥ Bending Magnet : 23
¥ Others : 1
★ BL04B1 High Temperature Research I
☆ BL04B2 High Energy Monochromatic X-ray
(BL05 IN Machine)
★ BL08W High Energy Inelastic Scattering
★ BL09XU Nuclear Resonant Scattering
★ BL10XU Extremely Dense State
◆ BL11XU JAERI (3) Surface Science
○ BL12IN APCST ID
○ BL12B2 APCST BM
◆ BL14B1 JAERI (2) High-Pressure Science
○ BL15IN WEBRAM
National Institute for Research in Inorganic Materials
○ BL16XU Industrial Consortium ID (SUNBEAM-ID)
○ BL16B2 Industrial Consortium BM (SUNBEAM-BM)
◇ BL19IS RIKEN (4) SR Physics
☆ BL20XU Medical Undulator
☆ BL20B2 Medical and Imaging Application R&D
◆ BL23SU JAERI (1) Actinide Science
● BL24XU Hyogo Beamline
★ BL25SU Soft X-ray Spectroscopy of Solid
★ BL27SU Soft X-ray Photochemistry
☆ BL28B2 White BM
Powder Diffraction BL02B2 ☆
Crystal Structure Analysis BL02B1 ★
XAFS BL01B1 ★
R&D (1) BL47XU ◆
R&D (2) BL46XU ◆
RIKEN (1) Structural Biology I BL45XU ◆
RIKEN (2) Structural Biology II BL44B2 ◆
Macromolecular Assemblies BL44XU ○
Institute for Protein Research, Osaka University
Infrared Materials Science BL43 IR ☆
Bio-Crystallography BL41XU ★
Monochromatic Focused X-ray BL40B2 ☆
High Flux BL40XU ☆
Physicochemical Analysis BL39XU ★
(Machine BL38B2)
High Resolution Inelastic Scattering BL39XU ☆
Laser-Electron Photon BL33LEP ○
RCNP, Osaka University
RIKEN (3) Coherent X-ray Optics BL29XU ◇
★ : Public Beamlines
● : Contract Beamlines
◆ : JAERI, RIKEN and JASRI Beamlines
☆ ○ ◇ : Planned or Under construction
N

Editor
Seishi Kikuta
SPring-8/JASRI

Editing & Layout
Marcia M. Obuti-Daté
SPring-8/JASRI

Photography
Maiko Isshiki & Katsuyuki Nakai
SPring-8/JASRI

Printing
Kōyū Printing Co., Ltd.

J A S R I
Kouto 1-1-1, Mikazuki, Sayo
Hyogo 679-5198, JAPAN
Tel. +81-(0) 791 58-2750 FAX: +81-(0) 791 58-2752
frontiers@spring8.or.jp

SPring-8

Japan Synchrotron Radiation Research Institute

Kouto 1-1-1, Mikazuki, Sayo
Hyogo 679-5198
JAPAN